

**MECHANICAL FLOW RESPONSE AND ANISOTROPY IN ULTRA-FINE
GRAINED MAGNESIUM AND ZINC ALLOYS**

A Dissertation

by

MAJID AL MAHARBI

Submitted to the Office of Graduate Studies of
Texas A&M University
in partial fulfillment of the requirements for the degree of
DOCTOR OF PHILOSOPHY

December 2009

Major Subject: Materials Science and Engineering

**MECHANICAL FLOW RESPONSE AND ANISOTROPY IN ULTRA-FINE
GRAINED MAGNESIUM AND ZINC ALLOYS**

A Dissertation

by

MAJID AL MAHARBI

Submitted to the Office of Graduate Studies of
Texas A&M University
in partial fulfillment of the requirements for the degree of

DOCTOR OF PHILOSOPHY

Approved by:

Chair of Committee,	Ibrahim Karaman
Committee Members,	Zachary Grasley
	K. Ted Hartwig
	Xinghang Zhang
Head of Department,	Tahir Cagin

December 2009

Major Subject: Materials Science and Engineering

ABSTRACT

Mechanical Flow Response and Anisotropy in Ultra-fine Grained Magnesium and Zinc Alloys. (December 2009)

Majid Al Maharbi, B.E., Sultan Qaboos University, Al-Khod, Oman;

M.S., Arizona State University

Chair of Advisory Committee: Dr. Ibrahim Karaman

Hexagonal closed packed (hcp) materials, in contrast to cubic materials, possess several processing challenges due to their anisotropic structural response, the wide variety of deformation textures they exhibit, and limited ductility at room temperature. The aim of this work is to investigate, both experimentally and theoretically, the effect of severe plastic deformation, ultrafine grain sizes, crystallographic textures and number of phases on the flow stress anisotropy and tension compression asymmetry, and the mechanisms responsible for these phenomena in two hcp materials: AZ31B Mg alloy consisting of one phase and Zn-8wt.% Al that has an hcp matrix with a secondary face-centered cubic (fcc) phase. Mg and its alloys have high specific strength that can potentially meet the high demand for light weight structural materials and low fuel-consumption in transportation. Zn-Al alloys, on the other hand, can be potential substitutes for several ferrous and non-ferrous materials because of their good mechanical and tribological properties. Both alloys have been successfully processed using equal channel angular extrusion (ECAE) following different processing routes in

order to produce samples with a wide variety of microstructures and crystallographic textures for revealing the relationship between microstructural parameters, crystallographic texture and resulting flow stress anisotropy at room temperature. For AZ31B Mg alloy, the texture evolution during ECAE following conventional and hybrid ECAE routes was successfully predicted using visco-plastic self-consistent (VPSC) crystal plasticity model. The flow stress anisotropy and tension-compression (T/C) asymmetry of the as received and processed samples at room temperature were measured and predicted using the same VPSC model coupled with a dislocation-based hardening scheme. The governing mechanisms behind these phenomena are revealed as functions of grains size and crystallographic texture. It was found that the variation in flow stress anisotropy and T/C asymmetry among samples can be explained based on the texture that is generated after each processing path. Therefore, it is possible to control the flow anisotropy and T/C asymmetry in this alloy and similar Mg alloys by controlling the processing route and number of passes, and the selection of processing conditions can be optimized using VPSC simulations. In Zn-8wt.% Al alloy, the hard phase size, morphology, and distribution were found to control the anisotropy in the flow strength and elongation to failure of the ECAE processed samples.

Dedicated

To my parents for their endless love

To my wife, Raya for here support and encouragement

To my sons, Ahmed and Shihab for the happiness and joy they bring to my life

ACKNOWLEDGMENTS

First of all, I would like to thank my advisor Dr. Ibrahim Karaman for his full support and encouragement throughout my PhD study here. Driven by his enthusiasm and motivated by his and his students' achievements in the field, my experience in scientific research excelled during the period of my PhD. I also, would like to thank Mr. Robert Barber for his highly appreciated help in processing the materials. The great discussions with my colleague, David Foley, as well as his help in processing and characterizing some of the materials are highly appreciated. I am also grateful to Sonia Razavi for her help in characterizing some of the materials studied in this dissertation.

I would like to thank my advisory committee, Dr. Hartwig, Dr. Zhang and Dr. Grasley for their support and valuable comments. I also thank Dr. Karaman's previous students, Mohammed Haouaoui and Guven Yapici, who taught me and introduced me to equal channel angular extrusion. I thank Ersin Karaca, Benat Kockar and Burak Basran for their help in using some of the machines and instruments in the labs. I am also thankful to Dr Karaman's group members, Ji Ma, Can Atli, Nevin Ozdemir, Cengiz Yegin, Fevzi Ozaydin, Fatmata Barrie, Ruixian Zhu, James Monroe, Ebubekir Dogan, Erhan Akin, Micheal Murphy, Peter Nystrom and William Zumalt, for creating a peaceful and motivational environment.

Last but not least, this work would not have been completed without the unconditional support of my wife. I really appreciate her sacrifices and patience, being away, taking care of our two sons and raising them while I am finishing this work.

TABLE OF CONTENTS

	Page
ABSTRACT.....	iii
DEDICATION.....	v
ACKNOWLEDGMENTS.....	vi
TABLE OF CONTENTS	vii
LIST OF FIGURES.....	x
LIST OF TABLES	xx
 CHAPTER	
I INTRODUCTION.....	1
1.1 Motivations.....	2
1.1.1 Magnesium alloys	3
1.1.2 Zinc-aluminum alloys	4
1.2 Objectives.....	5
1.3 Methods of Approach.....	7
1.3.1 Magnesium alloy	7
1.3.2 Zinc-aluminum alloy	9
II BACKGROUND AND LITERATURE REVIEW.....	12
2.1 Equal Channel Angular Extrusion.....	12
2.2 Hexagonal Closed-packed Materials and Magnesium Alloys	15
2.2.1 Deformation mechanisms in Mg.....	16
2.2.2 Equal channel angular extrusion of magnesium alloys and dynamic recrystallization	19
2.2.3 Flow stress anisotropy and tension-compression asymmetry of ECAE processed Mg alloys.....	26
2.3 Zinc-aluminum Alloys as Two-phase HCP Materials	28
2.3.1 Severe plastic deformation of Zn-Al alloys using equal channel angular extrusion	29
2.4 Visco-plastic Self-consistent Crystal Plasticity Modeling.....	32
2.4.1 VPSC modeling of ECAE process	34

CHAPTER	Page
2.4.2 Dislocation-based hardening model	36
III EXPERIMENTAL PROCEDURES	40
3.1 Materials.....	40
3.2 Thermomechanical Processing of AZ31B Mg Alloy Using Equal Channel Angular Extrusion.....	41
3.2.1 Microstructural characterization of as received and processed AZ31B alloy	44
3.2.2 Mechanical testing of as received and processed AZ31B alloy.....	44
3.3 Thermomechanical Processing of Zn-8wt.% Al Alloy Using Equal Channel Angular Extrusion.....	46
3.3.1 Microstructural characterization of as received and processed Zn-8wt.% Al alloy.....	47
3.3.2 Mechanical testing of as received and ECAE processed Zn-8wt.% Al alloy.....	48
IV FLOW STRESS ANISOTROPY AND TENSION COMPRESSION ASYMMETRY OF ECAE PROCESSED AZ31B MG ALLOY	49
4.1 Microstructure Evolution	49
4.2 Crystallographic Texture.....	52
4.3 Mechanical Flow Response.....	56
4.4 Discussion of Results	65
4.4.1 Texture prediction	65
4.4.2 Deformation mechanisms during ECAE.....	69
4.4.3 Effect of prismatic slip on dynamic recrystallization during ECAE.....	73
4.4.4 Effect of prismatic slip on evolution of grain morphology	74
4.5 Flow Stress Anisotropy and Tension-compression Asymmetry	75
4.6 Summary of Observations.....	81
V EFFECTS OF CRYSTALLOGRAPHIC TEXTURE OF AZ31B Mg ALLOY ON FLOW STRESS ANISOTROPY AND TENSION-COMPRESSION ASYMMETRY	83
5.1 Microstructures.....	84
5.2 Crystallographic Texture Evolution and Prediction.....	86
5.3 Mechanical Response.....	87
5.4 Low Temperature Processing of AZ31B Mg Alloy.....	91
5.5 Discussion of Results	96
5.5.1 Tensile twinning and tension-compression asymmetry	96

CHAPTER	Page
5.5.2 Different microstructures and similar textures	98
5.5.3 Slip and twinning dependence on grain size	99
5.5 Summary of Observations	101
VI PREDICTION OF FLOW STRESS ANISOTROPY AND TENSION-COMPRESSION ASYMMETRY OF AZ31B MG ALLOY	103
6.1 Dislocation-based Hardening Formulation	103
6.2 Prediction of Hot-rolled Sample Mechanical Response	106
6.3 Prediction of Mechanical Response of ECAE Processed AZ31B Mg Alloy	109
6.4 Discussion of Results	110
6.4.1 Governing mechanisms during through-thickness and in-plane monotonic testing of hot rolled plate.....	112
6.4.2 Deformation mechanisms of ECAE processed samples	113
6.5 Summary of Observations	115
VII FLOW RESPONSE OF A SEVERE PLASTICALLY DEFORMED TWO-PHASE ZINC-ALUMINUM ALLOY	117
7.1 Microstructural Evolution during ECAE	117
7.2 Tensile Flow Response.....	121
7.3 Wavelength Dispersive Spectroscopy (WDS)	125
7.4 Microhardness Evolution	127
7.5 Discussion of the Results	128
7.5.1 Effects of Al content on mechanical behavior of Zn-Al alloys after ECAE	128
7.5.2 Effects of ECAE processing routes on the microstructural evolution.....	131
7.5.3 Ductility Improvements after ECAE.....	132
7.5.4 Flow anisotropy in ECAE processed materials.....	133
7.6 Summary of Observations.....	135
VIII MAIN CONCLUSIONS	137
IX SUGGESTIONS FOR FUTURE WORKS.....	141
REFERENCES	147
VITA	153

LIST OF FIGURES

	Page
Figure 2.1 (a) Schematic illustration of typical ECAE process: The X, Y and Z plane denote the extrusion plane, flow plane and longitudinal plane respectively [31]. (b) Schematic demonstrating the simple shear that the representative material element goes through during the process. ED, LD and FD are the extrusion, longitudinal and flow directions which are the directions perpendicular to the extrusion, longitudinal and flow planes, respectively. ϕ is the die angle and ψ is the curvature angle ranging from 0° for sharp die and 90° .	13
Figure 2.2 The four conventional processing routes in ECAE [32].	14
Figure 2.3 Schematic of slip and twinning systems observed in Mg alloys.	19
Figure 2.4 X-ray diffraction spectra of (a) directly extruded AZ31 Mg alloy and (b) the ECAE processed and annealed AZ31 alloy. (c) Nominal stress-strain response of AZ31 alloy after direct extrusion and after annealing following ECAE [55].	21
Figure 2.5 Pole figures (equal area projection) show the crystallographic textures in: (a) conventionally extruded, (b) ECA processed and (c) annealed AZ31B as determined by neutron diffraction [14]. The extrusion axes are to the right.	22

Figure 2.6	A summary of ECAE studies on improving the mechanical properties of Mg alloys. Solid and hollow symbols represent yield and ultimate stresses, respectively.	23
Figure 2.7	The TEM micrographs of (a) as-received AZ31 Mg alloy; the same alloy (b) after ECAE at 498 K for five passes; and (c) after two-step ECAE: 498 K for four passes following route B _C and one pass at 453 K [71].	26
Figure 2.8	Tensile tests results from the AZ31B ECAE processed samples having a variety of orientations with respect to the ECAE processed bar shown in the upper left corner. Basal pole figure of the sample which is ECAE processed up to eight passes following route B _C and then annealed is shown on the upper right corner [14].	27
Figure 2.9	Phase diagram of Zn-Al alloys showing the Zn-wt.% Al alloy.	29
Figure 2.10	Microstructure of Zn-22wt.%Al (a) in as received condition where the bright and dark grains are Al-rich and Zn-rich, respectively, (b) after 8 ECAE passes and (c) after high pressure torsion [17].	30
Figure 2.11	Evolution of strength levels with the number of ECAE passes, of (a) ZA5 [21], (b) ZA12 [19], (c) ZA27 [16] and (d) ZA40 [15].	32
Figure 2.12	Schematic of the Composite Grain (CG) model implemented in VPSC to model twinning, showing morphology and orientation of twins and matrix, and indicating the parameters of the CG model.	34

Figure 2.13	Reference coordinate systems used in the ECAE process showing the deformation of a square by simple shear at the intersection plane of the channels.....	35
Figure 3.1	Schematics of the two extrusion cases, (a) 1A-I: the starting basal poles are parallel to the ED and (b) 1A-II: the basal poles are parallel to the FD.....	43
Figure 3.2	Schematic showing the tension and compression samples cut along the three orthogonal directions in the ECAE processed AZ31B Mg alloy: extrusion direction (ED), longitudinal direction (LD) and flow direction (FD).....	45
Figure 4.1	(a) The microstructure, (b) grain size distribution, and (c) texture of the starting AZ31B Mg alloy.	50
Figure 4.2	Optical micrographs of AZ31B ECAE samples processed starting with basal poles (a) parallel to the extrusion direction (1A-I) and (b) parallel to the flow direction (1A-II). The extrusion direction is to the right.	51
Figure 4.3	Optical micrographs of AZ31B ECAE samples processed starting with basal poles parallel to the extrusion direction and up to two ECAE passes following route (a) A (2A-I), (b) C (2C-I) and (c) BC (2BC-I).	53

- Figure 4.4 Prismatic and basal pole figures of starting and ECAE processed AZ31B Mg alloy after one ECAE pass with two different initial textures. (a) In the 1A-I case, most grains have c-axes parallel to LD. There is also a secondary peak in the basal pole figure making an angle of about 35° about LD. (b) In the 1A-II case, the basal poles are more spread around FD towards a pole that makes a 27° angle with LD.55
- Figure 4.5 Basal and prismatic pole figures for (a) 2A-I (b) 2C-I and (c) 2B_C-I samples. The starting texture of all these cases is similar to the one shown in Figure 6.a. The split between the peaks in the basal pole figures of 2A-I and 2C-I samples is measured as 29° and 65° , respectively.....55
- Figure 4.6 Room temperature tensile (solid lines) and compressive (dashed lines) responses of as-received, hot rolled AZ31B alloy along the two plate directions: In-plane (IP) and through-thickness (TT).....57
- Figure 4.7 Room temperature tension (solid lines) and compression (dashed lines) of AZ31B alloy ECAE processed starting with basal poles parallel to (a) Extrusion direction (1A-I) and (b) Flow direction (1A-II).....61

Figure 4.8	Room temperature true tension (solid lines) and compression (dashed lines) of AZ31B ECAE samples processed up to two passes following route (a) A (2A-I), (b) C (2C-I), and (c) BC (2BC-I).....	64
Figure 4.9	Predicted basal pole figures of AZ31B Mg alloy processed via one ECAE pass starting with basal poles parallel to (a) the extrusion direction (1A-I), and (b) parallel to the flow direction (1A-II).....	67
Figure 4.10	Predicted basal pole figures of AZ31B Mg alloy processed via two ECAE passes starting with basal poles parallel to the extrusion direction and following route (a) A (2A-I), (b) C (2C-I) and (c) B _C (2B _C -I).....	68
Figure 4.11	Predicted relative activities of the considered deformation modes for one ECAE pass starting with basal poles parallel to (a) the extrusion direction (1A-I), and (b) parallel to the flow direction (1A-II).....	70
Figure 4.12	Predicted relative activities of slip systems during the second ECAE pass starting with basal poles parallel to the extrusion direction, and following route (a) A (2A-I), (b) C (2C-I) and (c) B _C (2B _C -I).....	71
Figure 4.13	The predicted distribution of grain ellipsoidal ratio (grain major to minor axes ratio (a/b)) for the two one-pass ECAE cases: (a) starting with basal poles parallel to extrusion direction (1A-I) and (b) starting with basal poles parallel to flow direction (1A-II).....	76

Figure 4.14	Predicted distribution of ellipsoidal grain major to minor axes ratio (a/b) for the three two-pass ECAE cases starting with basal poles parallel to extrusion direction and following route (a) A (2A-I), (b) C (2C-I) and (c) B _C (2B _C -I).. (d) The polynomial fits, and, the experimental and predicted average of (a/b) ratio of the three two-pass ECAE cases.	77
Figure 4.15	Lower magnification optical micrographs of AZ31B ECAE samples processed starting with basal poles parallel to the extrusion direction and up to two ECAE passes following route (a) A (2A-I), (b) C (2C-I) and (c) B _C (2B _C -I) . The extrusion direction is to the right.	78
Figure 4.16	Evolution of stress differential (SD) ratio with number of ECAE passes of the as received (AR) sample and the samples of two-passes ECAE following the three routes: A, C and B _C , along the three orthogonal directions of the billets: extrusion direction (ED), longitudinal direction (LD) and flow direction (FD).	79
Figure 5.1	Optical micrographs of AZ31B ECAE samples processed up to four ECAE passes and following routes (a) A (4A-I), (b) C (4C-I), (c) E (4E-I) and (d) B _C (4B _C -I).....	85
Figure 5.2	Grain size distribution of AZ31B ECAE samples processed up to four ECAE passes and following routes (a) A (4A-I), (b) C (4C-I), (c) E (4E-I) and (d) B _C (4B _C -I).....	86

Figure 5.3	Predicted and measured basal pole figures of AZ31B Mg alloy processed via four ECAE passes starting with basal poles parallel to extrusion directions and following route (a) A (4A-I), (b) C (4C-I), (c) E (4E-I) and (d) B _C (4B _C -I).....	88
Figure 5.4	Tensile (solid lines) and compressive (dashed lines) true response of AZ31B alloy ECAE processed up to four passes following route (a) A (4A-I), (b) C (4C-I), (c) E (4E-I) and (d) B _C (4B _C -I)	90
Figure 5.5	Optical micrographs of AZ31B sample ECAE processed following the hybrid route (a) 5H-I sample and (b) 7H-I sample.....	94
Figure 5.6	Prismatic and basal pole figures of AZ31B sample processed following (a) 5H-I and (b) 7H-I hybrid routes. The numbers in these labeling indicates the number of ECAE passes I represents the type of initial starting texture in which basal pole.	95
Figure 5.7	Predicted basal pole figures of AZ31B sample processed following (a) 5H-I and (b) 7H-I hybrid routes. The numbers in these labeling indicates the number of ECAE passes and I represents the type of initial starting texture in which basal pole.	95
Figure 5.8	The mechanical response of the AZ31B Mg samples processed via the hybrid route (a) 5H and (b) 7H.....	96

Figure 5.9	The stress differential ratio of as-received along the two plate directions, and as ECAE processed up to four passes following routes A, B _C , C and E.....	97
Figure 5.10	The mechanical response along flow direction (FD) of (a) Texture A samples and (b) Texture C samples.....	101
Figure 6.1	Experimental (lines) and predicted (symbols) of the as-received hot rolled sample.	108
Figure 6.2	The predicted activities of deformation modes during (a) Through-Thickness Compression (TTC), (b) Through-Thickness Tension (TTT) in parent grains and (c) in twins, (d) In-Plane tension (IPT) and, (e) In-Plane compression in parent grains and (f) in twins, of the as-received hot rolled AZ31B Mg sample.	109
Figure 6.3	Experimental (lines) and predicted (symbols) of AZ31B samples ECAE processed up to four passes following route (a) A (4A-I), (b) C (4C-I), (c) E (4E-I) and (d) B _C (4B _C -I).....	111
Figure 6.4	The predicted relative activities of deformation modes during tension along the FD of the AZ31B ECAE processed up to four passes following route (a) A (4A-I), (b) C (4C-I), (c) E (4E-I) and (d) B _C (4B _C -I).....	114

	Page
Figure 7.1 Optical micrographs of (a) the as-cast ZA-8 alloy and ECAE processed alloy for (b) one pass, (c) two passes, and (d) eight passes in route B _C	119
Figure 7.2 Optical micrographs of ECAE processed ZA-8 alloy up to eight passes via (a) route C, (b) route B _A , (c) route B _C and (d) route E.....	120
Figure 7.3 Room temperature true tensile stress vs. strain curves of the as-cast ZA-8 alloy and the samples ECAE processed using route B _C up to 8 passes.....	122
Figure 7.4 Room temperature true stress vs. true strain curves of the ECAE processed ZA-8 alloy up to eight passes using different processing routes.....	122
Figure 7.5 Macroscopic appearance of the failed tensile samples in the as-cast and ECAE processed conditions.....	124
Figure 7.6 Room temperature true stress vs. true strain curves of the ECAE processed ZA-8 alloy tested along the extrusion direction and the directions parallel and perpendicular to the long axis of the elongated hard phase particles or bands (see Figure 1) for samples processed for (a) 1A, (b) 2B _C , and (c) 8B _C . (HP: The long axis direction of the hard-phase particles).....	126

Figure 7.7	Evolution of ultimate tensile strength with the number of extrusion passes in different ECAE studies on Zn-Al alloys including the present work.	129
Figure 7.8	Back-scattered electron images of (a) as cast, (b) 1A, (c) 2B _C and (d) 8B _C samples. The hard phase particles are sheared and elongated starting from the first pass. However, the elongated structure is fully developed after the second pass. Large elongated particles can still be seen in 2B _C sample. In 8B _C sample, these particles are broken into much smaller particles that form elongated bands.	134

LIST OF TABLES

		Page
Table 3.1	A list of ECAE experiments carried out on AZ31B and ZK60A Mg alloys.	43
Table 3.2	Details of the processing and characterization experiments conducted on AZ31B Mg alloys.	45
Table 3.3	A list of ECAE and characterization experiments conducted on Zn-8wt.% Al alloy.	47
Table 4.1	Mechanical properties of ECAE processed AZ31B Mg alloy under tension and compression including the standard deviation. The number before the billet label indicates the number of passes, I represent the starting texture of basal poles parallel to the extrusion direction and II represent the starting texture of basal poles parallel to the flow direction. (IP: In-plane, TT: Through-Thickness, ED: Extrusion Direction, LD: Longitudinal Direction, FD: Flow Direction, SD: Stress Differential).	58
Table 5.1	Mechanical properties of ECAE processed AZ31B Mg alloy under tension and compression. The number before the billet label indicates the number of passes, and the letter represents the ECAE route.	92

	Page
Table 6.1 Deformation modes considered in the prediction of the stress-strain response.....	106
Table 6.2 Hardening parameters for slip systems considered in the predictions.	107
Table 7.1 Tensile properties of the as-cast and ECAE processed ZA-8 alloy. HP: Major axis direction of the hard phase.....	123
Table 7.2 Chemical compositions of the two phases in the as-cast and ECAE-processed ZA-8 alloy as a function of the processing parameters.	127
Table 7.3 Vickers microhardness values of the two phases of the as-cast and ECAE processed ZA-8 alloy as a function of the processing parameters.	128

CHAPTER I

INTRODUCTION

Hexagonal closed packed (hcp) materials, in contrast to cubic structured ones, are scientifically interesting due to their anisotropic behaviors and to the wider variety of deformation textures they exhibit. They usually have more deformation modes than body-centered cubic (bcc) or face-centered cubic (fcc) materials but lower number of independent systems. Therefore, they usually have limited ductility compared to cubic materials because of the lack of sufficient independent slip systems to accommodate plastic deformation. The high number of possible deformation mechanisms in these materials ranging from slip to twinning systems, also, makes it very challenging to model and predict their behaviors. There has been lot of attention, recently, in studying these materials like Titanium (Ti), Zirconium (Zr), Beryllium (Be) and Magnesium (Mg) alloys as structured materials for aerospace, biomedical, nuclear and other engineering applications.

Although these materials have the same crystal structure (hcp structure), their deformation mechanisms are not always the same. The c/a ratio, which is the ratio of the hcp lattice parameters, c and a , dictates these governing mechanisms, and, hence their behaviors during plastic deformation and their evolved textures. It is believed that the distinct texture evolutions of these materials are due to the combined effect of c/a ratio

This dissertation follows the style of Acta Materialia.

and the fact that different hcp metals deform by different slip and/or twinning modes [1] which in turn are somehow affected by c/a ratio. This is why, historically, hcp materials have been categorized in terms of c/a ratio. As an example of the influence of c/a ratio, in metals with $c/a < \sqrt{3}$, the common $\{10\bar{1}2\}$ twin is activated by c-axis tension. Therefore, during compression (or cold or hot rolling) grains are favorably oriented for this twin if their axis is perpendicular to the compression axis; and twinning reorients the c-axis of the twin nearly parallel to the compression axis (or normal of the rolled plate) [2]. This is the major reason behind the basal or near basal textures of rolled hcp metals [3]. On the other hand, in metals with $c/a > \sqrt{3}$, excluding Zn, this primary twin is activated by compression along c-axis. Mg has a c/a ratio of about 1.624 which is very close to the theoretical value of $\sqrt{8/3}$ calculated by assuming spherical atoms having radius R equals to a/2.

1.1 Motivations

In our group, Ti and Zr alloys have been processed to improve their mechanical properties, and, their flow stress anisotropy and texture evolution during plastic deformation have been studied [4-8]. The flow stress anisotropy and tension compression asymmetry of other materials such as ultrafine grained (UFG) copper [9, 10] have also been studied by our group. The texture evolution and flow stress anisotropy of these hcp structured alloys have, also, been successfully predicted using a visco-plastic self-consistent (VPSC) crystal plasticity model. Motivated by the success in processing these hard to deform hcp alloys using equal channel angular extrusion

(ECAE), and, in predicting their texture evolution and flow stress anisotropy, the present dissertation focuses on an Mg alloy as a single-phase hcp alloy and a Zinc-Aluminum alloy as a two-phase alloy having an hcp matrix.

1.1.1 Magnesium alloys

Mg and its alloys have high specific strength and hence are gaining interest in many industrial and research communities for structural materials that can potentially meet the high demand for low fuel-consumption. However, frequent observations of low ductility and relatively low strength present great concern and limitation. Mg alloys, like any materials with an hcp crystal structure, has a limited number of easy-to-activate independent slip systems. Moreover, because of the anisotropic nature of the slip and twinning modes used by Mg to accommodate plastic deformation, they tend to develop texture under deformation. Texture and the relatively large differences in the activation stresses between the different slip modes lead to highly anisotropic mechanical properties. This means that the material can be relatively strong (but brittle) when tested in one direction, but low in strength (and relatively ductile) when tested in another. However, in some instances, highly anisotropic deformation can give these alloys an advantage over other more isotropic structural materials, such as in blast protection applications. Therefore, an understanding of the relationship between deformation texture, micro-scale slip and twinning activity, and macro-scale anisotropic flow behavior is vital for controlled synthesis (processing routes and parameters) of material for specific application needs.

Concerning the flow stress anisotropy and tension-compression asymmetry of Mg alloys, there is a lack of investigation of these behaviors in literature. There are few studies that tackled the flow stress anisotropy in tension or compression but not tension-compression asymmetry, and they are done on alloys that have conventionally extruded [11, 12], plate [13] and one ECAE texture [14]. It is well known that the crystallographic texture and grain morphology of materials evolve with strain path changes and magnitude. Both, texture and grain morphology can influence the mechanical response of the materials. Therefore, a detailed investigation that involves processing the material following different ECAE routes and up to different number of ECAE passes along with modeling is required to fully understand the deformation mechanisms of these alloys and the influence of texture, and grain size and morphology on these mechanisms. The reasons behind selecting ECAE to process these alloys in this work are presented later in this chapter.

1.1.2 Zinc-aluminum alloys

In addition to studying the ultra-fine grained (UFG) AZ31B Mg, a zinc-aluminum two phase alloy, in which aluminum-rich secondary hard phase embedded in a zinc-rich hcp matrix, will also be ECAE processed in order to refine the microstructure and introduce UFG microstructures in the alloy. The effect of the size and morphology of the second hard phase, on the mechanical behaviors and flow stress anisotropy of this alloy is investigated.

Several Zn-Al alloys were investigated and processed using ECAE including: ZA-40 [15], ZA-27 [16], ZA-22 [17, 18], ZA-12 [19], ZA-8 [20] and ZA-5 [21] (digits

in the alloy designations indicate their approximate Al content in weight. ZA represents Zinc-Aluminum). Most of these studies have reported an increase in strength of the as-cast alloys after the first ECAE pass due to the reported microstructural refinement and the elimination of as-cast dendritic structure, but they also reported some notable decrease after further ECAE passes, even in some cases, to lower values than the as-cast strength levels. To the best of our knowledge, there is no clear understanding of why strength levels drop with further ECAE in the presence of the microstructural refinement. In addition, the effects of the composition and morphology of the hard second phase on the flow response of ECAE processed materials were not investigated. Therefore, one of the goals of the present dissertation is to improve the room temperature tensile properties of the ZA-8 (Zn-8%Al) alloy using lower temperature ECAE processing than those previously reported, and to reveal the mechanisms for such possible changes, if any, in these properties. In order to mechanically rationalize these improvements in tensile properties after ECAE and to reveal the effect of different processing routes on these properties, a detailed investigation was carried out focusing on the composition, strength levels and morphology of the two constitutive phases.

1.2 Objectives

Upon the above discussion, the objectives of this study can be summarized as follows:

1. Process AZ31B Mg alloys using equal channel angular extrusion following different processing routes, temperatures and up to different number of ECAE passes.

2. Identify the influence of the starting textures on microstructural and texture evolution during ECAE.
3. Investigate the mechanical behavior of ECAE processed AZ31B alloy by determining flow stress anisotropy and tension-compression asymmetry as functions of processing routes and number of passes.
4. Identify the influence of texture and grain size and morphology on flow stress anisotropy and tension-compression asymmetry.
5. Predict the texture evolution during ECAE process of the AZ31B alloy using a visco-plastic self consistent (VPSC) crystal plasticity model in order to fully understand the governing mechanisms leading to the wide variety of deformation textures on this alloy.
6. Predict flow stress anisotropy of the unprocessed and ECAE processed alloy using the same VPSC model coupled with dislocation-based hardening formulation.
7. Improve the mechanical properties of the two-phase Zn-8wt.%Al alloy by refining the microstructure and homogeneously distribute the hard second phase in the hcp matrix using ECAE.
8. Explain the reported softening of ECAE processed zinc-aluminum alloys and understand the softening mechanisms.
9. Identify the effects of the presence of second hard phase on the anisotropy of the Zn-Al alloys on their flow stress anisotropy.

1.3 Methods of Approach

In order to reach these objectives, a combination of experimental and modeling investigations have been carried out for the two alloys studied in this dissertation. They are listed here for each alloy separately although ECAE processing was used to process and understand the behaviors of both alloys.

1.3.1 Magnesium alloy

In order to pursue the goal of understanding the behavior of Mg alloys and hence, hcp metals and alloys in general, a systematic study is carried out on an AZ31B Mg alloy to link texture evolution, microstructural evolution, and dynamic recrystallization (DRX) to slip activity during severe plastic deformation (SPD). To achieve this fundamental understanding the AZ31B Mg alloy was processed using equal channel angular extrusion (ECAE) [22]. ECAE has been utilized to severely deform metals and alloys in order to refine the grains and hence improve strength and ductility. This grain refinement depends on several ECAE parameters like the extrusion temperature and speed, the number of passes and the processing path or routes. The possibility of multi-pass processing following different processing routes that ECAE offers makes it the best processing technique to achieve the goals of this dissertation. The billet can be rotated about its extrusion axis between consecutive passes and hence subjected to different shearing patterns. Therefore, these ECAE routes and number of passes usually lead to different microstructural [23] and texture evolution [24] after ECAE. This wide variety of deformation textures is what needed to satisfy the goals of this dissertation.

Therefore, the AZ31B alloy is ECAE processed at 200 °C starting with two different crystallographic textures for up to four ECAE passes following different processing routes A, C, E and B_C to vary the relative contributions of different slip modes (basal, prismatic, pyramidal <c+a>). This processing results in many processed samples in addition to the as received sample. An ECAE simulation model [25, 26] built on the visco-plastic self-consistent (VPSC) crystal plasticity scheme [27] is used to predict the relative activities of the aforementioned hcp slip modes, and the texture and grain morphology evolution associated with each ECAE test. It is demonstrated that texture, grain elongation, and the amount of DRX are highly dependent on the starting texture and differences can be correlated with the relative activity of each slip system during ECAE.

Regarding the flow stress anisotropy and tension-compression asymmetry of Mg alloys, a detailed investigation that involves the above mentioned processing along with modeling is required to fully understand the deformation mechanisms of these alloys and the influence of texture, and grain size and morphology on these mechanisms. The results of this study are presented in Chapter IV of this dissertation. It is found that the variation in flow stress anisotropy and tension-compression asymmetry among the samples can be explained based on the texture that is generated after each processing path. The influence of texture and grain size on the mechanical response and, hence, the anisotropy and asymmetry of these alloys is also compared and weighted. In order to do that, the alloy is also processed using several thermo-mechanical hybrid routes that utilize ECAE, in order to refine the grain size even more while preserving the texture.

The hybrid routes produce at least two distinct cases each one of them has samples that share similar texture but have different grain sizes and morphologies. Those cases are beneficial for weighing the influence of grain sizes and morphology on mechanical behaviors while eliminating texture effects. Chapter V focuses on the degree of influence of both texture and grain size and morphology on the flow stress anisotropy and tension and compression asymmetry of AZ31B Mg alloy.

In order to fully understand and explain the anisotropic behavior of Mg alloys, one of the goals of this dissertation is to predict the stress-strain response of ECAE processed AZ31B Mg alloy. This goal is achieved by using the aforementioned VPSC polycrystalline model coupled with a dislocation-based hardening law which is presented in Chapter II. The dislocation-based hardening parameters are first determined by fitting the stress-strain responses of unprocessed alloy along different directions. Those parameters are materials properties that describe the evolution of critical resolved shear stresses (CRSS) of each deformation mode, dislocation density and other microstructural characteristics of plastic deformation. The stress-strain response of the ECAE processed samples along different direction under tension and compression is then be predicted using the same parameters. These predictions are presented in Chapter VI of this dissertation.

1.3.2 Zinc-aluminum alloy

In this dissertation, the Zn-8wt.%Al two-phase zinc-aluminum alloy has been subjected to severe plastic deformation via equal channel angular extrusion (ECAE). The alloy is successfully extruded at homologous temperatures around $0.5 T_m$ through

various strain paths and magnitudes. Multi-pass ECAE processing following different routes led to the elimination of the as-cast dendritic microstructure and formed a structure of elongated, ribbon shaped phases. Monotonic tensile tests are conducted at room temperature along the longitudinal axis of the ECAE samples in addition to the directions parallel and perpendicular to the long axis of the elongated hard eutectoid phase particles in order to reveal the effect of microstructural morphology on the anisotropic flow response. The flow strength levels increase significantly after the first ECAE pass, and then saturated at a slightly higher value after the subsequent passes in route B_C.

In addition, possible mechanisms responsible for the reported softening upon further ECAE are revealed. Despite the relative chemical homogenization between the hard and soft phases, the size and distribution of the hard phase in the matrix are found to be the dominant factor controlling the flow response of the present two-phase zinc-aluminum alloy after ECAE. The hard phase size, morphology, and distribution are also found to control the anisotropy in the flow strength and elongation to failure of the ECAE processed samples. Notable flow softening with increasing number of ECAE passes, a general observation for the ECAE processed Zn-Al alloys with Al content more than 12%, is lacking in the present alloy which was attributed to the hardening effect of the fine eutectoid particles in the eutectic matrix overcoming the softening effect of deformation-induced chemical homogenization. The results concerning the Zn-Al alloys are presented in Chapter VII.

In addition to the above mentioned main chapters. Chapter II presents some background about current alloys, ECAE process and VPSC model. It also includes a literature review of previous studies related to the current study. More materials details and experimental procedures are presented in Chapter II. At the end of this dissertation, the main conclusions and suggestion for future works are included in Chapters VIII and IX, respectively.

CHAPTER II

BACKGROUND AND LITERATURE REVIEW

In this chapter, a brief background on the materials studied in this dissertation and the equal channel angular extrusion (ECAE) process used to process them. A literature review of related previous studies is conducted and presented in this chapter.

2.1 Equal Channel Angular Extrusion

Equal channel angular extrusion is a severe plastic deformation technique invented by Segal in 1981 [22] and have been used extensively to process materials since then. During ECAE, the materials are processed by simple shear at the intersecting plane of two channels that have the same cross-section and make an angle ϕ between them (see Figure 2.1.b). The billet is pushed into the upper channel and exited out of the bottom channel. Because the two channels have the same cross-section the billet will have the same dimensions and hence the process can be repeated to increase the total imposed strain. The effective Von Misses imposed strain during each pass depends on the die angle ϕ and it is given by the following equation for the sharp angle die [28]:

$$\varepsilon = \frac{2}{\sqrt{3}} \cot \phi \quad (2.1)$$

After N passes the equivalent imposed strain may be expressed in a general form by the following relationship [29, 30]:

$$\varepsilon_N = \frac{N}{\sqrt{3}} \left[2 \cot \left(\frac{\phi}{2} + \frac{\psi}{2} \right) + \psi \operatorname{cosec} \left(\frac{\phi}{2} + \frac{\psi}{2} \right) \right] \quad (2.2)$$

ψ is the angle outlined by the arc of curvature at the point of intersection (Figure 2.1.b). It follows that this general expression in equation (2.2) reduces to equation (2.1) multiplied by number of passes N if $\psi = 0$.

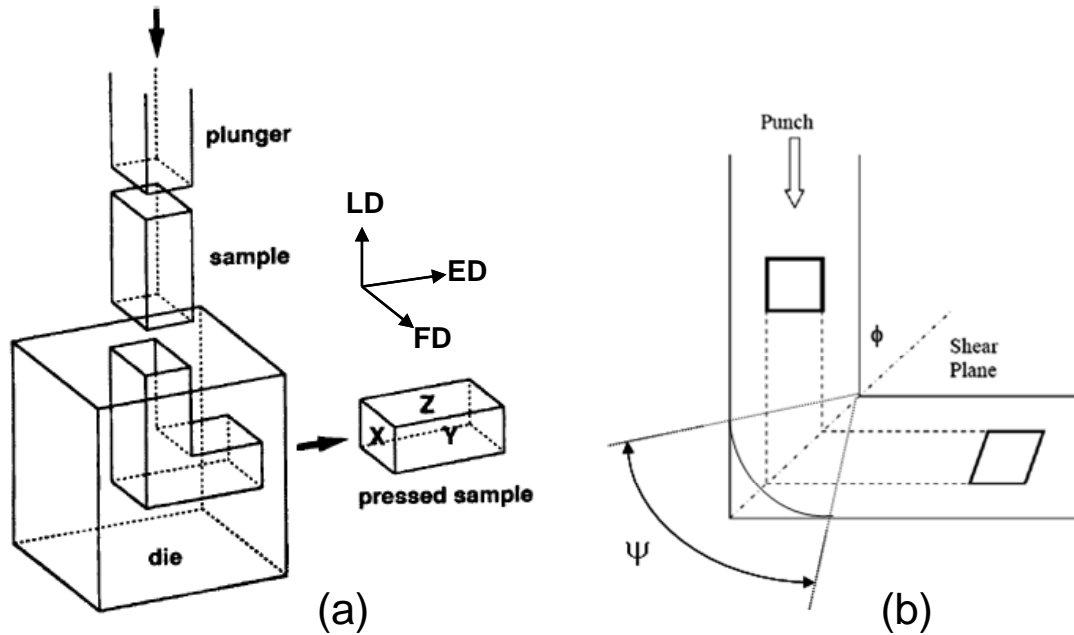


Figure 2.1 (a) Schematic illustration of typical ECAE process: The X, Y and Z plane denote the extrusion plane, flow plane and longitudinal plane respectively [31]. (b) Schematic demonstrating the simple shear that the representative material element goes through during the process. ED, LD and FD are the extrusion, longitudinal and flow directions which are the directions perpendicular to the extrusion, longitudinal and flow planes, respectively. ϕ is the die angle and ψ is the curvature angle ranging from 0° for sharp die and 90° .

In addition to the possibility of multi-pass processing, ECAE also offers the possibility of processing the material through different processing routes. The billet can

be rotated about its extrusion axis between consecutive passes and hence subjected to different shearing patterns. Therefore, these ECAE routes usually lead to different microstructure [23] and texture evolution [24] after ECAE. There are four known conventional ECAE routes: A, B_A, B_C and C. In route A, the billet is continually processed without rotation. In route B_A, the billet is rotated by +90° then -90° after each pass. In route B_C, the billet is always rotated by 90° before each successive pass. In route C, the billet is rotated by 180° between passes. These four conventional routes are illustrated in Figure 2.2. Combination of these routes can also be used. For example, the hybrid route E which is used in this study is a combination of route C and B_C, where the billet is rotated by 180 and 90° before the even and odd-numbered passes, respectively.

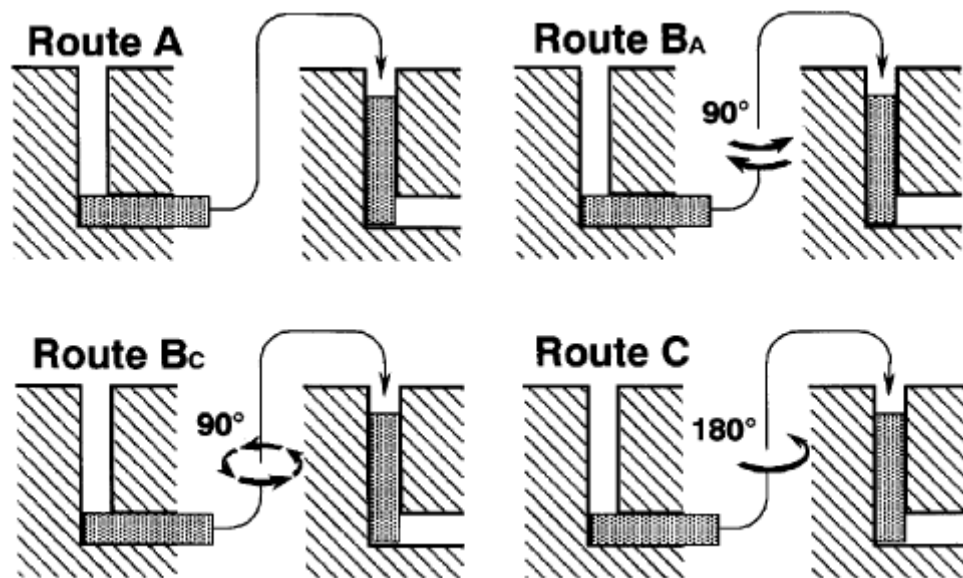


Figure 2.2 The four conventional processing routes in ECAE [32].

ECAE has been utilized to severely deform metals and alloys in order to refine the grains and hence improve strength and ductility. This grain refinement depends on several ECAE parameters like the extrusion temperature and speed, the number of passes and the die's angle. As mentioned above, the total imposed strain is dependent on the die angle ϕ through equations (2.1) and (2.2). It follows from those equations that smaller angle leads to higher amount of imposed strain. It was also shown by Horita et al. [33] that smaller die angle [90 – 115°] leads to high volume fraction of high angle grain boundaries compared to larger die angles.

2.2 Hexagonal Closed-packed Materials and Magnesium Alloys

Mg and its alloys have high specific strength and hence are gaining interest in many industrial and research communities for structural materials that can potentially meet the high demand for low fuel-consumption. However, frequent observations of low ductility and relatively low strength present great concern and limitation. Mg alloys have a hexagonal close-packed (hcp) crystal structure and hence a limited number of easy-to-activate independent slip systems. Moreover, because of the anisotropic nature of the slip and twinning modes used by Mg to accommodate plastic deformation, they tend to develop texture under deformation. Texture and the relatively large differences in the activation stresses between the different slip modes lead to highly anisotropic mechanical properties. This means that the material can be relatively strong (but brittle) when tested in one direction, but low in strength (and relatively ductile) when tested in another. However, in some instances, highly anisotropic deformation can give these alloys an advantage over other more isotropic structural materials, such as in blast

protection applications. Therefore, an understanding of the relationship between deformation texture, micro-scale slip and twinning activity, and macro-scale anisotropic flow behavior is vital for controlled synthesis (processing routes and parameters) of material for specific application needs.

2.2.1 Deformation mechanisms in Mg

At room temperature, the two dominant deformation modes in Mg alloys are basal slip and $\{10\bar{1}2\}$ tensile twinning [11, 34-36]. Because these two modes alone cannot accommodate an arbitrary deformation according to the von Mises [37] or Taylor [38] criteria, non-basal slip systems are needed. The non-basal slip systems sharing the same $\langle a \rangle$ Burgers vector, prismatic slip and pyramidal $\langle a \rangle$ slip have higher critical resolved shear stresses (CRSS) than basal slip. Pyramidal $\langle a \rangle$ slip is considered crystallographically equivalent to a combination of cross slip from basal to prismatic $\langle a \rangle$ and vice versa [1, 39]. Unlike these slip modes, the non-basal slip system, pyramidal $\langle c+a \rangle$ slip, plays an important role, providing shear deformation parallel to the c-axis [40-42] and a sufficient number of slip systems to fulfill the Taylor criterion. Pyramidal $\langle c+a \rangle$ slip is associated with the largest Burgers vector, the smallest interplanar spacing, the narrowest dislocation width and the lowest “ease of glide” [1, 43], and a “zonal” character of its core [44, 45]. Therefore the CRSS of this non-basal slip mode is also relatively high in comparison with basal slip. Because of their high CRSS values, prismatic slip and pyramidal $\langle c+a \rangle$ slip are reported to occur mostly in regions of high stress concentration, such as grain boundaries and twin interfaces [1, 46-

49]. As a result of the limited number of independent deformation modes, the high ratios of CRSS values between the active slip modes, and the directional nature of $\{10\bar{1}2\}$ twinning, which can be even easier to activate than basal slip in Mg [50]. Mg alloys are expected to develop strong deformation textures, and hence, high flow stress anisotropy and tension-compression asymmetry.

Because of the insufficient independent slip systems and the difficulty of activating some of them, twinning is observed in polycrystalline Mg. There are two main twinning systems in Mg alloys: tensile $\{10\bar{1}2\} \langle 10\bar{1}1 \rangle$ and compressive $\{10\bar{1}1\} \langle 10\bar{1}2 \rangle$ twins which accommodate c-axis extension and contraction, respectively [1, 51]. Due to the lack of sufficient number of independent slip systems, twinning is important as relaxation mechanism and can contribute to satisfy the Taylor condition of five independent deformation systems [52]. However, Brown et al. [53] proposed that tensile twinning contribute as a half independent deformation mode due to its unidirectional nature. The $\{10\bar{1}2\}$ tensile twinning in hcp materials is described as follows:

$$K_1 = \{10\bar{1}2\}, K_2 = \{\bar{1}012\}, \eta_1 = \langle \bar{1}011 \rangle, \eta_2 = \langle \bar{1}0\bar{1}1 \rangle \quad (2.3)$$

$$\gamma_0 = \frac{\sqrt{3}}{(c/a)} - \frac{(c/a)}{\sqrt{3}} \quad (2.4)$$

Where K_1 , K_2 , η_1 and η_2 are the twinning parameters, and, c and a are the hcp lattice constants. For the materials with $c/a < \sqrt{3}$, like Mg ($c/a = 1.624$), the direction of

shear is $[\bar{1}011]$, and the twinning occurs under tension parallel to the c-axis or under compression perpendicular to the c-axis [54]. The twinning shear from equation (2.4) is 0.1289 and thus, the maximum tensile strain that twinning may accommodate is only 0.065 [34] not including double-twinning.

The interaction between prismatic or basal slip dislocations and a $\{10\bar{1}2\}$ twin or a $\{11\bar{2}1\}$ compressive twin is repulsive in Mg [1]. Therefore, the activation of slip or twinning during plastic deformation may result in pile up of dislocation that causes local stress concentrations. This stress concentration may enhance the process of twin nucleation and also twin growth [46]. Furthermore, twins can act as effective barriers against slip dislocation. These effects of dislocation and twin interactions are found to be more pronounced in hcp materials [46]. Therefore, it is extremely important to take these interactions into account in interpreting the mechanical behavior of Mg and its alloys. As a summary, the slip systems as well as the twinning system that are observed in Mg alloys are schematically shown in Figure 2.3.

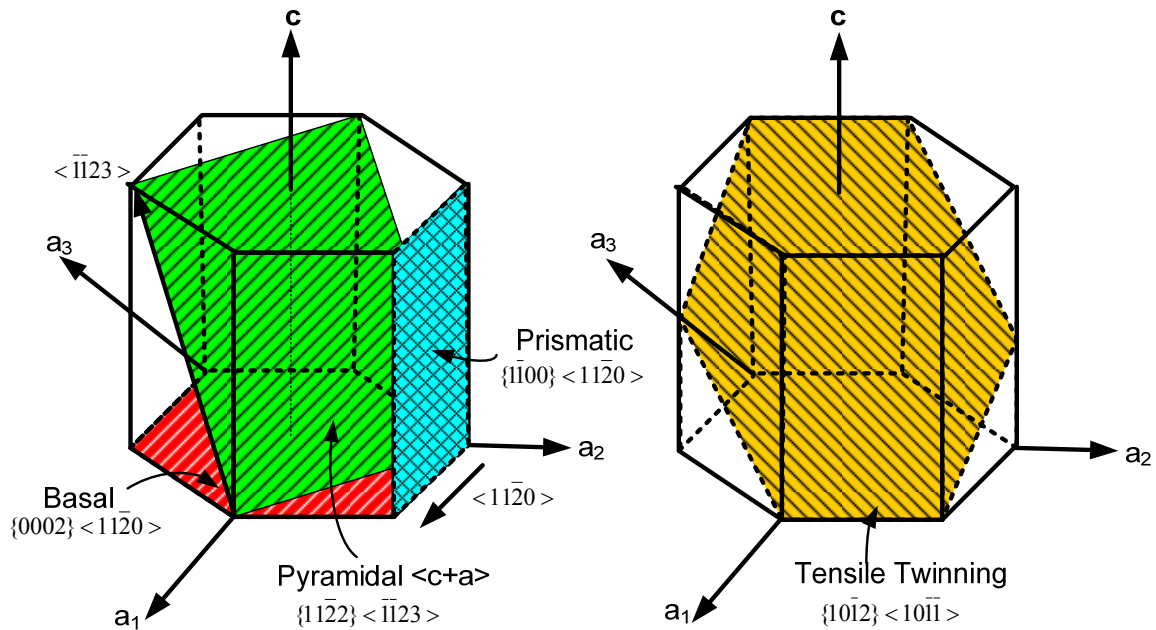


Figure 2.3 Schematic of slip and twinning systems observed in Mg alloys.

2.2.2 Equal channel angular extrusion of magnesium alloys and dynamic recrystallization

To overcome some of the limitations of Mg alloys, several processing techniques have been utilized. One such processing technique is equal channel angular extrusion (ECAE) which has been extensively used to increase the strength and ductility of many materials by refining the microstructure via severe plastic deformation. As discussed in section 2.1, ECAE is a very efficient grain refining technique. Moreover, ECAE is, currently, the only severe plastic deformation method that is able to produce different kinds of crystallographic textures on the same materials by using different processing routes, number of passes and die angles. Therefore, several Mg alloys have been

processed using (ECAE). Due to their hexagonal close-packed (hcp) structure and hence their limited ductility, Mg alloys are usually processed at high temperatures. Since they have relatively low melting temperature, the homologous temperature is relatively high for these alloys, therefore, dynamic recovery and recrystallization take place during processing and hence, decrease the efficiency of ECAE or other SPD processing in grain refinement and improvement of mechanical properties. Mukai et al. [55] were the first to report ductility improvement in AZ31 alloy after eight ECAE passes at 200 °C following route B_C, as can be seen in Figure 2.4. The tested sample exhibited remarkable strain hardening and a large uniform elongation to failure (about 45%) when tested parallel to the extrusion direction (ED) [55]. They attributed the improvement in ductility to the equal distribution of the basal poles with respect to both the extrusion and normal directions of the ECAE processed sample. However, this equal distribution of basal planes should not be assumed as randomization of strong extruded texture [14]. Agnew et al. [14] repeated the same processing on a conventionally extruded AZ31B alloy and found that despite the fact that the volume fractions of grains having basal poles parallel or perpendicular to the extrusion axis are quite low, the texture is in fact strong. They found that the texture strength was increased from 1.7 multiple of random distribution (mrd) in the conventional extrusion to about 2.3 mrd in the ECAE processed alloy. The texture of the AZ31 alloy ECAE processed by Agnew et al. [14] is shown in Figure 2.5. It is important to note that Mukai et al. [55] and Agnew et al. [14] have annealed the ECAE processed samples to increase the grain size to that of as conventionally extruded samples. This annealing might contribute to the high improvement in ductility.

Moreover, comparing the response of conventionally extruded sample and that of ECAE processed, it is clear that the governing mechanisms are different in the two samples. They strain harden because of slip and twinning, respectively. Barnett [12] concluded from the study of tensile twinning, that this type of twinning increase the uniform elongation of the sample and therefore, increase its elongation to failure. Therefore, more comprehensive studies need to be conducted to understand the effects of ECAE on the ductility of Mg alloys.

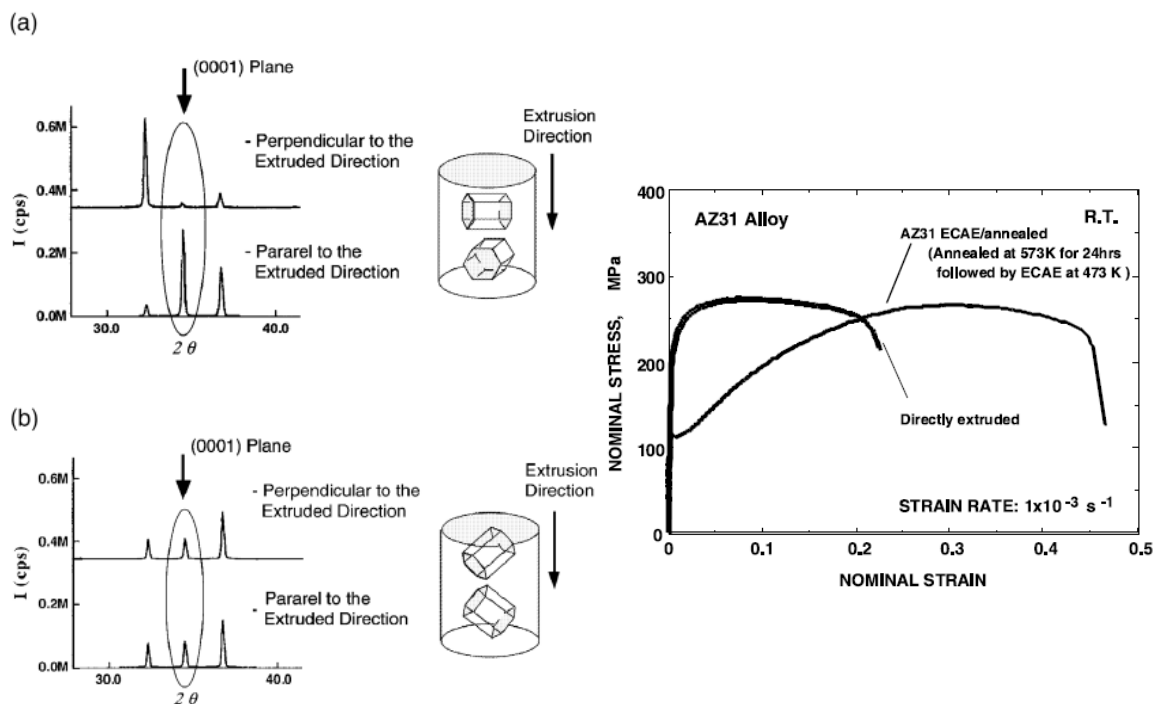


Figure 2.4 X-ray diffraction spectra of (a) directly extruded AZ31 Mg alloy and (b) the ECAE processed and annealed AZ31 alloy. (c) Nominal stress-strain response of AZ31 alloy after direct extrusion and after annealing following ECAE [55].

Motivated by this remarkable increase in ductility, several Mg alloys have been processed using ECAE including pure Mg [56-58], AZ31 [14, 59-61], AZ60 [59], AZ61 [62], AZ80 [59], ZK60 [59], WE43 [59] and Mg-3.3%Li [63]. Figure 2.6 summarizes the results of ECAE studies on Mg alloys to improve their strength and ductility.

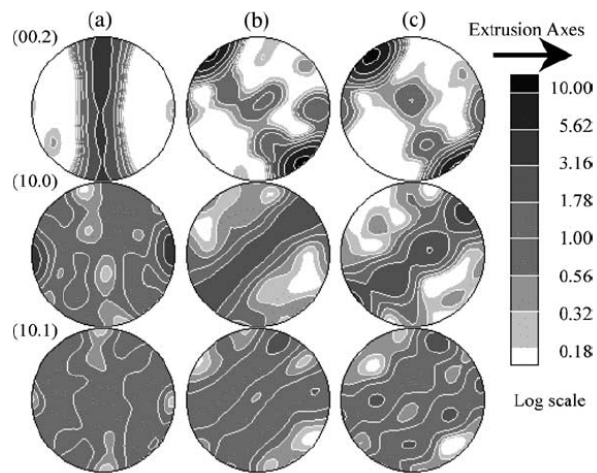


Figure 2.5 Pole figures (equal area projection) show the crystallographic textures in: (a) conventionally extruded, (b) ECA processed and (c) annealed AZ31B as determined by neutron diffraction [14]. The extrusion axes are to the right.

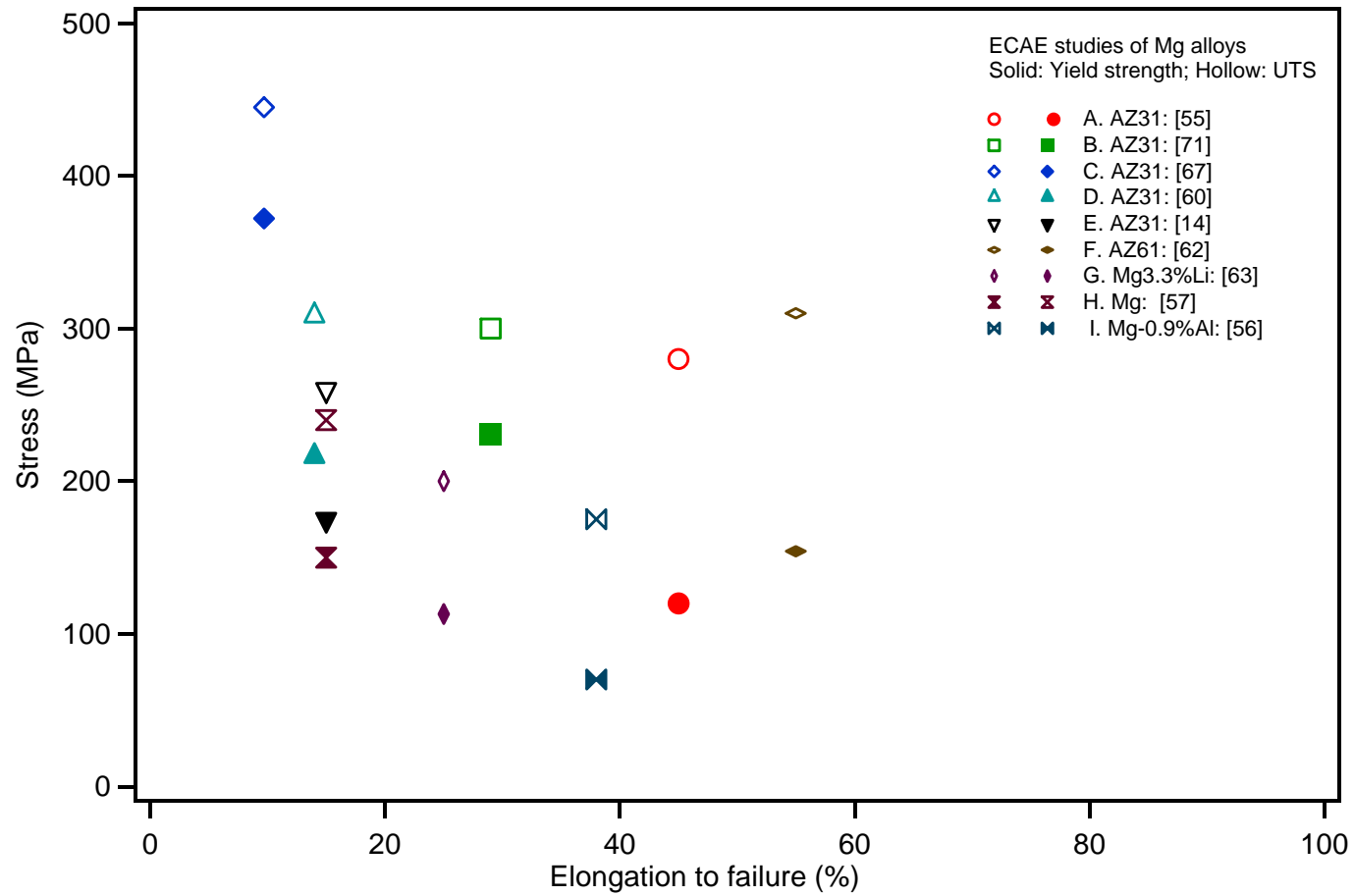


Figure 2.6 A summary of ECAE studies on improving the mechanical properties of Mg alloys. Solid and hollow symbols represent yield and ultimate stresses, respectively.

In most of the aforementioned studies, ECAE processing of Mg alloys was carried out at temperatures of 200 °C or above, which for Mg are sufficiently high homologous temperatures that can potentially trigger dynamic recrystallization (DRX). It is well known that DRX occurs most readily in materials in which recovery is slow, e.g. in materials of medium or low stacking fault energy (SFE). The SFE of magnesium is relatively high especially for prismatic and pyramidal (about 32-36 mJ/m² for basal plane [64, 65], 265 mJ/m² for prismatic [64] and 344 mJ/m² for pyramidal [64]) stacking faults, and therefore, it is expected to soften by dynamic recovery rather than recrystallize. However, Ion et al. [66] found that DRX indeed takes place during high temperature deformation of Mg and this they ascribed to the constraints imposed by the lack of easily activated slip systems rather than the effect of SFE. Since DRX leads to new strain-free grains, it can be undesirable for achieving high yield strength in Mg alloys. In order to prevent or limit DRX, the material should be deformed at the lowest possible temperature at least at the final stages of processing. However, DRX can also be utilized to introduce fine grains in the materials before further processing at lower temperatures. It has been found that AZ31B can be ECAE processed at relatively low temperatures following higher temperature processing [67, 68]. This is partially because of the fine DRX grains introduced during the initial high temperature processing stages stimulating additional deformation mechanisms such as grain boundary sliding [69, 70], which can help reduce shear localization and enhance formability at low temperatures.

Jin et al. [71] indeed showed that it is necessary to process AZ31B alloy at low temperature after high temperature ECAE in order to prevent dynamic recovery and

DRX and hence to preserve dislocations in the interior of grains and at the grain boundaries. They ECAE processed the alloy at 180 °C for one pass following four ECAE passes via route B_C at 225 °C. This reduction in processing temperature was found to be very effective in preventing dynamic recovery (see Figure 2.7) and hence increasing the yield strength of the alloy to 231 MPa from 152 MPa of that processed by five passes at 498K. Xia et al. [60], also, ECAE processed AZ31B alloy in two steps but to a higher number of passes using a 120° angle die. They processed the alloy up to four passes via route B_C at 150 °C with 0.2 mm/min extrusion speed followed by four passes following route B_C at 100 °C with the same speed. A grain size of 0.2-0.5 μm was achieved. However, there was no report on the mechanical properties of the processing at temperature lower than 200 °C other than microhardness which was increased after the low temperature processing. The most recent multi-step ECAE processing of Mg alloys is the study of Ding et al. [67] in which AZ31 alloy was extruded following four sequential steps: (1) four passes at 200 °C following route A; (2) four passes at 150 °C following route A; (3) two passes at 125 °C following route A; and (4) two passes at 115 °C following route A with rotating the billets by 180° between steps (1), (2) and (3), and by 90° between steps (3) and (4). They achieved a yield and ultimate tensile strengths of 372 MPa and 445 MPa, respectively along ED. No mechanical properties were reported along other billet directions.

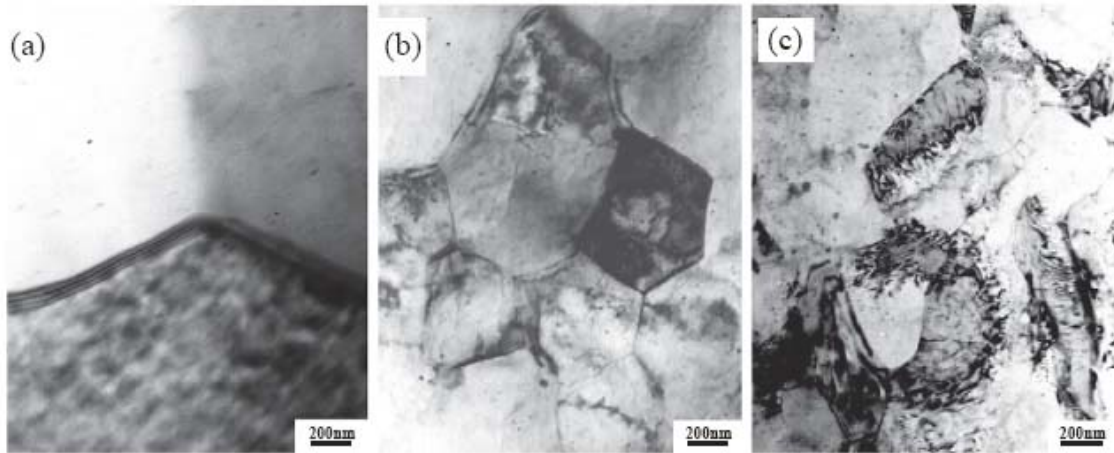


Figure 2.7 The TEM micrographs of (a) as-received AZ31 Mg alloy; the same alloy (b) after ECAE at 498 K for five passes; and (c) after two-step ECAE: 498 K for four passes following route B_C and one pass at 453 K [71].

2.2.3 Flow stress anisotropy and tension-compression asymmetry of ECAE processed Mg alloys

Agnew et al. [14] investigated the effects of texture on the flow stress anisotropy of AZ31B processed by ECAE by running tensile tests along various billet orientations. They found that the flow response is highly anisotropic and the flow stress and hardening behavior can be rationalized in terms of the strong crystallographic texture induced by ECAE processing (See Figure 2.8). This study however, was carried out only on materials ECAE processed up to 8 passes via route B_C. No study has been carried out to date to measure or predict the evolution of flow stress anisotropy, along different directions, as a function of the number of ECAE passes following different processing routes. Moreover, there is a lack of tension-compression asymmetry studies of these

alloys after ECAE processing. It is believed that amount of twinning activated during plastic deformation of Mg alloys will determine the degree of tension-compression asymmetry [52, 54, 72]. Therefore, one of the goals of this dissertation is to investigate the effects of twinning in both flow stress anisotropy and compression asymmetry by studying the mechanical behavior of several samples having different crystallographic textures.

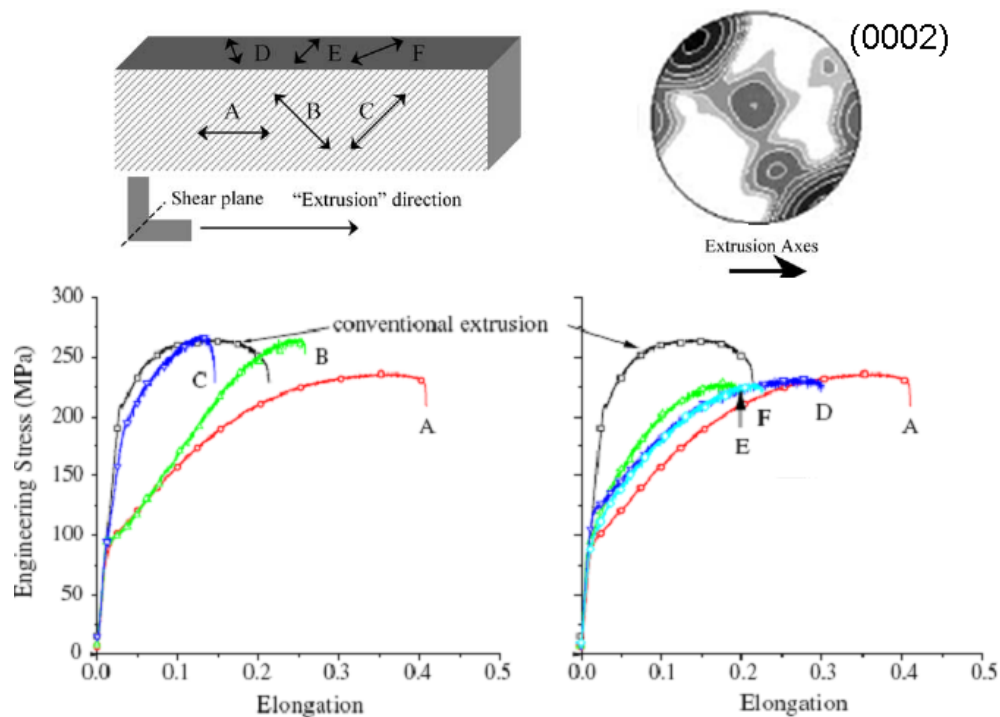


Figure 2.8 Tensile tests results from the AZ31B ECAE processed samples having a variety of orientations with respect to the ECAE processed bar shown in the upper left corner. Basal pole figure of the sample which is ECAE processed up to eight passes following route B_C and then annealed is shown on the upper right corner [14].

2.3 Zinc-aluminum Alloys as Two-phase HCP Materials

Zn-Al alloys are gaining increasing attention as potential substitutes for several ferrous and non-ferrous materials because of their good mechanical and tribological properties [73-77]. They have widely been used in bearings because of their excellent wear and damping properties, higher castability and lower energy requirement, and benefiting from superplasticity that some of these alloys, with ultrafine-grained structure, exhibit [17, 18, 78]. Zn-Al foundry alloys have several advantages over other commonly used casting alloys based on iron, aluminum and copper. For example their machinability is better than cast iron; they are harder and stronger than aluminum and much cheaper than copper.

Figure 2.9 shows the binary phase diagram of Zn-Al showing the Zn - 8wt.% Al which is the alloy investigated in this dissertation. Zn - 8wt.% Al alloy lies left side of the eutectic composition in the Al-Zn phase diagram where the primary phase is β which exists as numerous small and particulate dendrites in an eutectic matrix above the eutectoid temperature of 275 °C [79]. Upon cooling below the eutectoid temperature, the β phase decomposes into α and η giving its lamellar structure. Therefore, the microstructure of the as-cast alloy consists of a dendritic structure with eutectoid dendrites (fine $\alpha + \eta$ lamellae) dispersed in a eutectic matrix ($\alpha + \eta$ phase)

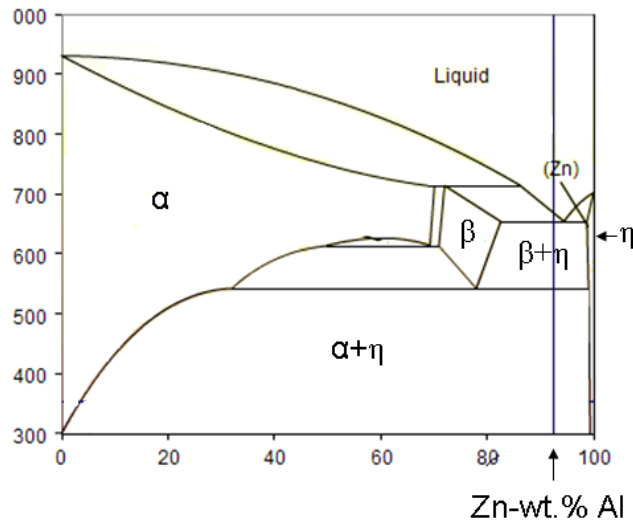


Figure 2.9 Phase diagram of Zn-Al alloys showing the Zn-wt.% Al alloy.

Zn-Al alloys, however, have inferior strength and poor ductility at low temperatures, and dimensional instabilities at elevated temperature [19, 80] that limit their use in some engineering applications. Several approaches have been reported to overcome these drawbacks such as addition of silicon [81], heat treatments [82, 83] and reinforcement with non-metallic compounds [84]. Recently, many attempts have been undertaken to improve the mechanical properties of Zn-Al alloys with the introduction of ultrafine grains (UFG) using ECAE [16-21].

2.3.1 Severe plastic deformation of Zn-Al alloys using equal channel angular extrusion

Kumar et al. [18] found that the maximum grain refinement in ZA22 can be achieved after the first ECAE pass. Furukawa et al. [17] also processed this (ZA22) alloy using two severe plastic deformation techniques: high-pressure torsion (HPT) and ECAE in order to find the most effective technique. Figure 2.10 shows the transmission electron

microscopy micrographs (TEM) in as received condition and after HPT and ECAE processing up to an equivalent strain of ~ 8 . As can be seen in the TEM micrographs, submicron grain sizes can be introduced using ECAE and HPT in the eutectoid ZA22 alloy. After eight ECAE passes at 100 °C following route B_C, the grains are elongated and there are agglomerates of Al-rich and Zn-rich grains with very limited mixing. On the other hand, after HPT, the grains are equiaxed and there is some mixing of the two phases. They attributed this limited mixing of the two phases in ECAE to the low pressure required in ECAE compared to HPT.

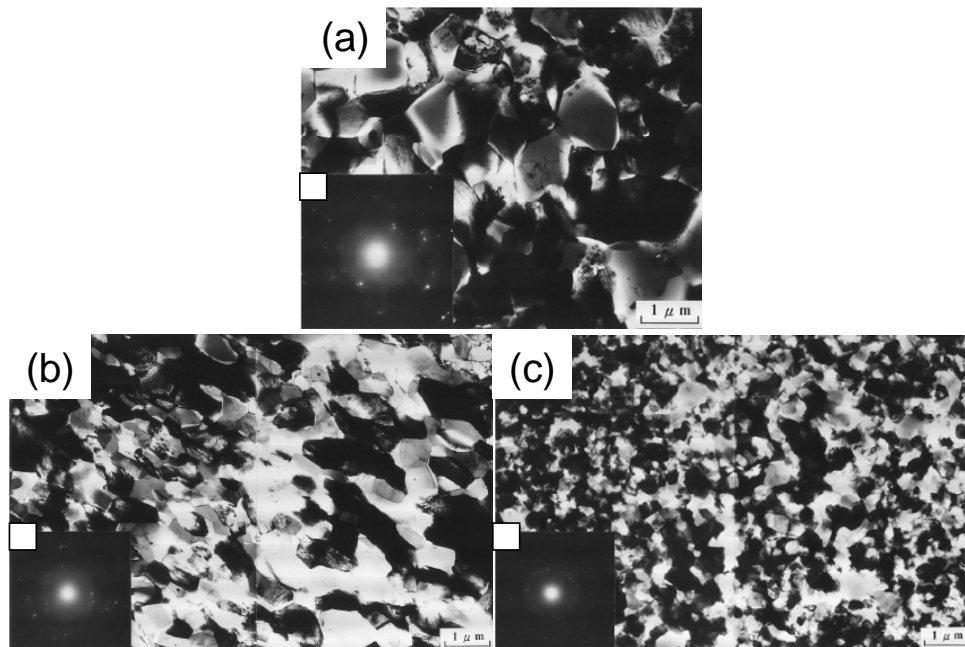


Figure 2.10 Microstructure of Zn-22wt.%Al (a) in as received condition where the bright and dark grains are Al-rich and Zn-rich, respectively, (b) after 8 ECAE passes and (c) after high pressure torsion [17].

Several Zn-Al alloys were investigated and processed using ECAE including: ZA-40 [15], ZA-27 [16], ZA-22 [17, 18], ZA-12 [19], ZA-8 [20] and ZA-5 [21]. Most of these studies have reported an increase in strength of the as-cast alloys after the first ECAE pass due to the reported microstructural refinement and the elimination of as-cast dendritic structure, but they also reported some notable decrease after further ECAE passes, even in some cases, to lower values than the as-cast strength levels. Figure 2.11 represents the evolution of the strength levels of different Zn-Al alloys with the number of ECAE passes. To the best of our knowledge, there is no clear understanding of why strength levels drop with further ECAE in the presence of the microstructural refinement. In addition, the effects of the composition and morphology of the hard second phase on the flow response of ECAE processed materials were not investigated. Therefore, one of the goals of the present dissertation is to improve the room temperature tensile properties of the ZA-8 alloy using lower temperature ECAE processing versus those previously reported, and to reveal the mechanisms for such possible changes, if any, in these properties. In order to mechanically rationalize these improvements in tensile properties after ECAE and to reveal the effect of different processing routes on these properties, a detailed investigation was carried out focusing on the composition, strength levels and morphology of the two constitutive phases.

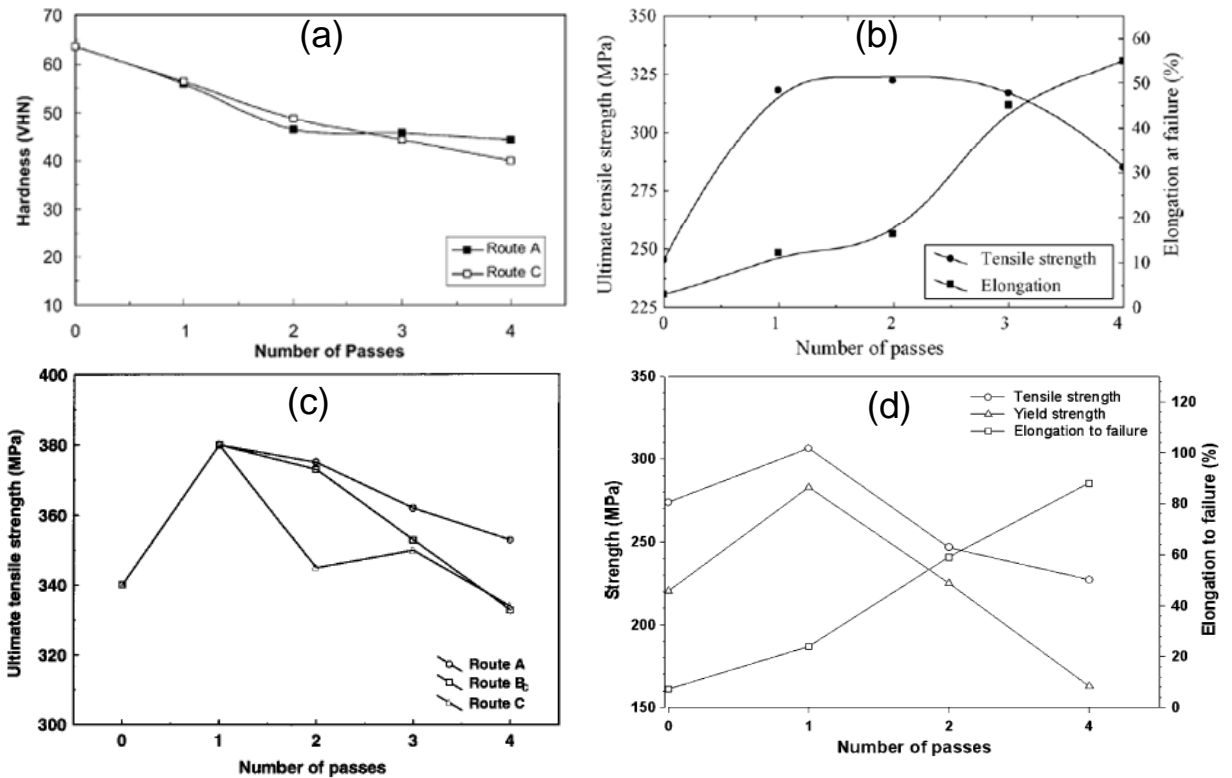


Figure 2.11 Evolution of strength levels with the number of ECAE passes, of (a) ZA5 [21], (b) ZA12 [19], (c) ZA27 [16] and (d) ZA40 [15].

2.4 Visco-plastic Self-consistent Crystal Plasticity Modeling

In addition to the experimental investigation, attempts to predict texture and grain morphology evolution during ECAE of AZ31B Mg alloy have been carried out. A visco-plastic self-consistent (VPSC) crystal plasticity model has been used to predict the texture and grain morphology as well as stress-strain response of this alloy. In this section, a brief introduction about this model is presented and for more details the readers are directed to the following references: Lebensohn and Tome' [27] and Texture and Anisotropy, chapter 11 by Tome' and Canova [85].

The basis of any plasticity model is the interaction of the grain with its surrounding. There are many modeling approaches that try to relate the grains with the polycrystalline aggregates. Full constraint (FC) approach or what is previously known as Taylor-Bishop-Hill assumption [38, 86] imposes the same deformation to every grain regardless of its anisotropy and therefore, the surrounding dictate the grain deformation [27]. Relaxed constraint (RC) [87] formulation, on the other hand, allows for some of the strain components to differ from the average ones. Relaxation in this approach is based on grain shape and stress continuity and not in relative stiffness of grain and matrix.

The visco-plastic self-consistent (VPSC) approach, however, treats each grain as an ellipsoidal visco-plastic inclusion embedded in and interacting with effective medium represented by the average response of all the grains. This treatment of each grain allows local equilibrium and compatibility to be satisfied, while maintaining computational efficiency [25]. Grains are paired at random at the beginning of the simulation and made to co-rotate to meet the strain compatibility at the grain boundaries using the so-called grain co-rotation scheme [88].

The effect of twinning on the texture evolution was treated inside the VPSC model using the so-called Predominant Twin Reorientation (PTR) scheme [89] in which the grain is fully reoriented when the most active twin system inside the grain reaches a threshold value. The PTR scheme has been replaced recently by a more realistic model called Composite Grain (GC) approach first presented by Proust et al. [90]. In CG approach, the twinned grain is considered as composite grain consisting of layers of twins and matrix (Figure 2.12). The CG approach, hence, allows accounting for the

directional barriers that specific twins poses to specific dislocations via a Hall-Petch (HP) effect [91].

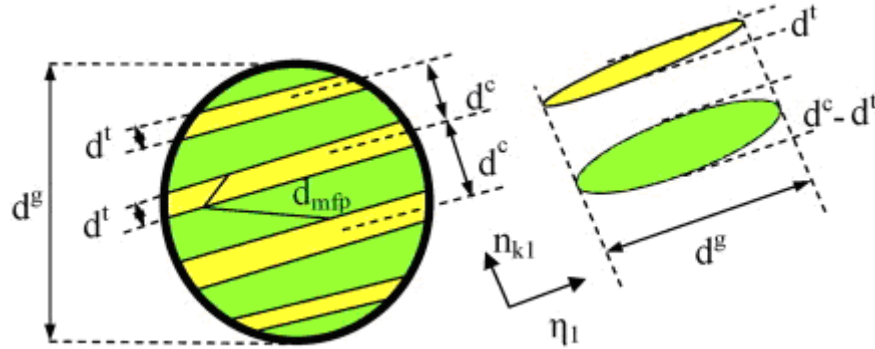


Figure 2.12 Schematic of the Composite Grain (CG) model implemented in VPSC to model twinning, showing morphology and orientation of twins and matrix, and indicating the parameters of the CG model [91].

2.4.1 VPSC modeling of ECAE process

The ECAE process used in this study was performed using a 90° die. A representation of the process with the reference coordinate systems used in the ECAE modeling is shown in Figure 2.13. According to the simple shear model of ECAE the velocity gradient of simple shear in the plane of symmetry (1'-2'-2' reference system in Figure 2.13) is given by:

$$L' = \begin{pmatrix} 0 & \dot{\gamma} & 0 \\ 0 & 0 & 0 \\ 0 & 0 & 0 \end{pmatrix} \quad (2.5)$$

Where $\dot{\gamma}$ is the constant applied strain rate. In global coordinate system 1-2-3, equation (2.5) is expressed as follow

$$L' = \frac{\dot{\gamma}}{2} \begin{pmatrix} 1 & -1 & 0 \\ 1 & -1 & 0 \\ 0 & 0 & 0 \end{pmatrix} \quad (2.6)$$

This velocity gradient describes tension in 1 (ED), compression in 2 (LD) and rigid body rotation about 3 (FD) [92].

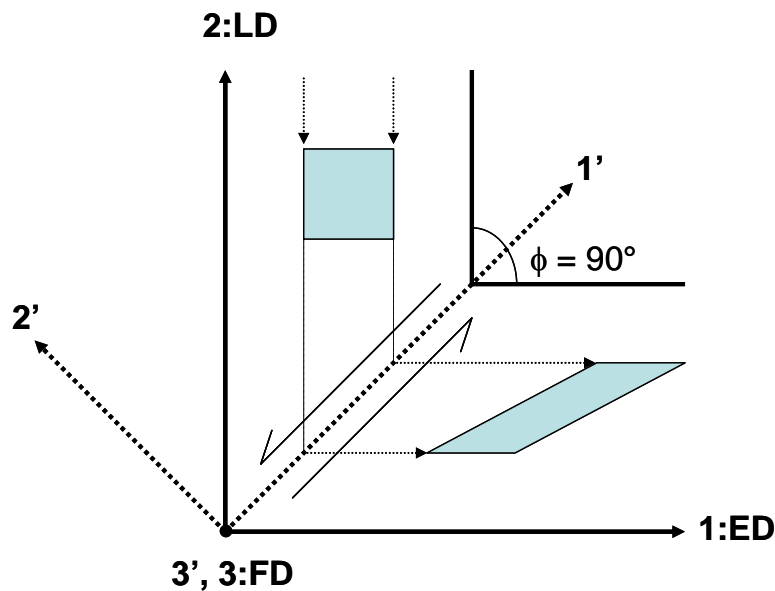


Figure 2.13 Reference coordinate systems used in the ECAE process showing the deformation of a square by simple shear at the intersection plane of the channels.

The aforementioned ECAE velocity gradient was obtained by assuming ideal simple shear. In reality, however, ECAE deformation can neither be described as a single shear along a single plane or as homogeneous [93]. In most cases, plastic

deformation during ECAE takes place in a broad zone whose shape depends on contact friction, material flow response, back-pressure, extrusion rate and die design [93].

2.4.2 Dislocation-based hardening model

The threshold stress, τ_s , describes the resistance for activation that the deformation modes experience at it usually increases with deformation (strain). The evolution of τ_s of each deformation mode is usually described by hardening functions. The most used of these functions is Voce hardening law which is characterized by the evolution of the threshold stress with the accumulated shear strain of each grain of the form

$$\hat{\tau}^s = \tau_o^s + (\tau_1^s + \theta_1^s \Gamma) \left(1 - \exp \left(-\Gamma \left| \frac{\theta_0^s}{\tau_1^s} \right| \right) \right) \quad (2.7)$$

where $\Gamma = \sum_s \Delta\gamma^s$ is the accumulated shear in the grain, and, τ_0 , θ_0 , θ_1 and $(\tau_0 + \tau_1)$ are the initial critical resolved shear stress (CRSS), the initial hardening rate, the asymptotic hardening rate and the back-extrapolated CRSS, respectively.

A recent single crystal constitutive hardening law for multiple slip and twinning modes was developed by Beyerlein and Tome [94]. For each slip mode α , a dislocation population is evolved explicitly as a function of temperature and strain rate through thermally-activated recovery and debris formation. This dislocation-based hardening law was implemented to predict compressive stress-strain response of clock-rolled pure Zr [94] and to investigate the twin growth mechanisms in Mg single crystals [50].

The shear increment $d\gamma^\alpha$ for each slip mode α is a straightforward sum of the shears of all slip systems contained in mode α at each time increment dt :

$$d\gamma^\alpha = \sum_{s \in \alpha} \left| \dot{\gamma}^s \right| dt \quad (2.8)$$

where

$$\dot{\gamma}^s = \dot{\gamma}_0 \left| \frac{m^s : \sigma}{\tau_c^s(\varepsilon, T)} \right|^n \text{sign}(m^s : \sigma) \quad (2.9)$$

This flow rule introduces a critical strength τ_c^t that depends on the local microstructure encountered by the dislocations. Equations (2.8) and (2.9) are also used to describe the kinematics of twinning in which τ_c^t is the directional threshold required to propagate the twin system $t \in \beta$. The exponent n is set high, $n=20$, so that slip or twinning is activated only when the resolved shear stress closely approaches the critical strength.

Work hardening is linked to the evolution of dislocations, their interactions with each other, and with barriers in the microstructure. Therefore, the critical strength or slip resistance of each slip $s \in \alpha$, τ_c^s evolves as follows:

$$\tau_c^s = \tau_0^\alpha + \tau_{forest}^\alpha + \tau_{deb}^\alpha + \tau_{HP}^s, \quad s \in \alpha \quad (2.10)$$

where τ_0^α is the initial slip resistance which depends on slip mode α , solute density, and T and $\dot{\varepsilon}$. The second and third terms on the right hand side of equation 2.10 represent the work hardening due to dislocation interactions. The last term, τ_{HP}^s , is the barrier

effect provided by grain or twin boundaries whichever constrains the mean free path of dislocations more.

An evolution model for dislocation density developed by Essman and Mughrabi [95] and further developed by Mecking and Kocks [96] was used to describe the dislocation density evolution and it is expressed as follow:

$$\frac{\partial \rho^\alpha}{\partial \gamma^\alpha} = k_1^\alpha \sqrt{\rho^\alpha} - k_2^\alpha(\dot{\epsilon}, T) \rho^\alpha \quad (2.11)$$

where k_2^α is calculated as follow:

$$\frac{k_2^\alpha(\dot{\epsilon}, T)}{k_1^\alpha} = \frac{\chi b^\alpha}{g^\alpha} \left(1 - \frac{kT}{D^\alpha b^3} \ln \left(\frac{\dot{\epsilon}}{\dot{\epsilon}_0} \right) \right) \quad (2.12)$$

where χ is an interaction parameter between 0.1 and 1.0, b is the Burger vector, D is a proportionality factor of unit of stress, g is normalized stress-independent activation energy and k is the gas constant. The third term on the RHS of equation 2.10 which is the contribution of ρ_{deb} is expressed as follow

$$\tau_{deb}^\alpha = k_{deb} \mu b^\alpha \sqrt{\rho_{deb}} \log \left(\frac{1}{b^\alpha \sqrt{\rho_{deb}}} \right) \quad (2.13)$$

Where k_{deb} is a material-independent constant determined to be 0.86 [97] and ρ_{deb} evolves with plastic strain as follow

$$\partial \rho_{deb, tot} = q \sum_\alpha f^\alpha \frac{\partial \rho_{rem}^\alpha}{\partial \gamma^\alpha}, \text{ and } f = \frac{nb^\alpha}{l_{deb}} \approx A^\alpha b^\alpha \sqrt{\rho_{deb}} \quad (2.14)$$

where $A = Q_0 + Q_1 \ln(1 + T/Q_3)$.

Therefore, the resistance to slip of each system $s \in \alpha$ evolves from a zero-strain value calculated to be:

$$\tau_c^s(\gamma = 0) = \tau_0^\alpha(T) + \mu HP^\alpha \sqrt{\frac{b^\alpha}{d_g}} + b^\alpha \chi \mu \sqrt{\rho_0^\alpha} \quad \forall s \in \alpha \quad (2.15)$$

assuming no twins are present and the amount of debris is negligible, to a final value of

$$\tau_c^s = \tau_0^\alpha(T) + \mu HP^{\alpha\beta} \sqrt{\frac{b^\alpha}{d_{mfp}^{s,PTS}}} + b^\alpha \chi \mu \left[\sqrt{\rho^\alpha} + \frac{k_{deb}}{\chi} \sqrt{\rho_{deb}} \log \left(\frac{1}{b^\alpha \sqrt{\rho_{deb}}} \right) \right] \quad \forall s \in \alpha. \quad (2.16)$$

CHAPTER III

EXPERIMENTAL PROCEDURES

In this chapter, the materials investigated in this work are listed in more details. The detailed experimental procedures are presented for each material separately. Lists of all processing and characterization experiments are also included in this chapter.

3.1 Materials

In this study, two alloys have been studied for the flow stress anisotropy and tension-compression asymmetry of hexagonal closed packed (hcp) materials. They were processed using thermomechanical processing in order to produce variety of samples that have different microstructures and crystallographic textures. The first alloy is an AZ31B Mg alloy (2.5-3.5 wt.% Al, 0.7-1.3 wt.% Zn, 0.2-1.0% Mg and balance-Mg) obtained from a hot rolled plate. This Mg alloy is the most widely available commercial alloy. It has been selected for this study because it is the most used Mg alloy in engineering applications and because it exists as one-phase which make it easier to study and model. The second alloy is Zn-8wt% Al (or shortly ZA-8) alloy obtained from as cast ingots having a nominal composition of 8.32% Al, 1.11% Cu, 0.024% Mg, 0.006% Fe, 0.0028% Pb, 0.001 Sn, less than 0.001% Cd in weight and balance Zn. This alloy was selected because it is a two-phase alloy having an hcp matrix. In addition to this matrix, it has a second hard phase Al-rich phase which has a face centered cubic structure. Therefore, flow anisotropy study was conducted on this alloy with respect to

the orientation of the second hard phase. Detailed experimental procedures for both alloys are listed in the following sections.

3.2. Thermomechanical Processing of AZ31B Mg Alloy Using Equal Channel Angular Extrusion

Material billets with a cross-section of 25 mm × 25 mm and a length of 150 mm were machined from the hot rolled AZ31B. The billets were ECAE processed with an extrusion rate of 0.075 mm/s at 200 °C isothermally in the presence of 30 MPa back-pressure. These ECAE parameters were found, after many trials, to be necessary to process the alloy up to four ECAE passes without shear localization or major cracks. A die having a sharp 90° corner angle was used. The hot rolled sample had a strong basal texture aligned with the plate normal. In order to reveal the effects of starting texture on microstructure and texture evolution during ECAE, the billets were processed with basal poles parallel to either the extrusion direction (ED) or the flow direction (FD). Figure 3.1 shows the schematics of the two processing conditions with hexagonal unit cell representing the orientation of the majority of the grains. Figure 3.1 also presents the starting textures in the die coordinate frame for both cases. These two processing conditions will be called 1A-I and 1A-II, respectively in the remaining of the text. Second and fourth ECAE passes were also conducted, to see the effects of ECAE routes on texture and to produce samples having different textures than those obtained after the first ECAE pass, on additional billets following the well established conventional ECAE routes A, C, E and B_C, with a starting textures the same as 1A-I before the first pass. In route A, the billet is reinserted into the die without any rotation, but in routes C and B_C,

the billet is rotated about its extrusion axis by 180° and 90° , respectively, before the successive pass. Route E is a combination of the routes C and B_C , where the billet is rotated around its extrusion axis by 180° before even-numbered passes and by 90° before odd-numbered passes. In addition to these rotations dictating the route, there is also unavoidable 90° rotation of the billet about its flow direction when it is inverted back to the vertical insertion orientation before the following pass. Details on the ECAE processing in general are presented in Chapter II. ECAE parameters for all passes were the same as those of 1A-I and 1A-II. These will be designated as xY-I, where x is the number of passes conducted on the billet, Y is the route designation (A, C, B_C or E) and I represents the starting texture of basal poles parallel to the ED as shown in Figure 3.1.a. All billets were heated to the processing temperature of 200°C for 20 minutes before the first pass and 15 minutes before additional passes. They were water quenched directly after each pass. All extrusions conducted on AZ31B alloy are listed in Table 3.1.

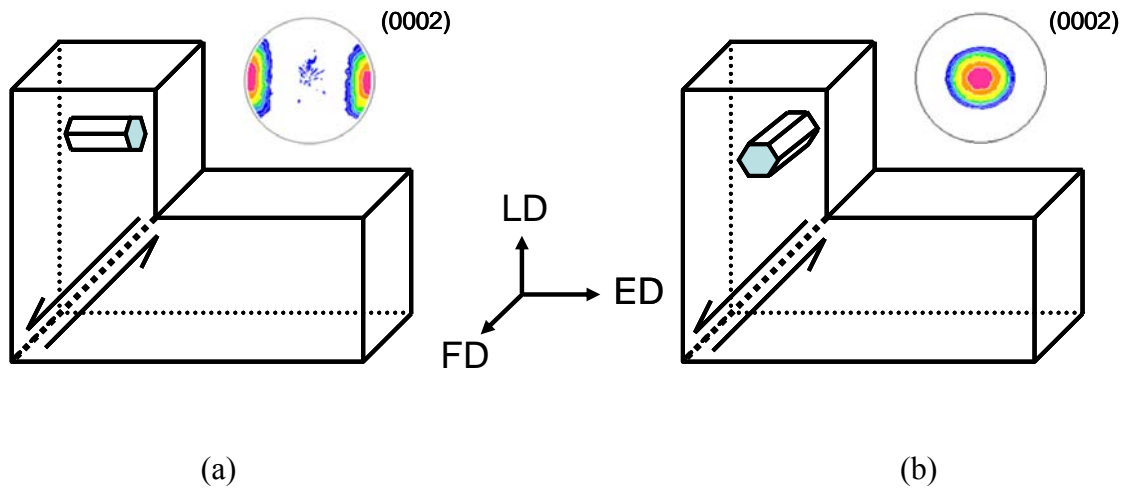


Figure 3.1 Schematics of the two extrusion cases, (a) 1A-I: the starting basal poles are parallel to the ED and (b) 1A-II: the basal poles are parallel to the FD.

Table 3.1 A list of ECAE experiments carried out on AZ31B and ZK60A Mg alloys.

Route	1 pass	2 passes	4 passes	ECAE parameters			Number of Billets
				Temperature (°C)	Speed (mm/s)	Back- Pressure (MPa)	
A	1A	2A	4A	200 °C	0.075	30	4
C		2C	4C	200 °C	0.075	30	3
B _C		2B _C	4B _C	200 °C	0.075	30	3
E			4E	200 °C	0.075	30	2
Total Number of billets							12

3.2.1 Microstructural characterization of as received and processed AZ31B alloy

Optical microscopy and crystallographic texture measurements were performed on the samples cut from the fully deformed region of the billets with surfaces parallel to the flow plane which is perpendicular to flow direction (FD) (Figure 3.1). Texture measurements were carried out using X-ray diffraction with a Bruker AXS D8 Discover Diffractometer with Cu-K α radiation at 40 kV and 40 mA. For optical microscopy, the samples were mechanically polished down to 0.1 μm and etched using a solution that is composed of 10 mL acetic acid, 4.2 g picric acid, 10 ml H₂O and 70 ml ethanol. The optical micrographs were taken using a Keyence VHX-600K digital microscope.

3.2.2 Mechanical testing of as received and processed AZ31B alloy

Dog-bone shaped tension specimens with nominal gage dimensions of 8 mm \times 3 mm \times 1.5 mm and rectangular prism compression specimens with nominal dimensions of 4 mm \times 4 mm \times 8 mm were prepared using wire electrical discharge machining (EDM) from the fully deformed region of the extruded billets (see Figure 3.2). All samples were polished using 600 grit size carbide paper to get rid of EDM surfaces. The tension and compression tests were performed at room temperature along the three orthogonal directions of the ECAE billets: ED, FD and longitudinal direction (LD) as shown in Figure 3.2. The experiments were conducted under strain rate control with a rate of $5 \times 10^{-4} \text{ s}^{-1}$. At least three compression and tension specimens were used to validate the repeatability of the experiments. A list of all characterization and testing experiments performed on as received and processed AZ31B Mg alloy are listed in Table 3.2.

3.3 Thermomechanical Processing of Zn-8wt.% Al Alloy Using Equal Channel Angular Extrusion

The material billets with a cross section of 25 mm × 25 mm and a length of 150 mm were cut from as-cast ZA-8 ingot. The billets were extruded using an ECAE die having a sharp 90° corner angle at an extrusion rate of 0.25 mm/s, reported in the literature, for up to eight passes following various processing routes listed in Table 3.3. The eight passes were selected because it was found in our previous works on bcc [98], fcc [9] and hcp [5] single phase materials that eight passes are necessary to assure high volume fraction of high-angle grain boundaries and stable mechanical response. Processing temperatures were 80 or 100 °C (corresponding to the homologous temperatures of 0.52 to 0.55 T_m), the lowest possible temperatures for extrusion of this alloy without cracking after eight passes. The billets were kept in the die at the extrusion temperature for 30 minutes before the first pass and 15 minutes before the subsequent passes. They were water quenched directly after each pass.

Table 3.3 A list of ECAE and characterization experiments conducted on Zn-8wt.% Al alloy.

Extrusion Route	Material Composition (wt. %)	Initial Condition	Extrusion temperature	Extrusion Rate (mm/s)	Characterization			
					OM: Optical Microscopy	WDS: Wavelength Dispersive Spectroscopy	MH: Vickers Micro-Hardness	T: Tension
8C	Zn-Al (8%)	As-Cast	80 °C	0.254	OM	WDS	MH	T
8B _C	Zn-Al (8%)	As-Cast	100 °C	0.254	OM	WDS	MH	T
8E	Zn-Al (8%)	As-Cast	100 °C	0.254	OM	-	-	T
8B _A	Zn-Al (8%)	As-Cast	100 °C	0.254	OM	-	-	T
8 B _C	Zn-Al (8%)	As-Cast	100 °C	0.254	OM	-	-	T
8 B _C	Zn-Al (8%)	As-Cast	80 °C	0.254	OM	WDS	MH	T
8E	Zn-Al (8%)	As-Cast	80 °C	0.254	OM		-	T
16 B _C	Zn-Al (8%)	As-Cast	100 °C	0.254	OM		-	T
1 B _C	Zn-Al (8%)	As-Cast	80 °C	0.254	OM	WDS	MH	T
2 B _C	Zn-Al (8%)	As-Cast	80 °C	0.254	OM	WDS	MH	T

3.3.1 Microstructural characterization of as received and processed Zn-8wt.% Al alloy

The microstructural evolution of the ZA-8 alloy was monitored using optical microscopy and scanning electron microscopy (SEM). The samples were obtained by sectioning the processed billets parallel to their flow plane, and then prepared using standard metallographic techniques down to 0.05 μm aluminum powder. The specimens

were then etched using nital solution composed of 1 mL nitric acid and 100 mL H₂O. The optical micrographs were taken using a Keyence VHX-600K digital microscope. The SEM micrographs were taken using Cameca SX50 electron microscope.

Wavelength Dispersive Spectroscopy (WDS) and microhardness measurements were carried out on the mechanically polished samples, down to 0.05 μm aluminum powder, cut from the as-cast and processed billets parallel to the flow plane. Microhardness measurements were carried out at a load of 200 mN. The compositional analyses were carried out on a four spectrometer Cameca SX50 electron microprobe at an accelerating voltage of 15 kV at a beam current of 10 nA.

3.3.2 Mechanical testing of as received and ECAE processed Zn-8wt.% Al alloy

For room temperature tension experiments, flat dog bone shaped tension samples with a gage section of $2.0 \times 3.0 \times 8.0 \text{ mm}^3$ were cut from the homogeneously deformed volume [99] using wire electrical-discharge machining (EDM) having their tensile axes parallel to the extrusion direction. In the 1A, 2B_C and 8B_C ECAE samples, tension specimens were also cut parallel and perpendicular to the long axis of the elongated hard eutectoid phase particles or bands. Tension tests were carried out at room temperature on an MTS test frame at a strain rate of $5 \times 10^{-4} \text{ s}^{-1}$. A contact extensometer with 8 mm gauge length was used to measure the strain. Three to four companion specimens were tested to confirm the repeatability of the experiments.

CHAPTER IV
FLOW STRESS ANISOTROPY AND TENSION COMPRESSION
ASYMMETRY OF ECAE PROCESSED AZ31B MG ALLOY

AZ31B Mg alloy is ECAE processed starting with two different crystallographic textures and up to two ECAE passes following routes A, C and B_C. A visco-plastic self-consistent (VPSC) crystal plasticity model is used to predict texture and grain morphology evolution during ECAE. Simulation of ECAE process using VPSC model helps understand the governing deformation mechanisms and the effects of these mechanisms on the resulting microstructure and texture. It is demonstrated that dynamic recrystallization during high temperature ECAE is highly dependent on the starting texture with respect to the die geometry and hence to the slip systems activated during ECAE. The crystallographic texture of the processed samples also depends on the starting texture and the rotation of the billet between successive passes, i.e. ECAE routes. The evolved texture after ECAE is found to be the main reason responsible for flow stress anisotropy and tension-compression asymmetry.

4.1 Microstructure Evolution

As can be seen in Figure 4.1.a, the starting material has an average grain size of 25 μm . The grains size is still not uniform throughout the specimen. As expected for hot rolled Mg plate, it has strong basal texture in which basal poles are parallel to the normal direction of the plate.

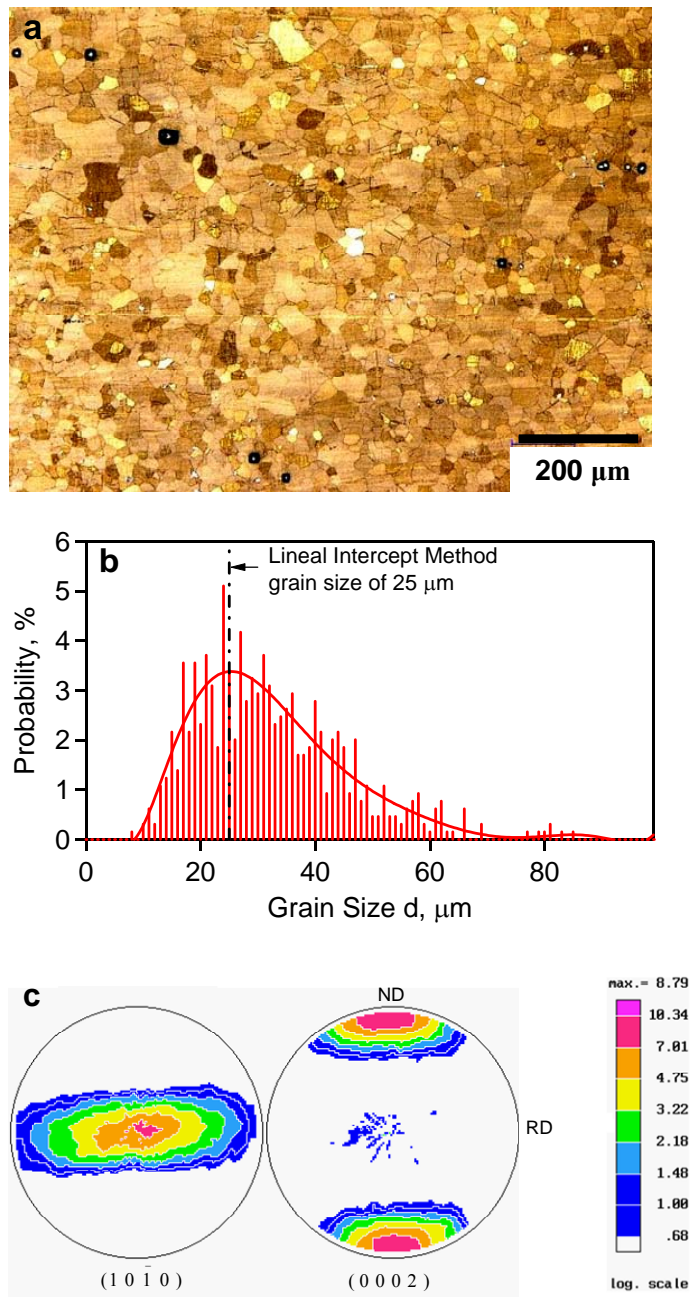


Figure 4.1 (a) The microstructure, (b) grain size distribution, and (c) texture of the starting AZ31B Mg alloy.

The optical micrographs of the processed samples taken from the flow plane of the billets of 1A-I and 1A-II are shown in Figure 4.2. The grains in the 1A-II sample are elongated and have an inclination angle of about 25-29° from the extrusion direction. A theoretical inclination angle of 26.6° from the ED has been calculated after the first ECAE pass of crystalline materials [23]. Two dynamically recrystallized and deformed regions are indicated in Figure 4.2. As shown, DRX took place in both cases but it is more prevalent in 1A-I. In 1A-II, we observe “necklace” type DRX starting in which small DRX grains are located along the grain boundaries of larger deformed grains. Figure 4.2 clearly indicates that starting texture has a substantial effect on DRX, grain morphology, and grain size.

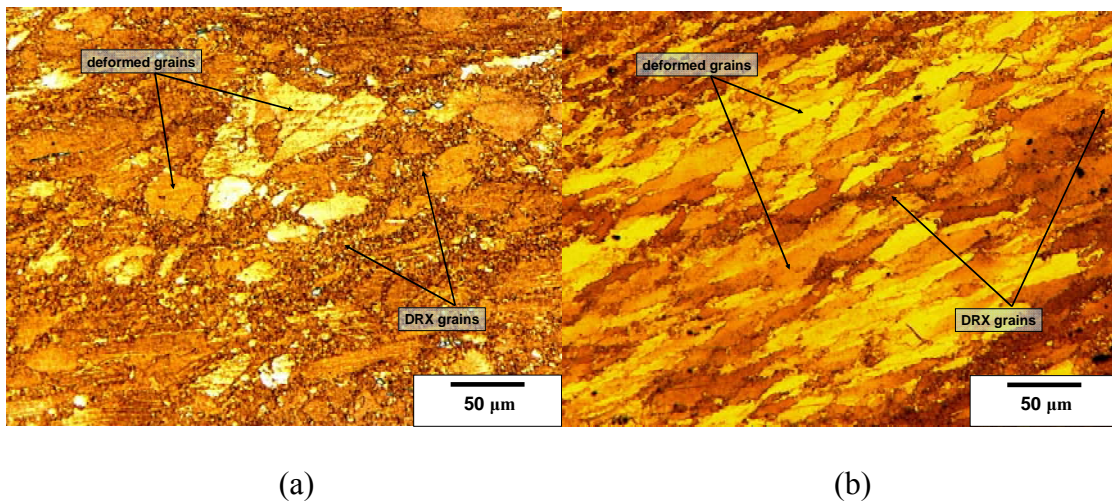


Figure 4.2 Optical micrographs of AZ31B ECAE samples processed starting with basal poles (a) parallel to the extrusion direction (1A-I) and (b) parallel to the flow direction (1A-II). The extrusion direction is to the right.

Figure 4.3 shows the microstructure of samples after the second pass of (a) 2A-I (b) 2C-I and (c) 2B_C-I. The grain morphologies developed in the 2A-I and 2C-I samples are similar to those in the 1A-I sample. It appears, however, that they have a higher amount of DRX than the 1A-I sample, although it is difficult to extract the exact volume fractions of DRX and non-DRX regions from these OM images. In contrast, the grain morphologies in 2B_C-I sample (Figure 4.3,c) are unlike those developed after the first pass (1A-I). In fact, they appear to be similar to those of the 1A-II sample in shape but finer. Also, unlike 2A-I and 2C-I, the amount of DRX in 2B_C-I is not significantly different than that of 1A-I, suggesting that most of the DRX observed in the 2B_C-I sample may have taken place during the previous pass.

4.2 Crystallographic Texture

Figure 4.4 shows the measured basal and prismatic pole figures of the first-pass AZ31B 1A-I and 1A-II samples. Starting texture I or II had a pronounced effect on the texture developed after one extrusion. In 1A-I, the grains have their c-axes more or less distributed about the LD with two peaks, one located about 5° clockwise from the LD and the other about 33° away, counter-clockwise, as shown in Figure. 4.4.a. The position of the two peaks at the rim of the pole figure indicates that the basal plane normals of most grains are almost perpendicular to the FD and the ED, but, the secondary peak makes an angle of about 57° from the ED. On the other hand, in the 1A-II sample the c-axes of most of the grains are spread around the FD towards a pole that makes 20-30° angle with LD counterclockwise.

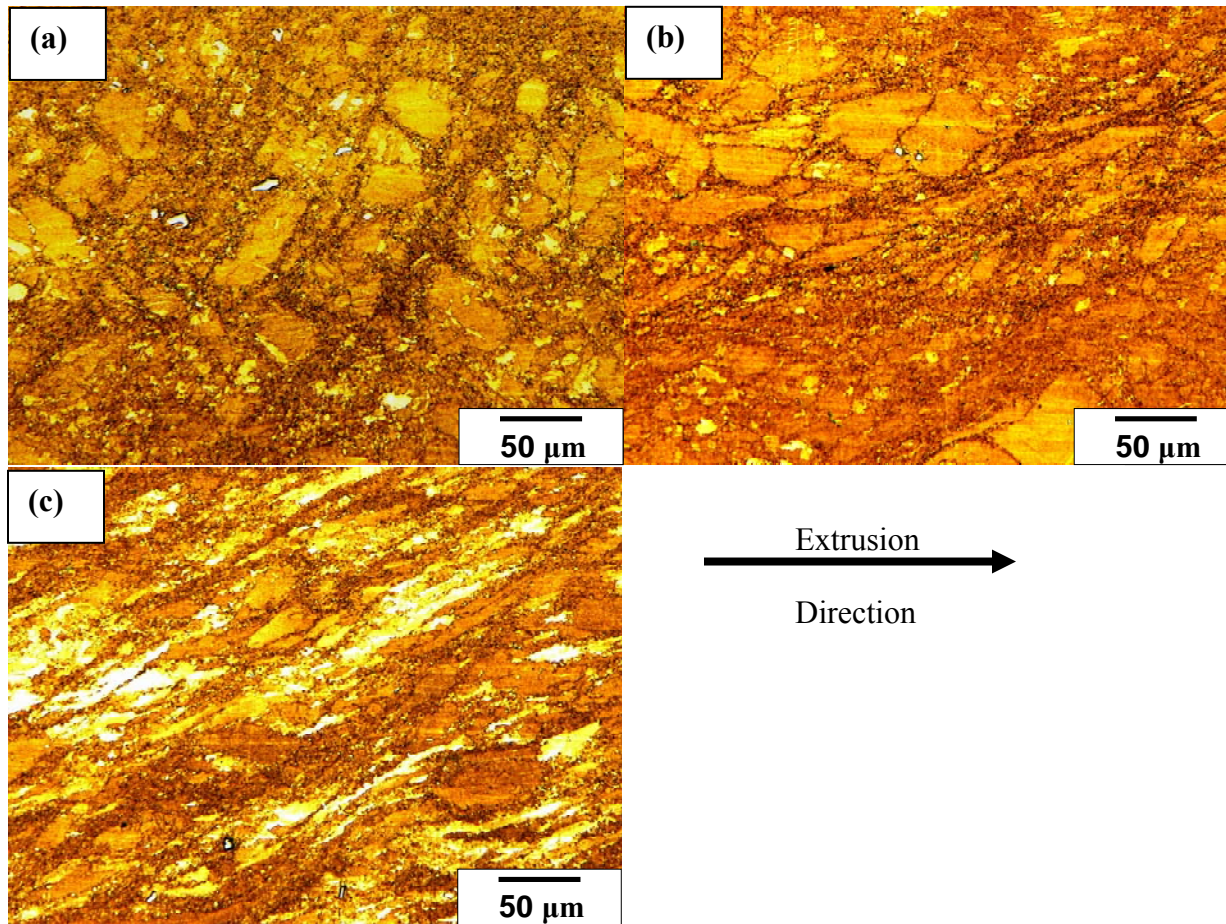


Figure 4.3 Optical micrographs of AZ31B ECAE samples processed starting with basal poles parallel to the extrusion direction and up to two ECAE passes following route (a) A (2A-I), (b) C (2C-I) and (c) BC (2BC-I).

In spite of their differences, textures of 1A-I and 1A-II both have a strong alignment of the basal poles approximately 20° to 30° from the LD. This is a common feature in one-pass textures of many HCP materials regardless of the c/a ratio [4, 26, 100-104]. Yapici and Karaman [4] found that other hcp materials, such as pure Zr, pure Be and Ti-6Al-4V alloy, have a similar texture evolution as AZ31B alloy, but without the basal peak split. Later it was proposed in [26, 100, 103] that this similarity is due to the prevalence of basal slip during ECAE processing. In the case of 1A-II, the alignment process is incomplete due to the influence of the starting texture. Yet the resulting texture is quite similar to one observed in Zr [103] with the same starting texture.

The basal and prismatic pole figures of the 2A-I, 2C-I and 2B_C-I samples are shown in Figure 4.5. For the second pass, the effect of ECAE route on texture evolution can be examined. As shown, the 2A-I and 2C-I textures have many features similar to those of the 1A-I texture. For instance, they are centro-symmetric and most of the basal poles are aligned about the LD into two peaks. The important difference, however, is the angle between these two maxima. As indicated, the angles between the two peaks are 32° and 62° for the 2A-I and 2C-I cases, respectively. The 2B_C-I texture is strikingly different than those of 2A-I and 2C-I. The symmetry found in 1A-I, 2A-I, and 2C-I is lost. In this case, the 90° rotation of the billet about its ED before the second pass in route B_C orients the basal poles parallel to near FD similar to the starting texture of case II. Accordingly, it is not surprising that the 2B_C-I texture is similar to the 1A-II texture.

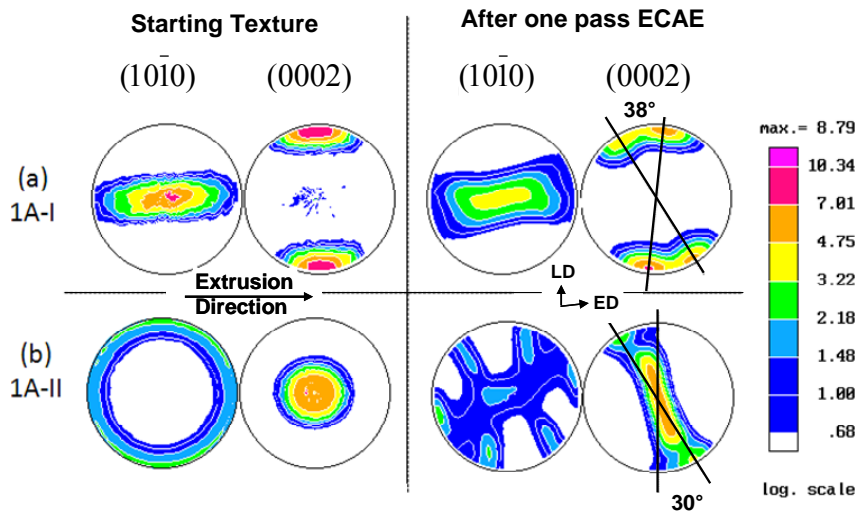


Figure 4.4 Prismatic and basal pole figures of starting and ECAE processed AZ31B Mg alloy after one ECAE pass with two different initial textures. (a) In the 1A-I case, most grains have c-axes parallel to LD. There is also a secondary peak in the basal pole figure making an angle of about 35° about LD. (b) In the 1A-II case, the basal poles are more spread around FD towards a pole that makes a 27° angle with LD.

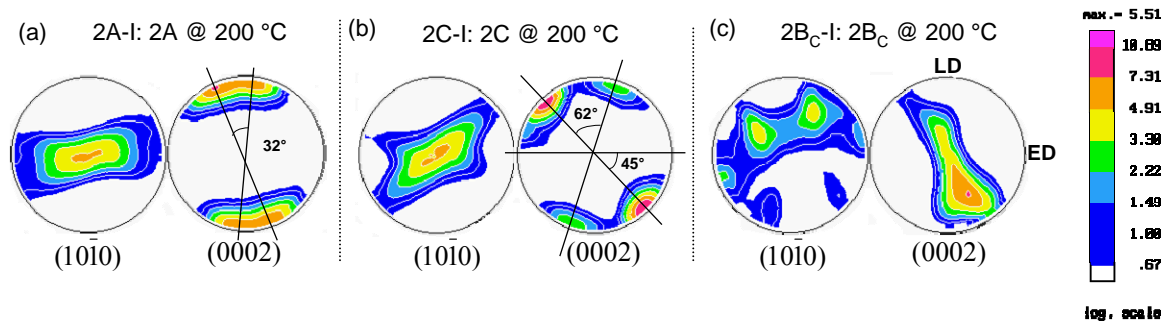


Figure 4.5 Basal and prismatic pole figures for (a) 2A-I (b) 2C-I and (c) 2B_C-I samples. The starting texture of all these cases is similar to the one shown in Figure 6.a. The split between the peaks in the basal pole figures of 2A-I and 2C-I samples is measured as 29° and 65° , respectively.

4.3 Mechanical Flow Response

It is well known that Mg and Mg alloys exhibit plastic anisotropy and tension-compression asymmetry as a result of texture and the strong dependence of deformation mechanisms on crystal orientation. In this section, the effect of texture changes as a result of starting texture, number of ECAE passes, and route on room temperature plastic anisotropy in tension and compression are reported.

As a basis of comparison, the mechanical response of the as-received material was determined. The initial texture of the sample had a strong basal texture. Consequently the flow anisotropy and tension-compression asymmetry in the as-received material is found to be significant. The as-received specimens yielded at 158 and 58 MPa in tension along the in-plane (IP) and through-thickness (TT) directions, respectively. In compression however, the specimens yielded earlier along the IP direction with a 0.2% proof stress value of 69 MPa compared to 126 MPa through the thickness (see Figure 4.6 and Table 4.1).

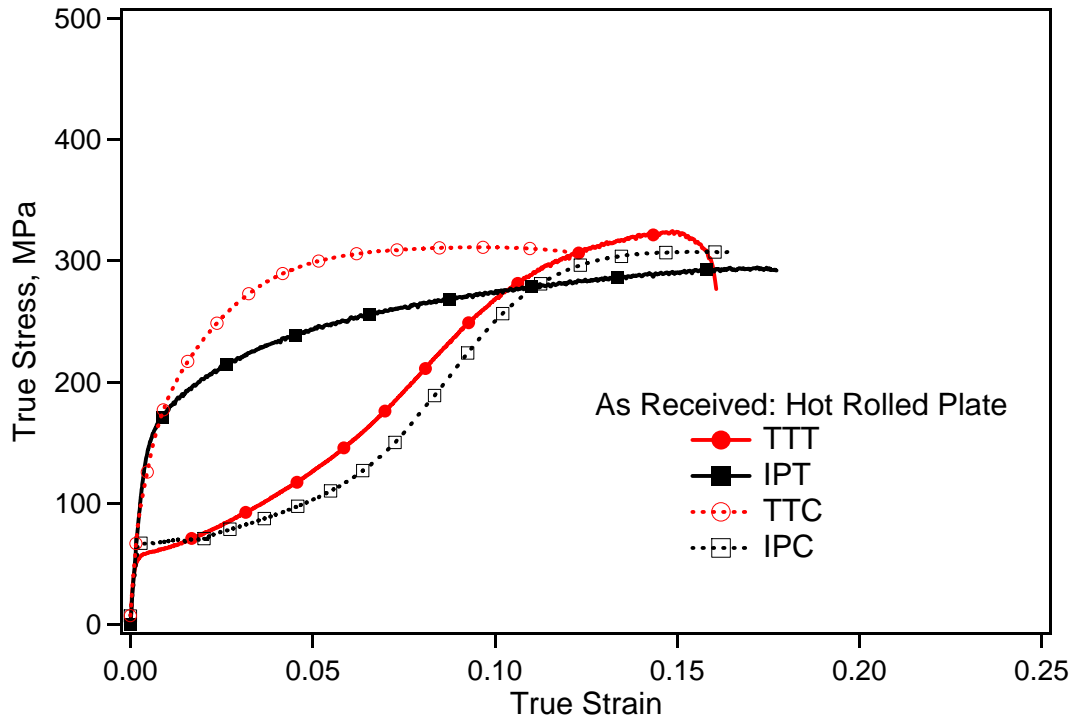


Figure 4.6 Room temperature tensile (solid lines) and compressive (dashed lines) responses of as-received, hot rolled AZ31B alloy along the two plate directions: In-plane (IP) and through-thickness (TT).

Table 4.1 Mechanical properties of ECAE processed AZ31B Mg alloy under tension and compression including the standard deviation. The number before the billet label indicates the number of passes, I represent the starting texture of basal poles parallel to the extrusion direction and II represent the starting texture of basal poles parallel to the flow direction. (IP: In-plane, TT: Through-Thickness, ED: Extrusion Direction, LD: Longitudinal Direction, FD: Flow Direction, SD: Stress Differential).

Billet	Direction	Tension			Compression		SD (%)
		0.2% proof stress (MPa)	UTS (MPa)	ϵ_f	0.2% proof stress (Mpa)	UTS (MPa)	
As Received	IP	158.5 ± 1.5	290 ± 3.0	0.158 ± 0.015	69.0 ± 1.4	307 ± 3.5	-78.7
	TT	58.5 ± 0.5	319 ± 5.0	0.149 ± 0.012	126.0 ± 2.6	295 ± 5.5	73.2
1A-I	ED	143 ± 10	298 ± 11	0.152 ± 0.018	133.5 ± 1.5	336.5 ± 0.5	-6.52
	LD	100 ± 4.1	256.5 ± 0.5	0.112 ± 0.001	119 ± 24	286 ± 21	17.45
	FD	222 ± 1	328.5 ± 1.5	0.191 ± 0.002	147.5 ± 0.5	378.5 ± 0.5	-40.32
1A-II	ED	150.5 ± 0.5	255.5 ± 13.5	0.061 ± 0.016	137 ± 8	269 ± 3	-9.39
	LD	103 ± 0	258 ± 9	0.109 ± 0.012	102.5 ± 1.5	272 ± 2	-0.49
	FD	135.5 ± 2.5	304.5 ± 4.5	0.1315 ± 0.0085	136 ± 5	343.5 ± 0.5	0.37
2A-I	ED	144 ± 2	283 ± 0	0.1055 ± 0.0005	148 ± 9	296 ± 13	2.74
	LD	128 ± 2	238 ± 6	0.092 ± 0.002	135.5 ± 6.5	290 ± 20	5.69
	FD	246 ± 0	321 ± 1	0.158 ± 0.009	182 ± 6	436 ± 7	-29.91
2C-I	ED	82.5 ± 0.5	237.5 ± 7.5	0.151 ± 0.014	114 ± 13	224 ± 4	32.06
	LD	102 ± 2	195 ± 1	0.1115 ± 0.0005	122 ± 3	240 ± 15	17.86
	FD	261 ± 4	347 ± 0	0.162 ± 0.024	193 ± 2	442 ± 2	-29.96
2B _C -I	ED	166 ± 22	291 ± 28	0.119 ± 0.047	181 ± 10	270 ± 0	8.65
	LD	114 ± 2	239 ± 1	0.120 ± 0.006	134 ± 4	290 ± 16	16.13
	FD	147 ± 0	314 ± 8	0.169 ± 0.022	162 ± 2	377 ± 6	9.71

The plastic anisotropic properties of the material changed after ECAE processing. Table 4.1 lists the 0.2% proof stresses, ultimate tensile strength (UTS), and strain-to-failure of all the samples tested. From the table it is readily apparent that the plastic anisotropy and T-C asymmetry in yield strength are significantly lower in the 1A-II sample than 1A-I sample and overall lower in the 2B_C-II sample than the 2A-II and 2C-II samples. For instance, the 0.2% proof stresses of the 1A-I samples along the LD, ED and FD are 100, 143 and 222 MPa in tension and 119, 134 and 148 MPa in compression, respectively. The 0.2% proof stresses of the 1A-II samples along LD, ED and FD are 103, 150 and 135 MPa in tension and 103, 137 and 136 MPa in compression, respectively. In addition to the anisotropy in yield strength, the hardening behavior of the samples when tested along the three orthogonal directions are also notably different. The remainder of this section is dedicated to relating the observed hardening behavior of these responses to the textures generated after ECAE.

The true tensile and compressive stress-strain responses of 1A-I and 1A-II are shown in Figure 4.7. In tension, the 1A-I samples exhibited higher tensile yield strength and subsequently lower work hardening at the later stage of deformation when tested along the FD and ED than those that were tested along the LD. Such directional dependence can be associated with the activation of tensile twinning. Recall in Figure 6 the textures after one-pass ECAE 1A-I, wherein most of the grains in this sample had the basal poles aligned with LD and almost perpendicular to ED and FD. Because tension along LD places most of the grains in c-axis tension, it will be accommodated mostly by tensile $\{10\bar{1}0\}$ twinning [50, 105, 106]. The strain hardening behavior observed along LD

is characteristic of the activation of twins, i.e. a plateau region with a relatively steady flow stress (or low hardening rate) [12, 50, 105-107] followed by an upward curvature with a high hardening rate. This kind of hardening behavior is not seen in the ED or FD tensile responses, two tests which do not place the crystals in c-axis tension and hence would not favor tensile twinning. Instead, the alloy exhibits a typical reduction in strain hardening rate with increasing strain associated with slip-dominated deformation. Incidentally tension along the ED and FD of the 1A-I sample is comparable to in-plane tension of hot rolled plate or sheet, possessing also a strong basal texture, in which basal slip and prismatic slip accommodate most of the deformation [108].

Due to the directionality of twinning, compression testing produces the opposite responses than those resulting from tension testing. As shown in Figure 4.7, the increasing hardening rate associated with twinning is observed when the alloy is compressed along the ED and FD but not along the LD. Since the basal poles are spread close to the LD in the 1A-I texture, it is likely that compression along the LD activated mainly basal and pyramidal $\langle c+a \rangle$ slip. In addition, the samples yield earlier in tension compared to compression when tested along the LD, and the opposite is the case when tested along ED and FD. Apparently, the activation of tensile twins makes the samples yield at a lower stress level, at least for the present ECAE cases.

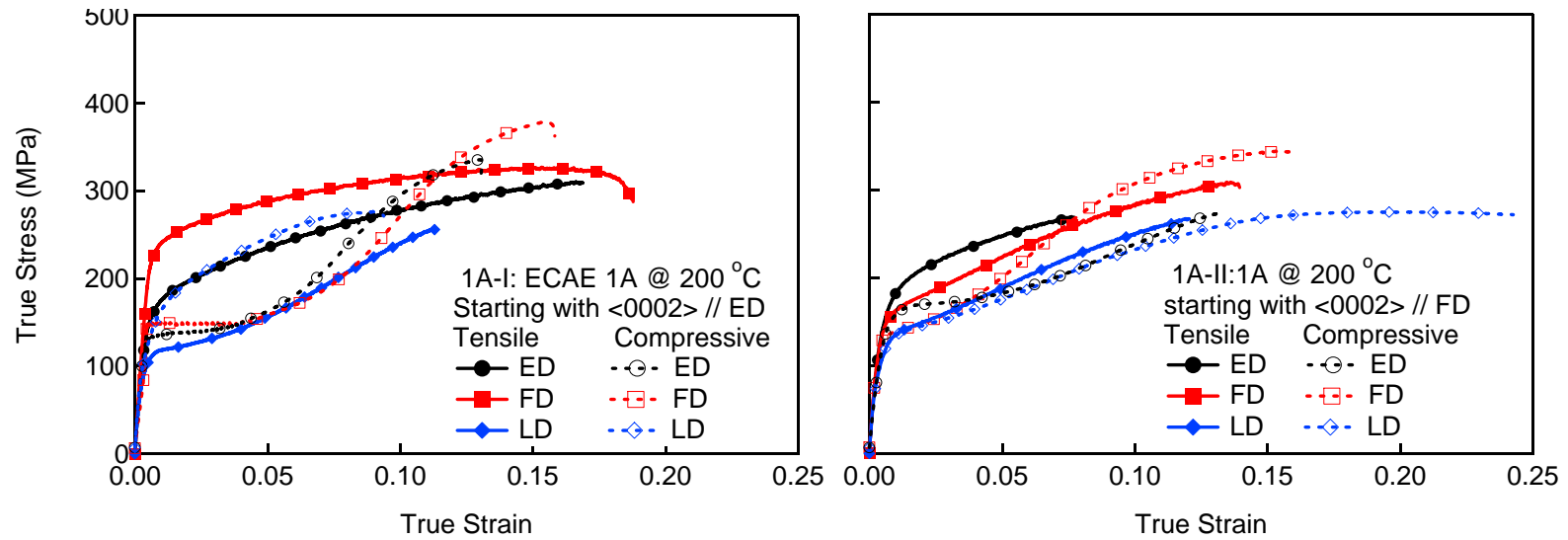


Figure 4.7 Room temperature tension (solid lines) and compression (dashed lines) of AZ31B alloy ECAE processed starting with basal poles parallel to (a) Extrusion direction (1A-I) and (b) Flow direction (1A-II).

As a result of differences in texture development after ECAE between the 1A-I and 1A-II samples, the tensile and compressive responses in the 1A-II sample are different from those of the 1A-I sample. The most obvious and significant observation is that 1A-II processing results in a much lower flow stress anisotropy and tension-compression (T/C) asymmetry than the 1A-I case. For instance, in the case of LD testing, T/C asymmetry is almost negligible. The reduction in directional dependence can be attributed to the more diffuse texture developed in the 1A-II sample than 1A-I sample. This is an important finding because it shows the possibility of controlling flow stress anisotropy and T/C asymmetry through careful selection of starting texture before ECAE while also refining the grain size simultaneously.

The hardening response of the 1A-II samples in all tension and compression tests exhibited an interval of increasing strain hardening rate with strain that signifies deformation twin activity. The only exception is the ED tensile response. Based on the texture of the 1A-II sample (Fig. 4.4.b), it is clear that uni-axial compressive loading in the ED, FD, and LD or tensile loading in the FD and LD of the 1A-II sample places some fraction of the crystals in c-axis tension, promoting $\{10\bar{1}2\}$ twinning. ED tension, on the other hand, places most of the c-axis in compression making it impossible to activate $\{10\bar{1}2\}$ twinning.

The true tensile and compressive responses of the 2A-I, 2C-I and 2B_C-I samples are shown in Figure 4.8 and the mechanical properties extracted from these curves are listed in Table 4.1. Like the first-pass cases, the trends in the flow stress anisotropy and T/C asymmetry in the two-pass cases can be correlated with the texture that develops

after two-pass ECAE. In both the 2A-I and 2C-I sample textures, most of the basal planes normals are perpendicular to the FD testing direction. Consequently the 2A-I and 2C-I samples have almost the same mechanical response along the FD in both tension and compression. In both cases, FD tension is likely accommodated by basal slip and FD compression mainly by tensile twinning. In contrast, due to the difference in basal pole orientations with respect to the ED and LD directions between the 2A and 2C sample textures, their responses along the ED and LD are not the same. For instance since the basal poles in the 2C-I sample make an almost 45° angle with ED, which maximizes the resolved stresses on the basal planes, ED tension in the 2C-I sample should favor more basal slip activity and hence explain the lower flow stress observed in this test than that in the ED tension test of the 2A-I sample. Moreover, because of the similar orientation of basal poles with respect to both the ED and LD directions in the 2C sample, there is little difference between the ED and LD responses whether in tension and compression. Because neither maximum is oriented well for tensile twinning, the T/C asymmetry along the ED and LD is also small. Similar to the 1A-II samples, the 2B_C-I samples demonstrate overall lower flow anisotropy and T/C asymmetry due to the more randomly distributed basal poles in the 2B_C-I texture in comparison to the textures of the 2A-I and 2C-I samples.

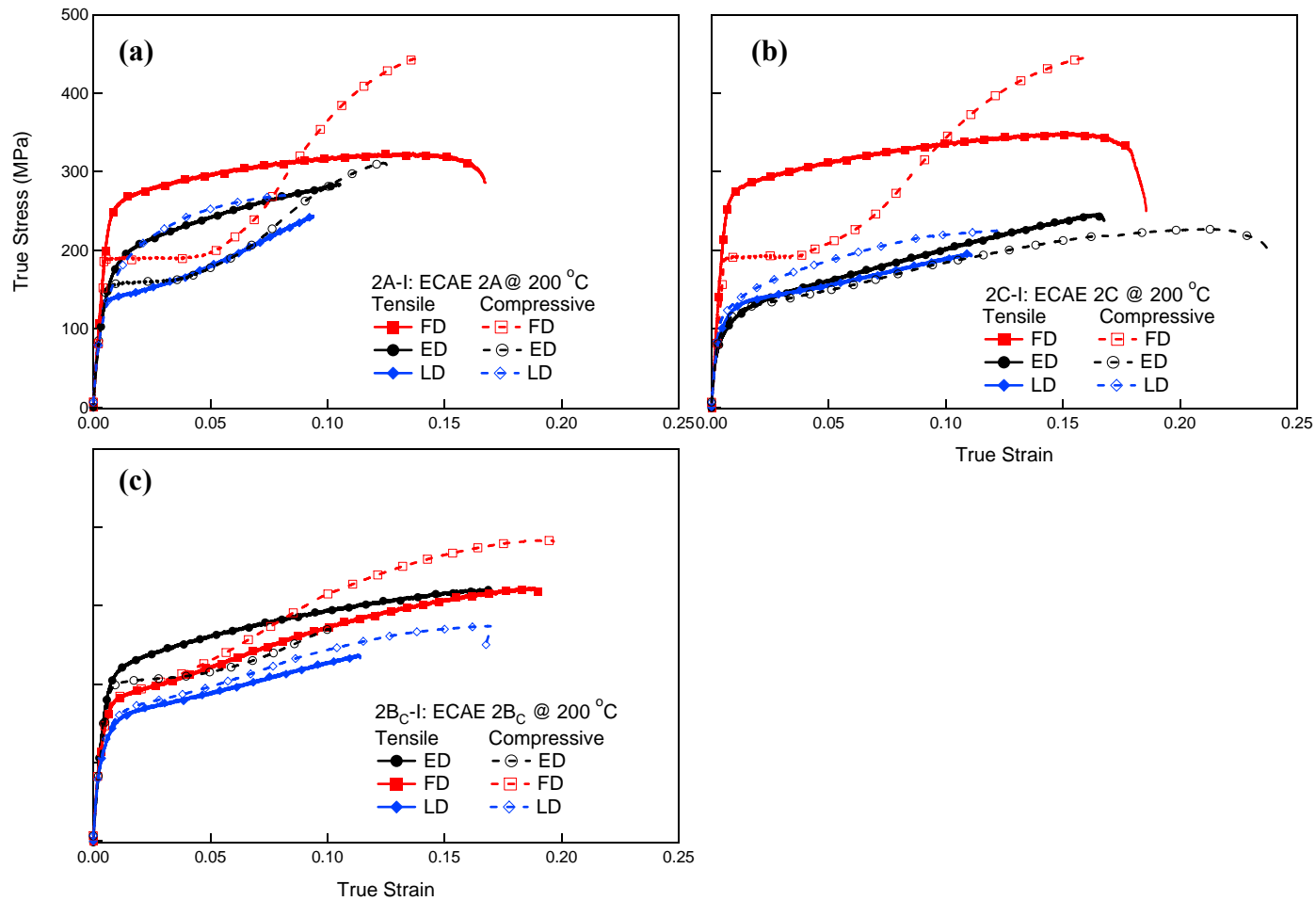


Figure 4.8 Room temperature true tension (solid lines) and compression (dashed lines) of AZ31B ECAE samples processed up to two passes following route (a) A (2A-I), (b) C (2C-I), and (c) BC (2BC-I).

4.4 Discussion of Results

The microstructure and crystallographic texture of ECAE processed samples are found to be highly dependent on the initial grain orientation with respect to the die geometry. The microstructure of the 1A-I and 1A-II samples, for example, are completely different in terms of the grain morphology and the amount of DRX. This should be because of the different deformation modes active during these two ECAE cases. In order to correlate the microstructural evolution with the governing deformation mechanisms, the ECAE process was simulated using a visco-plastic self-consistent (VPSC) crystal plasticity model. The VPSC model can predict theoretically the activity of several different deformation modes to achieve a particular deformation texture.

4.4.1 Texture prediction

Texture evolution, grain morphology, and DRX during ECAE processing were shown to depend significantly on the starting texture, number of passes (one or two), and route (A, B_C, or C). The observed differences in these microstructural properties are related to the relative activities of the various slip modes activated during each deformation path. To determine the variation in slip during each ECAE test the ECAE simulation model in [24-26], which incorporates the visco-plastic self-consistent (VPSC) crystal plasticity scheme, was applied. In these prior works the model formulation, extensions to severe plastic strain deformation, the applied ECAE shearing, and treatment of the rigid body rotations between ECAE passes are described.

The same material model is used to simulate ECAE continuously up to two passes for a given starting texture and ECAE route and to predict the evolution of four slip modes, texture, and grain morphology without adjustment of any parameters. The simulation begins by importing the starting texture in one of two orientations I or II as shown in Figure. 3.1. The initial texture is represented by 1000 discrete orientations and the grains are initially spherical. The CRSS values to activate each slip mode are constant and are normalized by the CRSS value for basal slip. They are assigned values of 1.0, 6.0, 8.0 and 8.0 for basal $\langle a \rangle$, pyramidal $\langle c+a \rangle$, pyramidal $\langle a \rangle$ and prismatic slip $\langle a \rangle$, respectively, which are the same as those first reported in Agnew et al. [59]. It should be mentioned that although this set of CRSS values may work for AZ31, even up to four passes [104], a significantly different set has been characterized for another Mg alloy (ZK60) at different grain sizes [102].

Figures 4.9 and 4.10 show respectively the first-pass and second-pass basal pole figures predicted from the model. In all cases the agreement is excellent, which indicates that the relative activities of basal, pyramidal $\langle a \rangle$ and $\langle c+a \rangle$, and prismatic slip are on average over the entire material are well predicted. In the 1A-I case, the calculated texture has the 38° angle between the two basal peaks as well as the correct location of the two peaks. Also, the predicted 27° orientation of the basal peak from LD in the 1A-II basal pole figure is in good agreement with the experimental one. Likewise the variation of the angles between the two maxima in basal pole figures of 2A-I and 2C-I was successfully predicted. Moreover, in case of 2B_C-I, the predicted location of the

basal pole peaks with respect to the billet directions agrees well with the experimental results.

It is important to note that despite the assumptions of homogeneous effective medium (HEM) in the self-consistent approach, the agreement between the predicted and measured texture is good. This could be attributed to the fact that the AZ31B Mg alloy at such high processing temperature of 200 °C is very dilute. Moreover, the strong texture observed in as received and processed samples reduces the inhomogeneity of the matrix. Therefore, an HEM can be assumed in which each grain see the same strain rate tensor and interact with the same representative medium.

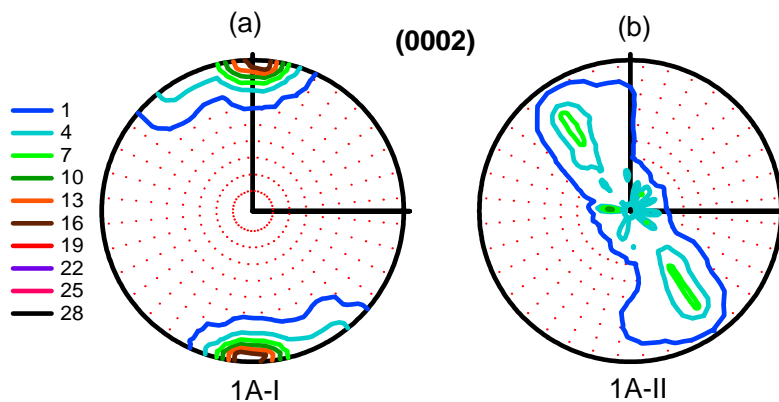


Figure 4.9 Predicted basal pole figures of AZ31B Mg alloy processed via one ECAE pass starting with basal poles parallel to (a) the extrusion direction (1A-I), and (b) parallel to the flow direction (1A-II).

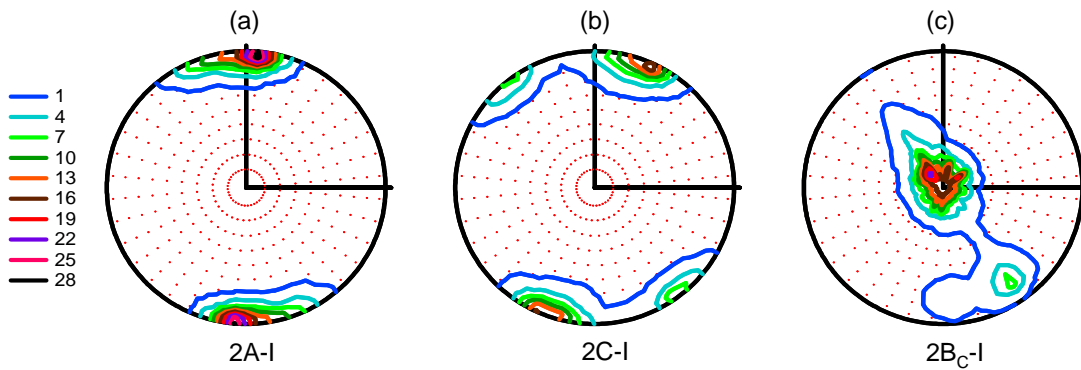


Figure 4.10 Predicted basal pole figures of AZ31B Mg alloy processed via two ECAE passes starting with basal poles parallel to the extrusion direction and following route (a) A (2A-I), (b) C (2C-I) and (c) B_C (2B_C-I).

It is important to note that twinning and DRX were not included in the model and in spite of their absence, the model is effective in forecasting texture evolution up to two passes. This may indicate that twinning did not occur or was negligible in contribution and as support, has not been reported to take place during processing at 200 °C [59]. Effective texture predictions without accounting for DRX have been also reported earlier [102, 104].

It should be emphasized that while constant CRSS values may be suitable for texture prediction, they generally are not for predicting the evolution of the material response during ECAE and subsequent stress-strain response of the processed billets. Plastic anisotropy is more sensitive than texture to details of microstructural evolution (e.g., amount of DRX, grain size, dislocation density accumulation, substructure development). Modeling the mechanical flow response of ECAE material in this case

would require evolving the CRSS for each slip system according to thermally activated storage of dislocations, as was done in [26, 50, 91]. Accounting in particular for the temperature dependence in hardening response is critical since processing took place at a significantly different temperature (200 °C) than subsequent testing (room temperature). The present model, however, is sufficient to accurately predict texture evolution during ECAE as a function of starting texture and ECAE route, and should be beneficial for simulation-based selection of thermo-mechanical processing parameters to obtain a desired texture. Since texture is the main determining factor for the plastic anisotropy in Mg alloys as clearly shown in Section 4.3, starting texture and ECAE parameters can be selected carefully with the help of the present model to reach highly anisotropic or weakly anisotropic end material.

4.4.2 Deformation mechanisms during ECAE

Effective texture predictions can provide insight on the relative contributions of slip as a function of deformation path. Figures 4.11 and 4.12 show the relative activities of the aforementioned slip modes for the one-pass and two-pass ECAE cases, respectively. In all cases, basal slip was the most active and pyramidal $\langle a \rangle$ slip was negligible or inactive. However, each test differed substantially in the amount of non-basal slip activity of pyramidal $\langle c+a \rangle$ slip and prismatic slip. During both 1A-I and 1A-II, most of deformation is accommodated only by basal slip. However unlike 1A-I, during 1A-II, pyramidal $\langle c+a \rangle$ and prismatic slip were also active (Figure 4.12.b). In the second passes of the 2A-I and 2C-I extrusions, most of the deformation is accommodated by basal slip and secondly by pyramidal $\langle c+a \rangle$ slip. The difference in

the location of their maxima may be explained by the deformation stage at which $\langle c+a \rangle$ slip is active. As shown in Figure 4.12.a, during 2A-I, $\langle c+a \rangle$ slip was active in the first 20% and last 40% of the strain but during 2C-I, it was only active in the first 50% of the strain. It is possible that activity of pyramidal $\langle c+a \rangle$ slip in the last stage of ECAE deformation brought the two basal peaks closer together in the 2A-I texture. In the second pass of the 2B_C-I extrusion we find the most prismatic slip activity.

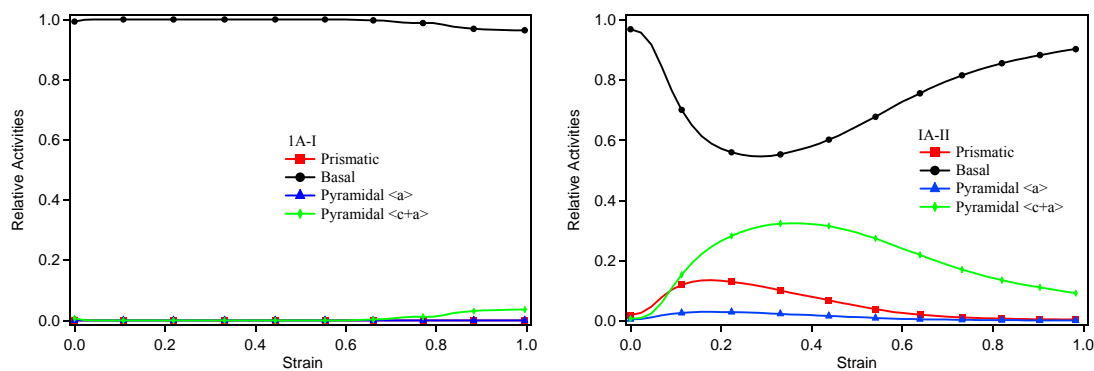


Figure 4.11 Predicted relative activities of the considered deformation modes for one ECAE pass starting with basal poles parallel to (a) the extrusion direction (1A-I), and (b) parallel to the flow direction (1A-II).

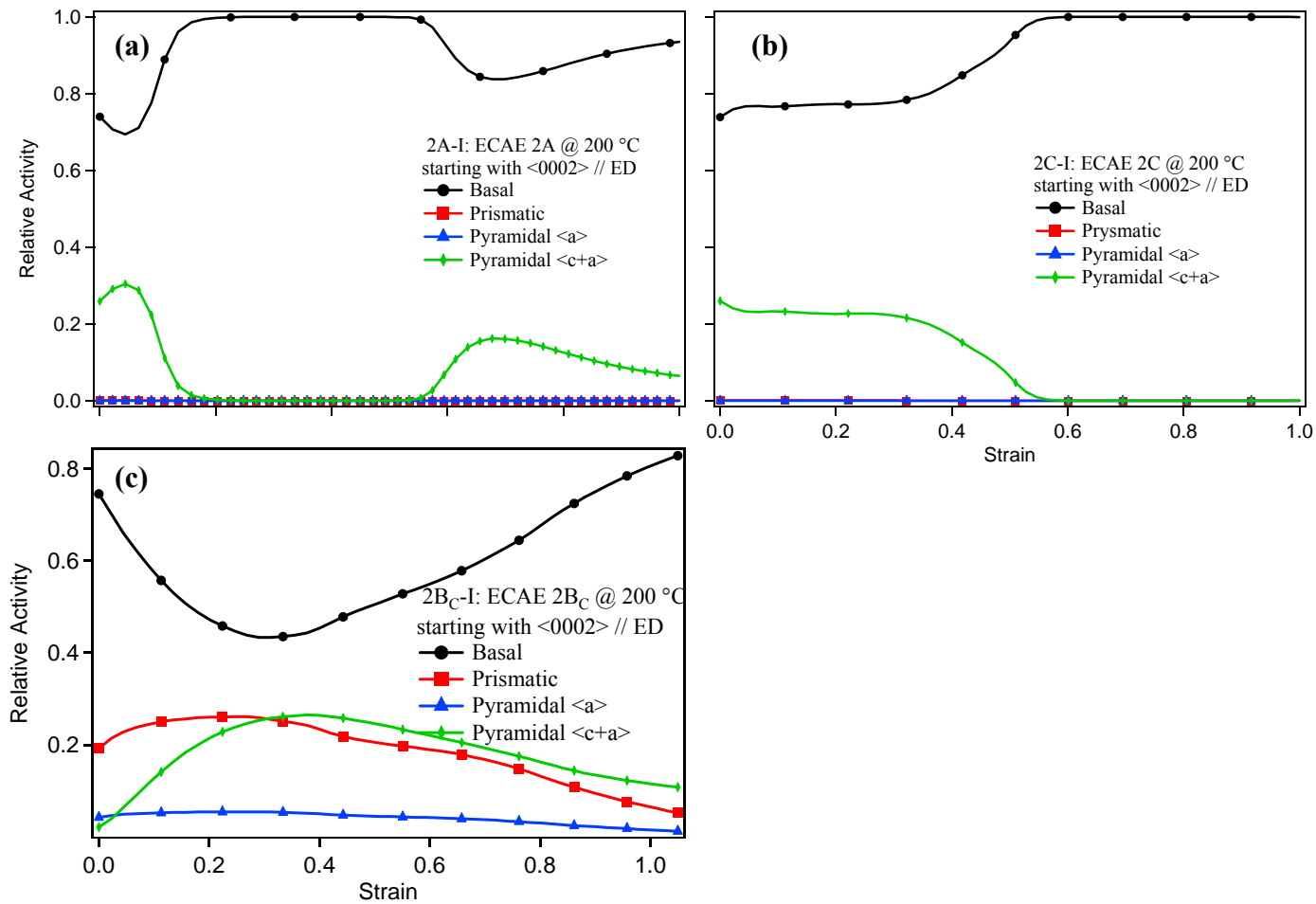


Figure 4.12 Predicted relative activities of slip systems during the second ECAE pass starting with basal poles parallel to the extrusion direction, and following route (a) A (2A-I), (b) C (2C-I) and (c) B_C (2B_C-I).

The slip modes activated can be explained by the orientation of the entry texture with respect to ECAE shearing. The starting orientation of case I places the crystals in a favorable orientation for basal slip with respect to the ECAE shearing and consequently in the 1A-I extrusion, almost all plastic deformation is accommodated by the basal slip. The starting orientation of case II, however, orients most of the crystals well for prismatic slip. As this is a relatively hard mode, deformation in 1A-II triggers the activity of basal, pyramidal $\langle c+a \rangle$ and prismatic slip. The entry texture for the second passes depends on the texture developed after the first pass, in this case 1A-I. The 1A-I had two maxima. No rotation and the 180° rotation around the axis of the billet before the second ECAE pass in route A and C, respectively, align the concentration of basal poles of one peak parallel to the ED similar to the case I starting texture. The other peak is placed at an angle of 33° counterclockwise and clockwise about LD in route A and C, respectively. These crystals are oriented well for pyramidal $\langle c+a \rangle$ slip in both cases, but due to the difference in the location of their second peak with respect to ECAE shearing, the evolution of pyramidal $\langle c+a \rangle$ slip in 2A and 2C is not the same. Before the second ECAE pass, the rotation of the billet by 90° around its ED in route B_C aligns the basal poles parallel to FD similar to the starting texture before the 1A-I extrusion but with a secondary peak making an angle of about 30° from the FD. As in the 1A-II extrusion, this ‘hard’ orientation activates all three slip systems but due to some distribution of orientations $\sim 20\text{-}30^\circ$ from the FD more prismatic slip is promoted.

4.4.3 Effect of prismatic slip on dynamic recrystallization during ECAE

It is well known that DRX occurs most readily in materials in which recovery is slow, e.g. in materials of medium or low stacking fault energy (SFE). The SFEs in magnesium depend on the slip plane: about 32-36 mJ/m² for the basal plane [64, 65], 265 mJ/m² for the prismatic plane [64] and 344 mJ/m² for the pyramidal plane [64]. Therefore recovery by DRX can be associated with deformations involving basal slip while recovery by dynamic recovery (and lack of DRX) can be associated with active prismatic and pyramidal slip. Alternatively Ion et al. [66] ascribed DRX during high temperature deformation of Mg to the constraints imposed by the lack of easily activated slip systems rather than the effect of SFE.

Of the two non-basal slip systems important in Mg deformation, it is probable that the activity of prismatic slip, more so than pyramidal $\langle c+a \rangle$ slip, moderates the amount of DRX. Barnett [109] found that the amount and progress of DRX was sensitive to changes in crystal orientation in relation to the compression axis of the deformed Mg alloy. In that study, the lowest recrystallized volume fraction occurred when prismatic slip was the most prevalent. It has also been reported that prismatic slip tends to relax the structure [49] and therefore, activity of prismatic slip could act as a relaxation mechanism, which lowers the amount of internal stress and hence the available energy for DRX.

The present results suggest prismatic slip during ECAE influenced the amount of DRX during ECAE of Mg. In the 1A-II and 2B_C-I cases, where prismatic slip is favored and active throughout the extrusion, a lower volume fraction of DRX is observed,

supporting the findings of Barnett [109]. Most of the DRX seen in the 2B_C-I sample probably took place during the first ECAE pass 1A-I, which deformed primarily by basal slip.

4.4.4 Effect of prismatic slip on evolution of grain morphology

Grain morphologies can also be extracted from the simulations. The ellipsoidal grain shape is predicted to evolve according to the slip activity, crystal orientation, strain level, interactions with surrounding anisotropic, homogeneous medium, and strain path experienced by each individual grain. The distribution of the ratio of the major axes (a) to the minor axis (b), a/b , of the deformed ellipsoid for all 1000 grains used in the simulation are plotted in Figures 4.13 and 4.14. Figure 4.13 compares the predicted distribution of the ratio a/b between the two first-pass cases, and Figure 4.14 compares the calculated a/b distribution between the three routes after the second ECAE pass. Also shown in these figures are the experimental averages of the a/b ratio obtained by measuring about 100 grains from each sample. In good agreement with the measurement, the model predicts higher grain elongations in the 1A-II case than the 1A-I case. Also consistent with the measurements, the model predicts that grains in the 2B_C-I sample are more elongated than the grains in both the 2A-I and 2C-I samples. Although the average a/b ratio of the 2A-I and 2C-I samples is the same, the latter distribution is bi-modal, as can be seen in Figure 4.14.b. The a/b ratio distribution for the 2B_C-I sample is also bi-modal (Figure 4.14.c). The higher variability in the grain shape calculated for the 2C-I and 2B_C-I samples than for the 2A-I samples can be validated by the lower magnification optical micrographs shown in Figure 4.15. The microstructure of the 2A-I

sample as seen in Figure 15.a is more uniform than that of the 2C-I and 2B_C-I samples in Figure. 4.15.b and 4.15.c, respectively. Evidently the latter two deformed samples have a wider range of grain shapes, in agreement with the prediction.

Qualitatively good agreement in grain shape evolution between the model and measurement suggests that the activity of prismatic slip tends to elongate the grains. Unlike 1A-I, 2A-I, and 2C1, simulations of 1A-II and 2B_C-I processing predict pronounced prismatic slip activity throughout the deformation. The grains in the 1A-II and 2B_C-I possess a similar, highly variable shape (a/b) distribution and are more elongated than those in 1A-I, 2A-I, and 2C-I.

4.5. Flow Stress Anisotropy and Tension-compression Asymmetry

Tension-compression asymmetry in yield strength can be quantified by the following stress differential (SD) [110] which is given by

$$SD = \frac{(\sigma_y^c - \sigma_y^t)}{0.5 \times (\sigma_y^c + \sigma_y^t)} \quad (4.1)$$

where σ_y^t and σ_y^c are yield strengths in tension and compression. The SD ratio for all cases are listed in Table 4.1 and plotted as functions of number of passes in Figure 4.16. As shown T/C asymmetry was reduced from the as-received to the processed material. For a given direction, the SD ratios are generally higher for the 1A-I, 2A-I, and 2C-I samples than 1A-II and 2B_C-I samples.

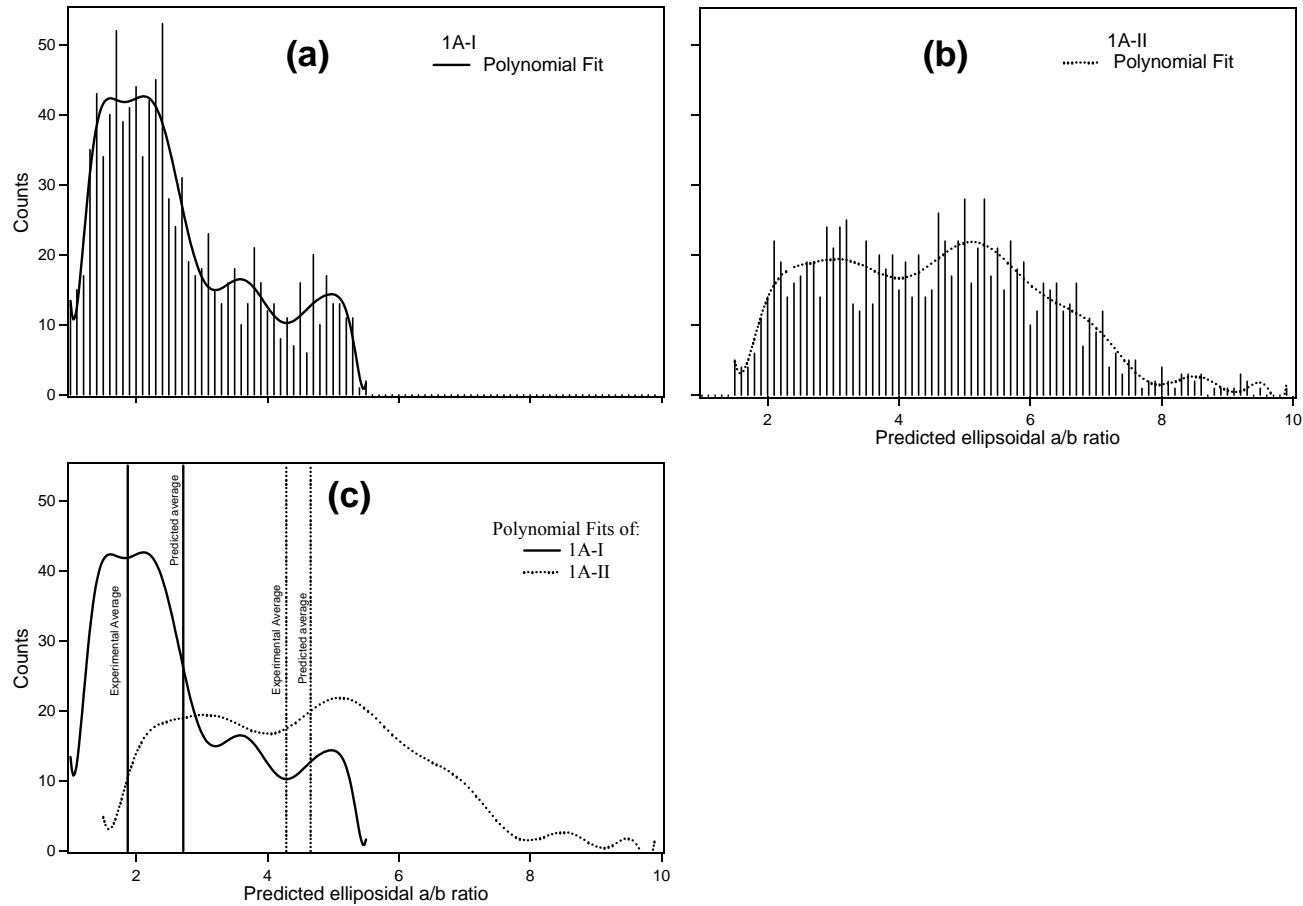


Figure 4.13 The predicted distribution of grain ellipsoidal ratio (grain major to minor axes ratio (a/b)) for the two one-pass ECAE cases: (a) starting with basal poles parallel to extrusion direction (1A-I) and (b) starting with basal poles parallel to flow direction (1A-II). The polynomial fits and the experimental and predicted average (a/b) ratio of the two cases.

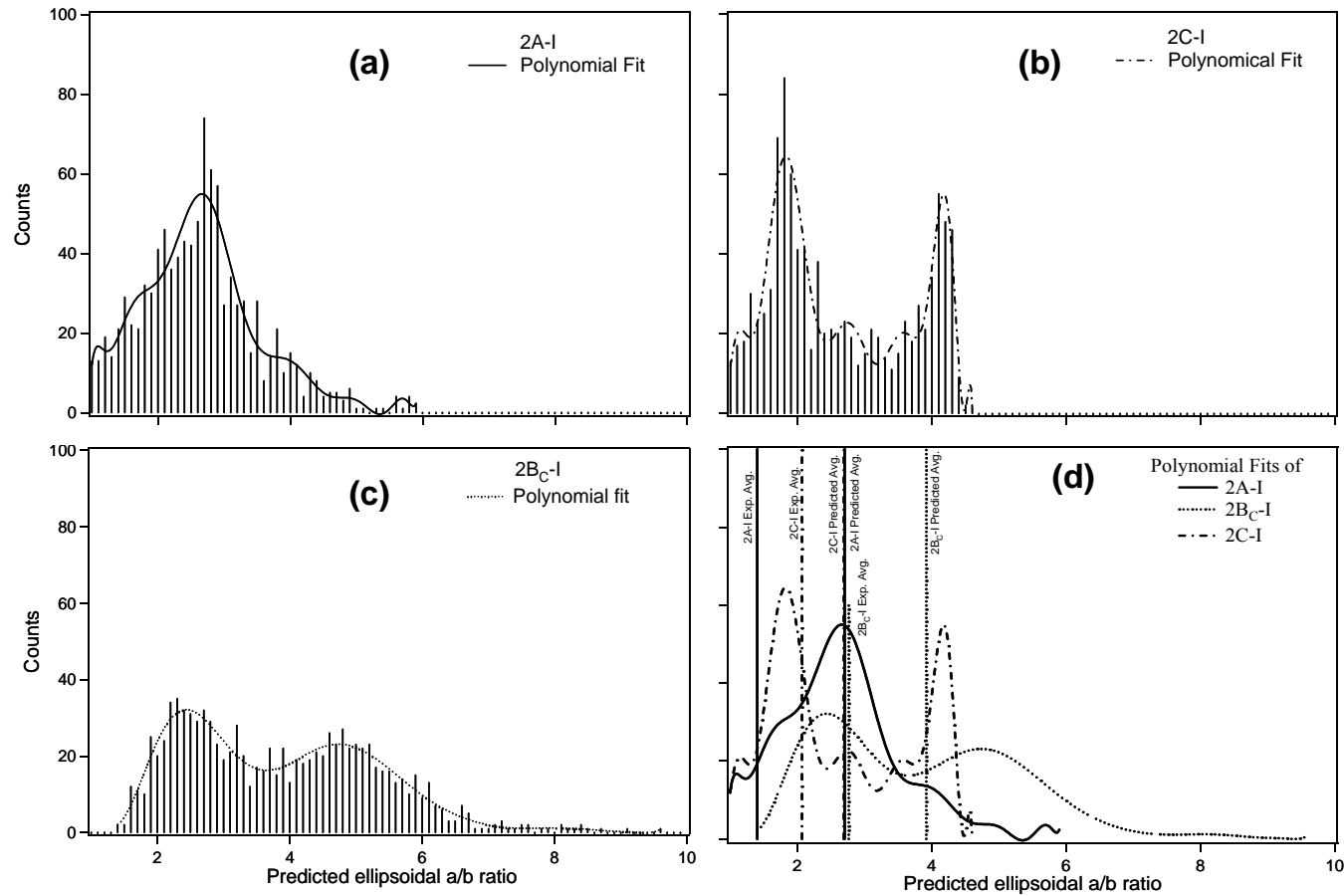


Figure 4.14 Predicted distribution of ellipsoidal grain major to minor axes ratio (a/b) for the three two-pass ECAE cases starting with basal poles parallel to extrusion direction and following route (a) A (2A-I), (b) C (2C-I) and (c) B_C (2B_C-I).. (d) The polynomial fits, and, the experimental and predicted average of (a/b) ratio of the three two-pass ECAE cases.

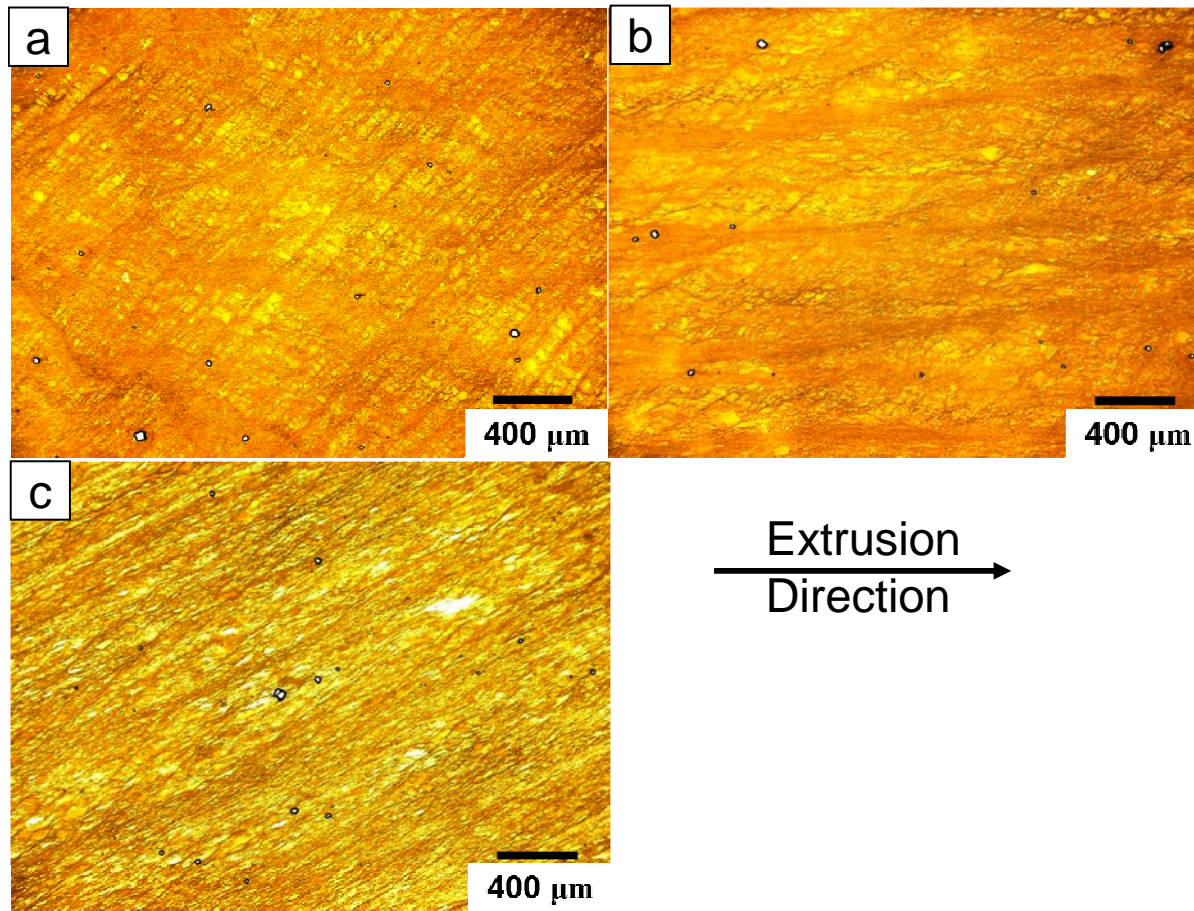


Figure 4.15 Lower magnification optical micrographs of AZ31B ECAE samples processed starting with basal poles parallel to the extrusion direction and up to two ECAE passes following route (a) A (2A-I), (b) C (2C-I) and (c) B_C (2B_C-I) . The extrusion direction is to the right.

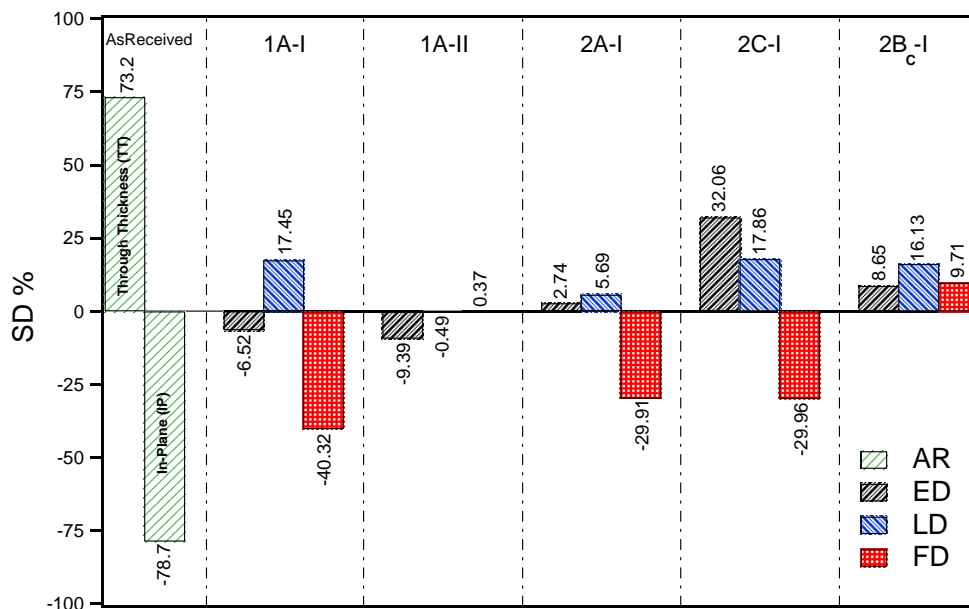


Figure 4.16 Evolution of stress differential (SD) ratio with number of ECAE passes of the as received (AR) sample and the samples of two-passes ECAE following the three routes: A, C and B_c, along the three orthogonal directions of the billets: extrusion direction (ED), longitudinal direction (LD) and flow direction (FD).

Likewise beyond yield, the stress-strain behaviors of the 1A-I, 2A-I and 2C-I samples exhibited higher flow stress anisotropy and tension-compression asymmetry along the three orthogonal directions than the 1A-II and 2B_c-I samples. A notable exception was the ED and LD responses of the 2C-I sample; while the T/C asymmetry in ED and LD yield strengths were high (Figure 4.16), the T/C asymmetry in flow stress was low.

Note that in some load directions, the yield strength and ultimate tensile strength (UTS) of the second-pass material are stronger, while in others they are weaker than the

first-pass material. Therefore, although ECAE does not necessarily strengthen the material uniformly, it can be used to either enhance or reduce plastic anisotropy.

As discussed in section 4.3, the different characteristics in flow stress anisotropy and tension-compression asymmetry in the processed Mg alloys can be explained by considering the textures that develop as a result of the starting texture and the straining path imposed when going from one pass to another during ECAE process and from ECAE shearing to uniaxial testing. The strong orientation dependence with respect to the sense and direction of loading can be attributed to the ease of $\{10\bar{1}2\}$ twinning and the high ratio of CRSS between the slip modes in Mg alloys. Assuming a CRSS criterion for slip and twinning, the CRSS values were characterized via single crystal model of pure Mg tested in various orientations [50]. The two easiest modes were tensile twinning (1 MPa) and basal slip (4 MPa) in comparison with for prismatic (12.5 MPa) and pyramidal $\langle c+a \rangle$ slip (63.2 MPa). The relative ease and directionality of twinning causes the stress-strain response to be highly sensitive to orientation of the c-axis with respect to tensile stress states generated under the applied loading. The relative ease of basal slip leads to flow responses highly dependent on the orientation of shearing with respect to the orientation of the basal slip planes. In the crystallographic textures of 1A-I, 2A-I and 2C-I, the orientation of the basal poles with respect to the FD is similar. Therefore, the stress-strain responses of these three cases along FD in tension and compression are identical, except that the 1A-I sample yields at slightly lower stress level than those of 2A-I and 2C-I which might be due to differences in the grain size and the volume fraction of DRX grains between one and two pass cases. However, the orientation

distribution of the basal poles with respect to ED and FD in the 2C-I sample is more diffuse than those in the 1A-I and 2A-I in samples and therefore the flow anisotropy and tension-compression asymmetry between the ED and FD tests are lower in the former. Compared to these three cases, the basal poles in the 1A-II and 2B_C-I samples are distributed more randomly and hence the flow stress anisotropy is lower.

4.6 Summary of Observations

A systematic study on an AZ31B Mg alloy was conducted to achieve a basic understanding of the relationship between slip activity and the evolution of texture and grain microstructure during ECAE through the studies of only the two passes. Changes in slip activity during the first pass were invoked by changing the orientation of the basal poles of the strong initial texture with respect to the die. The slip activity during the second pass was altered by applying different routes. AZ31B alloy was successfully ECAE processed starting with two different initial grain orientations with respect to the die geometry and up to two passes following routes A, C and B_C. The texture evolution during ECAE was successfully predicted using a VPSC crystal plasticity model in order to understand the relationship between the initial grain orientation and the ECAE texture evolution. The room temperature mechanical responses of the processed samples revealed the significance of the crystallographic texture on flow stress anisotropy and tension-compression asymmetry. The main findings of this study can be summarized as follow:

1. Basal slip was the most active slip mode and pyramidal $\langle a \rangle$ slip was negligible in all ECAE cases.

2. The initial grain orientation (initial texture) with respect to the die orientation significantly affects the evolution of texture, dynamic recrystallization, and grain morphology during ECAE due to different amounts of non-basal slip activity.
3. The activity of prismatic slip during ECAE significantly reduces the amount of dynamic recrystallization because the prismatic slip activity acts as a relaxation mechanism that reduces the stored energy and hence, the likelihood of DRX.
4. A secondary basal peak and its location in the basal pole figure can significantly influence the slip activities during ECAE, and hence, the evolving texture. This can be seen clearly in the 2A-I and 2C-I cases.
5. Flow stress anisotropy and tension-compression asymmetry in the three orthogonal direction of the billets is significantly influenced by the starting texture and route. The difference can be explained based on the concentration and orientation of the basal poles in the post-ECAE texture with respect to testing direction and sense of loading. It is shown that the more random the distribution of the basal poles, the lower the flow anisotropy and tension-compression asymmetry.

CHAPTER V

EFFECTS OF CRYSTALLOGRAPHIC TEXTURE OF AZ31B MG ALLOY ON FLOW STRESS ANISOTROPY AND TENSION-COMPRESSION ASYMMETRY

As a continuation of the study of flow stress anisotropy and tension-compression asymmetry (T/C) discussed in Chapter IV, the pure influence of the crystallographic textures on the anisotropy and asymmetry of the hexagonal closed packed AZ31B Mg alloy will be discussed in this chapter. In order to eliminate the possible effects of grain size and morphology on the anisotropy and asymmetry, the alloy is ECAE processed up to four passes following four different routes. The resulted microstructures of processed samples are much more uniform than those discussed in the previous chapter. The grains in all four samples are equiaxed. All four samples have uniform microstructures with a grain size in the order of 3-5 μm . The textures of the processed samples were also predicted using the aforementioned visco-plastic self-consistent (VPSC) crystal plasticity model for further evaluation of its capabilities in ECAE texture prediction. A comparison between the flow behavior of these uniformly structured samples and those presented in the previous chapter is also conducted in order to isolate the influence of grain size and morphology, if any, in this behavior.

5.1 Microstructures

Figure 5.1 shows the optical micrographs of the four samples discussed in this chapter which were processed up to four ECAE passes following routes A, C, E and B_C. Figure 5.2 shows the grain size distribution of these samples. To be consistent with the same terminology used for one and two-pass sample, the four-pass samples will be labeled as 4A-I, 4C-I, 4E-I and 4B_C-I. The grain size distributions were calculated by measuring the size of about 300 – 400 grains from different micrographs individually, covering most of well defined grains. It is very clear, from micrographs and grain size distributions, that route B_C produces the most uniform microstructure with the smallest grain size of about 2.7 μm. Samples processed following routes A and C have close grain sizes but 4C-I sample is slightly more inhomogeneous as can be seen clearly from the broader grain size distribution (Figure 5.2.b) as well as from its optical micrographs (Figure 5.1.b). The as-received sample (hot rolled plate) has a grain size of about 25 μm as can be seen from Figure 4.1. After four ECAE passes at 200 °C, a grain size in the order of 4 μm was achieved. This refinement could be because of the continuous shearing of the grains as expected during ECAE and because of dynamic recrystallization which has been observed very clearly during one and two ECAE passes of the same material and processing temperature and starting with the same texture.

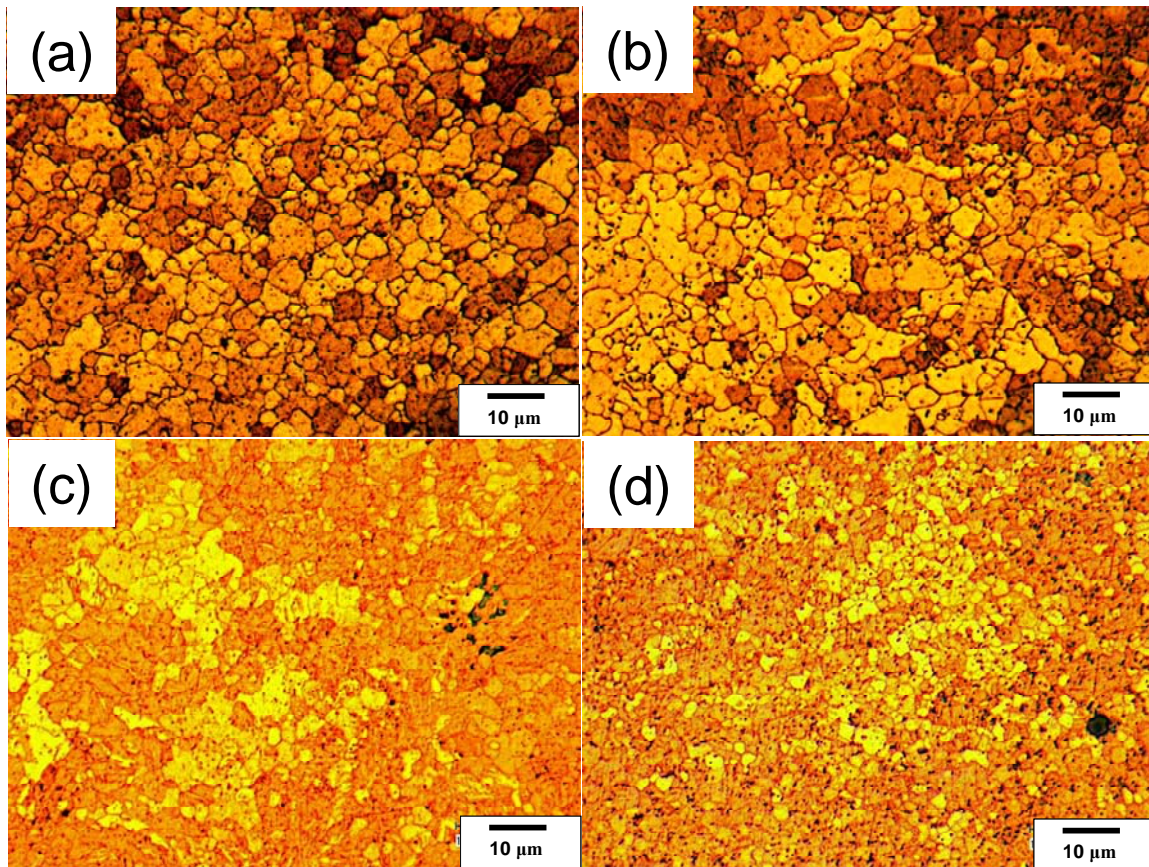


Figure 5.1 Optical micrographs of AZ31B ECAE samples processed up to four ECAE passes and following routes (a) A (4A-I), (b) C (4C-I), (c) E (4E-I) and (d) B_c (4B_c-I).

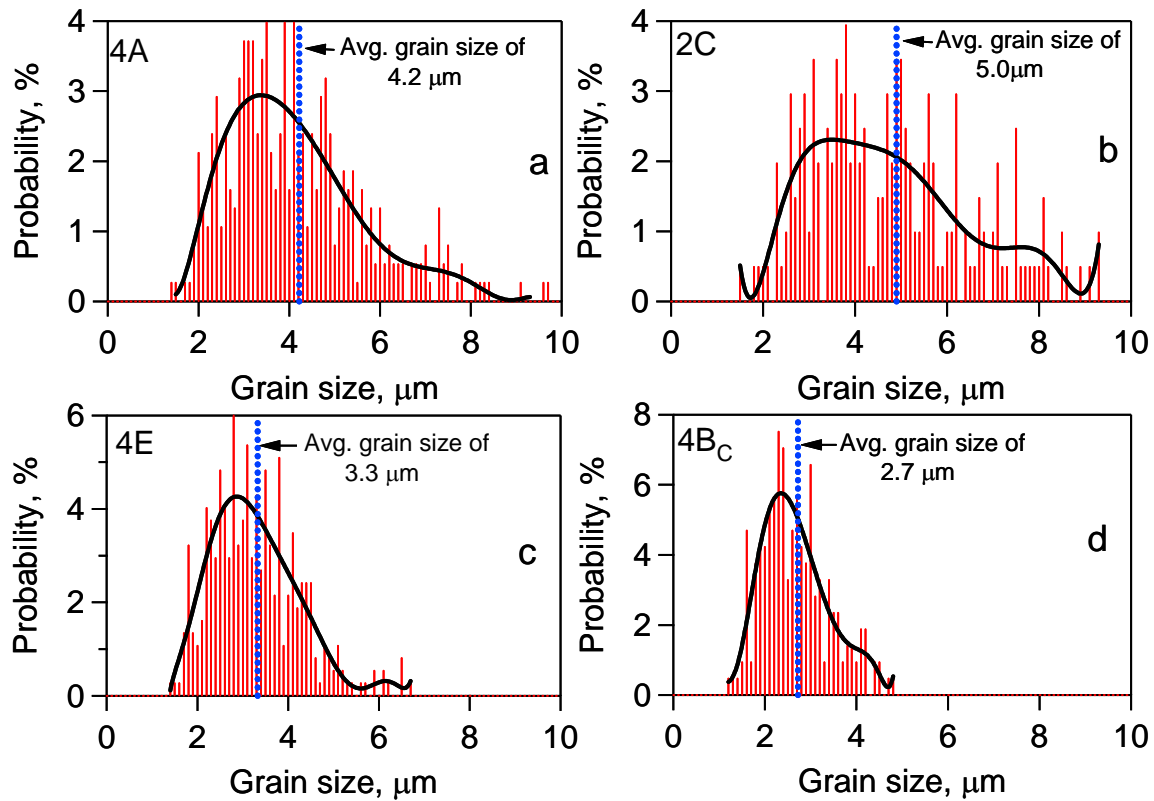


Figure 5.2 Grain size distribution of AZ31B ECAE samples processed up to four ECAE passes and following routes (a) A (4A-I), (b) C (4C-I), (c) E (4E-I) and (d) B_C (4B_C-I).

5.2 Crystallographic Texture Evolution and Prediction

Starting from the same initial texture in which basal poles were parallel to the extrusion directions, the four routes yielded four different textures after 4 passes. The experimental basal pole figures as well as the VPSC predicted ones of 4A-I, 4C-I, 4E-I and 4B_C-I samples are shown in Figure 5.3. Similar to the texture of 1A-I and 2A-I samples shown in Chapter IV, the 4A-I basal pole figure has two basal peaks that are oriented along and about $30\text{-}40^\circ$ from LD. The angle between the two peaks is about 30-

35°. In 4C-I sample the split of the two basal peaks increases to 60-64° compared to the split in 2C-I sample.

In order to further evaluate the visco-plastic self-consistent (VPSC) crystal plasticity model, it has also been used to predict the texture evolution up to four ECAE passes following the four different routes. The simulation was started from the same initial discrete texture of the experimental one in which basal poles are parallel to the extrusion axis during ECAE (Figure 3.2.a). The simulation was continuous, i.e. the starting texture of each pass is the predicted texture of the previous pass. For these predictions, the same parameters used to predict the first and second ECAE texture where only possible slip modes at 200 °C have been considered in the simulation without twinning, and relative critical resolved shear stresses (CRSS) values of 1.0, 6.0, 8.0 and 8.0 for basal $\langle a \rangle$, pyramidal $\langle c+a \rangle$, pyramidal $\langle a \rangle$ and prismatic slip, respectively, have been used. Interestingly, despite the dynamic recrystallization (DRX) that takes place during 200° ECAE and the fact that DRX was not taken into account in the VPSC simulation, the agreement between the predicted and experimental texture is acceptable for all routes as can be seen from Figure 5.3 The DRX grains in Mg alloys, usually, keep the same orientation of the parent grains [111]. This might explain the good agreement between the experimental and predicted textures in the presence of DRX.

5.3 Mechanical Response

The responses of the four ECAE samples: 4A-I, 4C-I, 4E-I and 4B_C-I in tension and compression are shown in Figure 5.4. The first observation from these curves is the

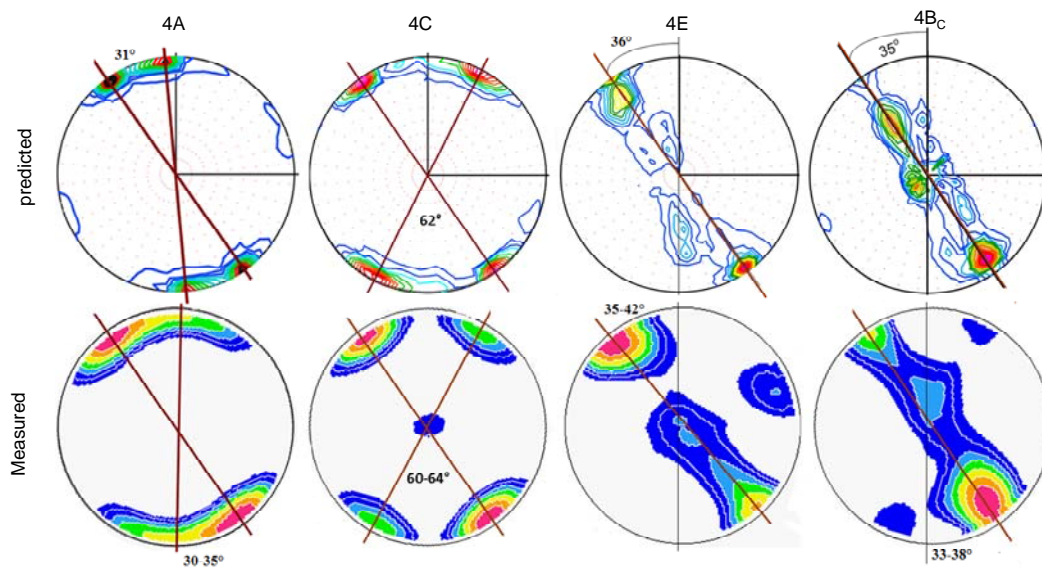


Figure 5.3 Predicted and measured basal pole figures of AZ31B Mg alloy processed via four ECAE passes starting with basal poles parallel to extrusion directions and following route (a) A (4A-I), (b) C (4C-I), (c) E (4E-I) and (d) B_C (4B_C-I).

similar behavior of 4C-I, 4E-I and 4B_C-I samples along both ED and LD in tension and compression. These three samples yield at almost the same stress and strain harden in the same way when tested along ED and LD. The same thing can be said about the hardening behavior along FD of these three samples; however, the yield stress of 4C-I sample in tension is higher than that of 4E-I and 4B_C-I samples. In compression, the four samples yield almost at the same stress value of about 150 MPa when tested along FD. Along this direction (FD), the four samples exhibited lower compressive yield strength and higher work hardening compared to tension.

The 4A-I sample exhibited the higher flow stress anisotropy and tension compression asymmetry as clearly seen in Figure 5.4.a. In this sample, most grains have

basal poles aligned with or 30-35° away from LD, and almost perpendicular to ED and FD. Therefore, the deformation during tension along LD will be accommodated mostly by tensile twinning [12, 112]. The strain hardening behavior observed along LD is an evidence of the activation of twins, i.e. a plateau region with relatively steady stress [12] or low hardening coefficient followed by an upward curvature with a high hardening rate. This kind of hardening behavior is not seen when the alloy is pulled along ED or FD. Instead, the sample exhibits typical downward hardening curvature associated with slip dominated deformation. Tension along ED and FD is similar to in-plane tension of hot rolled plate (Figure 4.5) or sheet in which basal and prismatic slip accommodate most of the deformation [108]. Interestingly, during compression of this sample, the hardening associated with twinning is observed when the alloy is compressed along ED and FD but not along LD. Compressing the sample along LD can be estimated as a through-thickness compression (TTC) of a hot rolled plate or sheet since the basal poles are almost aligned with LD similar to the normal direction of a hot rolled plate. During this compression (along LD), the material deforms mainly via basal and pyramidal $\langle c+a \rangle$ slip [112]. Moreover, this sample (4A-I sample) yields earlier in tension than in compression when tested along LD and the opposite are true when tested along ED and FD. It can also be seen in Figure 5.4.a that the hardening behavior is also different in tension and compression along the same direction, again due to the activated deformation mechanisms and thus, ECAE texture.

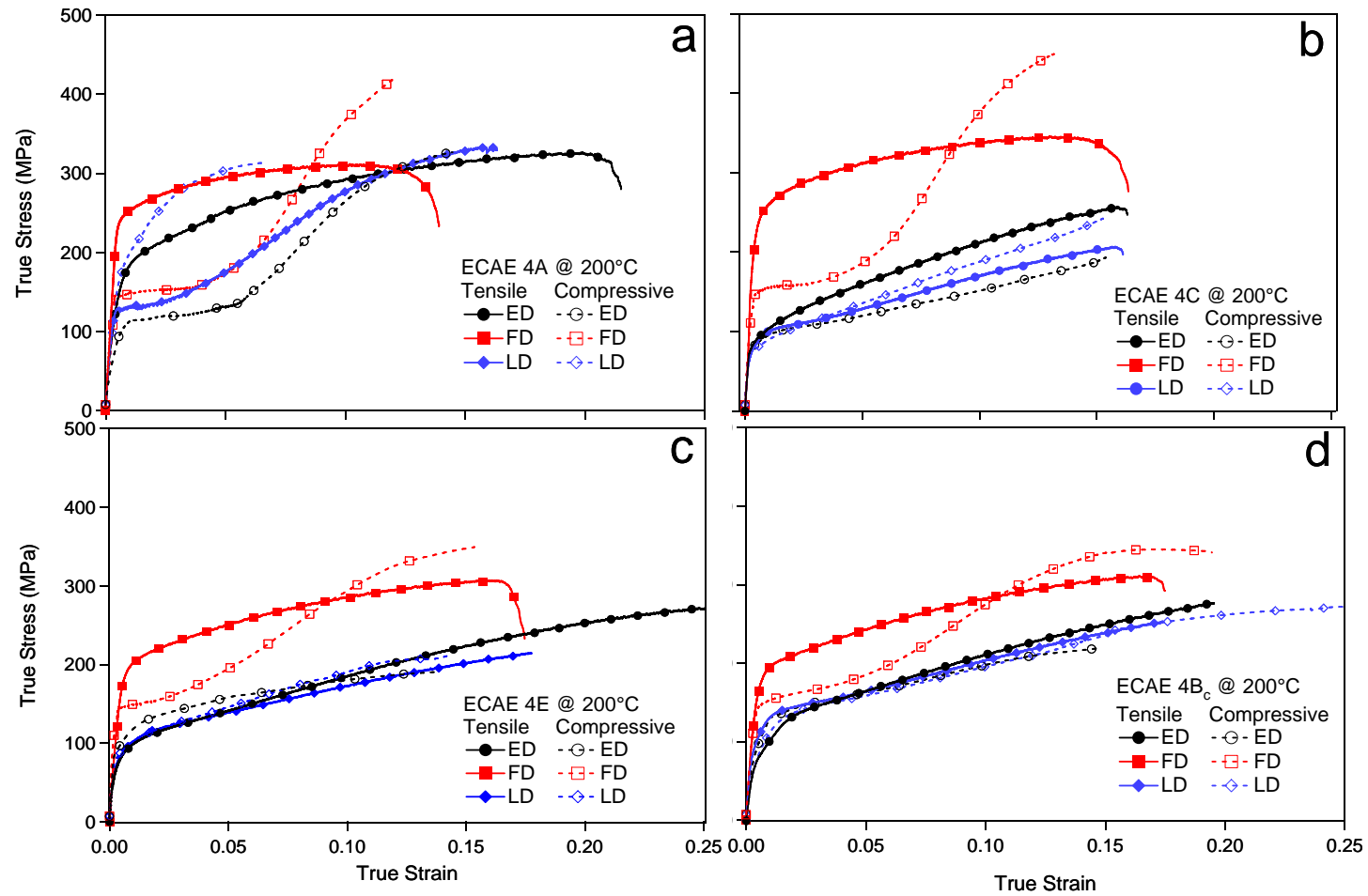


Figure 5.4 Tensile (solid lines) and compressive (dashed lines) true response of AZ31B alloy ECAE processed up to four passes following route (a) A (4A-I), (b) C (4C-I), (c) E (4E-I) and (d) B_C (4B_C-I) .

This phenomenon of opposite hardening behavior in tension and compression is also seen from the response of the other three samples, 4C-I, 4E-I and 4B_C-I when tested along FD. Moreover, the T/C asymmetry of these samples is very high along this direction and almost negligible along ED and LD. This can be attributed to the orientation of the basal poles with respect to these three directions as can be seen in Figure 5.3. In all samples, basal poles are almost perpendicular to FD because of the existence of the basal peaks closer to the rim of the pole figure. But they make an angle of 30-42° from LD and hence 60-48° from ED. This might explain the higher T/C asymmetry along FD than along ED or LD especially in the last three samples.

5.4 Low Temperature Processing of AZ31B Mg Alloy

As discussed in Chapter IV, 200 °C processing of AZ31B Mg alloy triggers dynamic recovery and recrystallization very easily. These phenomena, tends to soften the materials. Therefore, low temperature processing after the initial high temperature processing is necessary to prevent dynamic recovery and recrystallization. The advantages of these processing over conventional ECAE routes include the flexibility to produce certain deformation textures that are not possible with conventional ECAE routes after the same amount of imposed strain.

Table 5.1 Mechanical properties of ECAE processed AZ31B Mg alloy under tension and compression. The number before the billet label indicates the number of passes, and the letter represents the ECAE route. (IP: In-plane, TT: Through-Thickness, ED: Extrusion Direction, LD: Longitudinal Direction, FD: Flow Direction, SD: Stress Differential).

billet	Direction	Tension		Compression		SD (%)
		0.2% proof stress (MPa)	UTS (MPa)	0.2% proof stress (MPa)	UTS (MPa)	
As Received	IP	158.5 ± 1.5	290 ± 3.0	69.0 ± 1.4	307 ± 3.5	-78.7
	TT	58.5 ± 0.5	319 ± 5.0	126.0 ± 2.6	295 ± 5.5	73.2
4A	ED	146.35 ±11.6	328.55 ±1.85	108 ±2.0	326.6 ±3.5	-30.2
	LD	127.1 ±0.85	306.8 ±27.1	182.75 ±4.25	310.4 ±3.0	35.9
	FD	243.8 ±0.3	314 ±2.35	149.25 ±4.45	419.5 ±0.5	-48.1
4B _C	ED	83.91 ±3.0	262.9 ±13.6	100 ±1	211.6 ±7.2	17.5
	LD	98.5 ±0.1	249.3 ±4.03	99.25 ±11.75	276 ±4.0	0.8
	FD	170.7 ±1.62	308.11 ±2.89	140 ±5	341.15 ±3.75	-19.8
4C	ED	78.86 ±6.26	251.4 ±5.4	78.75 ±1.65	189.2 ±3.8	-0.1
	LD	78.1 ±1.2	189 ±17.65	62.4 ±12.1	221.3 ±20.9	-22.3
	FD	239.3 ±10.5	312.7 ±33.4	143.1 ±4	441.7 ±8.3	-50.3
4E	ED	74.75 ±8.25	268 ±4	86.6 ±8.6	186.2 ±4.45	14.7
	LD	81.59 ±2.61	213.78 ±1.19	82.6 ±2.3	216.6 ±4.8	1.2
	FD	183.5 ±4.8	303.6 ±3.6	142 ±3	322 ±27.3	-25.5

The AZ31B Mg alloy was processed using thermo-mechanical hybrid routes that include ECAE at different temperatures. Here, the results of two of these hybrid routes are presented because of their relevance of the discussion of this chapter. Starting with initial texture similar to texture I used for the cases presented in Chapter IV and this chapter. In this texture, the basal poles are oriented parallel to the extrusion direction during the first ECAE pass as shown in Figure 3.1.a. The as-received hot rolled billet was, first, annealed at 350 °C for 8 hours and canned in nickel can. Then the Ni cans was ECAE processed following route A at 200 °C for two passes with extrusion speed of 2.54 mm/s. It was then rotated by 180° (like in route C) about its extrusion axis. Two more passes were performed following route A but at a temperature of 150 °C with extrusion speed of 0.8 mm/s. The can is then rotated one more time by 180° around its extrusion axis. The fifth pass was performed at 125 °C at extrusion speed of 0.25 mm/s. Back-pressure of about 35 MPa This processing case will be designated as 5H-I representing the number of passes, the use of a hybrid route and the initial starting texture. Another AZ31B billet was processed inside a Ni can too, but for seven passes at different temperatures and extrusion speeds. It was also processed in three steps as follow: (1) four passes following route A at 200 °C with extrusion speed of 2.54 mm/s, (2) two passes following route A at 150 °C and (3) One pass at 125 °C with extrusion speed of 0.08 mm/s. This case will be called as 7H-I. The reasoning of such processing path is beyond the subject of this dissertation and details about the hybrid processing will be published soon by Foley et al.

The optical micrographs of the 5H-I and 7H-I samples are shown in Figure 5.5. An average grain size of about 2 μm is achieved, with the presence of submicron grain sizes, after those hybrid routes. The measured prismatic and basal pole figures are shown in Figure 5.6, and the predicted basal pole figures are shown Figure 5.7. The simulation of all passes, despite the different processing temperatures, was performed using the VPSC model with the same parameters used for all aforementioned cases. Interestingly, the resulting textures of the two hybrid cases fall on the same categories as those of route A and C cases. These categories will be presented later in section 5.5.2.

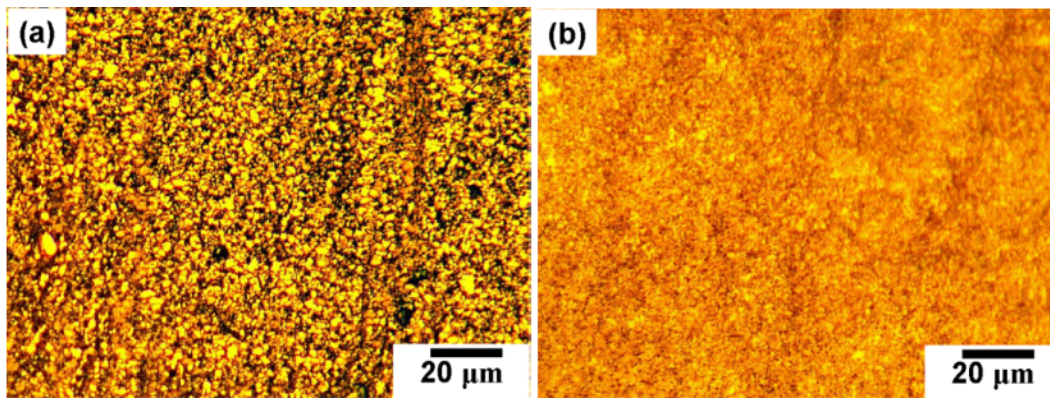


Figure 5.5 Optical micrographs of AZ31B sample ECAE processed following the hybrid route (a) 5H-I sample and (b) 7H-I sample.

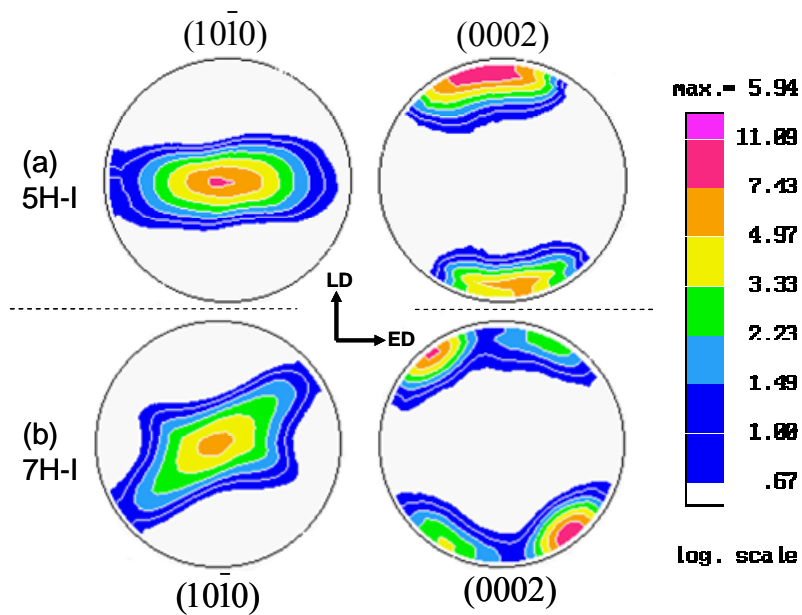


Figure 5.6 Prismatic and basal pole figures of AZ31B sample processed following (a) 5H-I and (b) 7H-I hybrid routes. The numbers in these labeling indicates the number of ECAE passes I represents the type of initial starting texture in which basal pole.

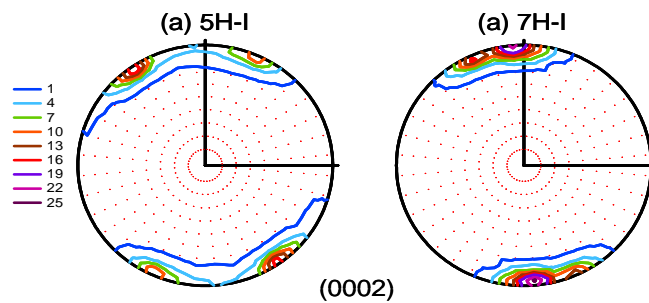


Figure 5.7 Predicted basal pole figures of AZ31B sample processed following (a) 5H-I and (b) 7H-I hybrid routes. The numbers in these labeling indicates the number of ECAE passes and I represents the type of initial starting texture in which basal pole.

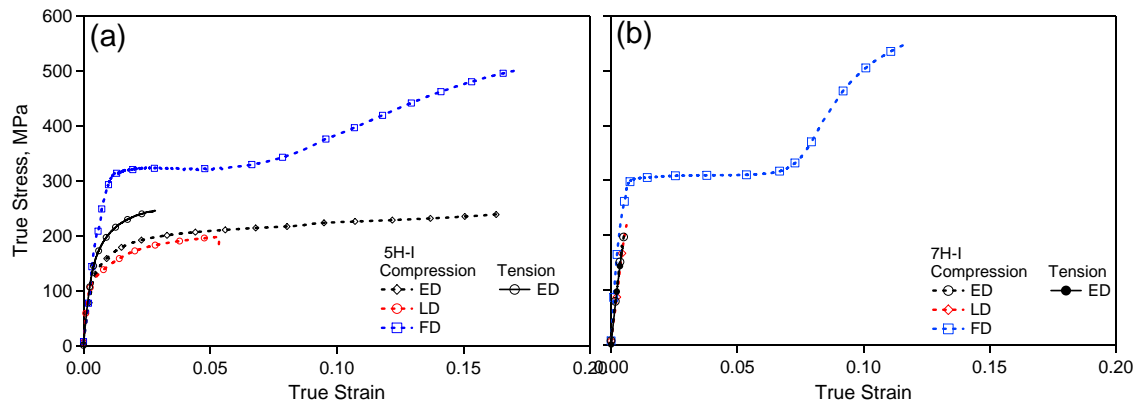


Figure 5.8 The mechanical response of the AZ31B Mg samples processed via the hybrid route (a) 5H and (b) 7H.

5.5 Discussion of Results

5.5.1 Tensile twinning and tension-compression asymmetry

The evolution of the stress differential (SD) [113] for all cases is listed in Table 5.1 and plotted as a function of ECAE routes in Figure 5.9. The mechanical responses of the 4E-I and 4B_C-I samples are very close to each other due to their similar textures as can be seen from the basal pole figures in Figure 5.3. The T/C asymmetry of the two samples along the three orthogonal directions is the same (see Figure 5.8). For these two samples, the T/C asymmetry is negligible.

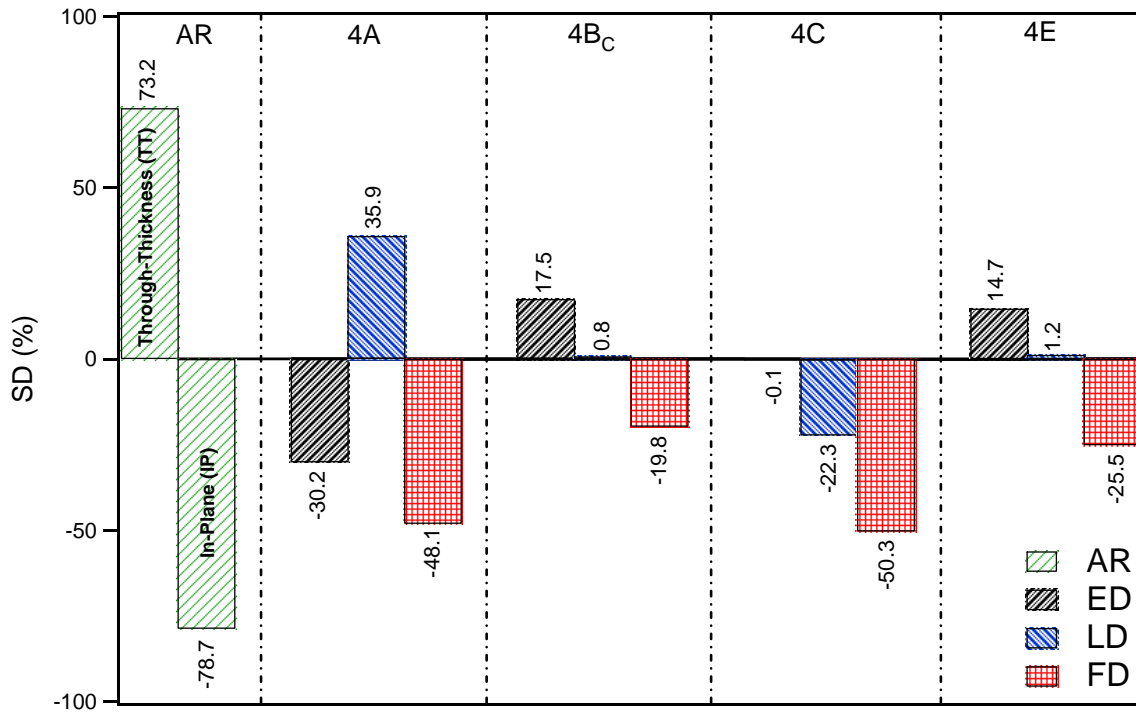


Figure 5.9 The stress differential ratio of as-received along the two plate directions, and as ECAE processed up to four passes following routes A, B_c, C and E.

Another clear observation from Figure 5.9 is that SD is always negative along the FD, i.e., the compressive yield strength is lower than the tensile one along this direction for all four cases. The basal poles of most grains in all four samples are aligned perpendicular to the FD because of the location of the basal peaks closer to the rim of the pole figure. Compression along FD will, then, activate tensile twinning similar to in-plane compression (IPC) of the hot rolled plate or sheet. The strain hardening behavior observed along FD in compression is, also, evidence of the activation of twins, i.e. a plateau region with relatively steady stress [12] or low hardening coefficient followed by an upward curvature with a high hardening rate. This strain hardening behavior is

observed in all four samples however, sample 4A-I and 4C-I have higher hardening rate than 4E-I and 4B_C-I samples. This is because that the amount of grains that have c-axis perpendicular to the compression direction (FD) is higher in the former. Therefore, they have higher Schmid factors of basal slip than those of 4E-I and 4B_C-I samples. This will result in a high amount of twinning to compensate for the lack of basal slip and hence higher amount of T/C asymmetry as can be clearly seen in Figure 5.9. The influence of tensile twinning on T/C asymmetry is also the cause of high positive SD value (35.9%) along LD of the 4A-I sample. Along this direction, the 4A-I sample has lower compressive yield strength, because of the activity of tensile twins, than its tensile yield stress.

5.5.2 Different microstructures and similar textures

From the inspection of Figure 4.4 and 4.5 showing the textures of 1A-I, 2A-I, 2C-I (or 2E-I) and 2B_C-I, Figure 5.3 showing the textures of four-pass samples and Figure 5.6 showing the textures of the hybrid route samples, the textures of all cases can be classified in three categories: (1) Texture A, which has two basal peaks close to each other and close to LD, and it includes 1A-I, 2A-I, 4A-I and 7H-I samples, (2) Texture C, which has two peaks separated by 60-65° and they make an angle of about 45° from ED and FD, and it includes 2C-I, 4C-I and 5H-I samples, and (3) Texture B_C, in which basal poles are aligned along a pole making an angle of about 27-38° from LD, and it includes 2B_C-I, 4E-I and 4B_C-I. The mechanical response in tension and compression of the samples in each category, except for hybrid routes samples, are similar to each other regardless of their microstructures (see Figures 5.4 for the mechanical response of the

four-pass samples and Figure 4.7 and 4.8 for the response of one- and two-pass samples). In Texture A category, for example, samples 1A-I and 2A-I have bimodal microstructures that consist of large grains in the order of 20 μm and very fine dynamically recrystallized (DRX) grains, while the microstructure of 4A-I sample is more uniform with an average grain size of 4 μm . The same thing can be said about the samples in the other two categories where one and two ECAE passes produce bimodal structures and four passes make the microstructure more uniform.

As a continuation of the effects of tensile twinning on T/C asymmetry, the activity of tensile twinning during compression along FD of Texture A samples should be emphasized. The 1A-I sample has the lowest compressive yield strength among the Texture A samples (1A, 2A and 4A) along FD. As discussed earlier, all three samples yielded under compression, along this direction, as a result of the activation of tensile twinning. The SD values along FD of 1A-I, 2A-I and 4A-I samples are -40, -30 and -48%, respectively. Samples 2A-I and 4A-I yielded in tension almost at the same stress value despite the observed microstructural difference. Therefore, the higher value of SD of 4A sample is because of its lower compressive yield strength and hence its higher ease of twinning.

5.5.3 Slip and twinning dependence on grain size

Figure 5.10 shows the mechanical response in tension and compression along the flow direction (FD) of Texture A and Texture C samples. The two textures as discussed earlier has basal poles of most grains oriented perpendicular to the FD. Therefore, during compression along this direction, tensile twinning is activated as can be seen from the

hardening behavior of all samples (dashed lines). Tension along this direction is accommodated by slip systems mainly prismatic and basal systems. Only compression tests were performed on the hybrid routes samples (5H-I and 7H-I) because of the size limitations of the processed samples. The important observation from these curves, is the effect of the thermo-mechanical hybrid processing on the activity of twins during compression along FD. The compressive yield strength of the hybrid samples is almost twice that of the conventionally ECAE processed samples. The differences between these samples are the grain sizes and morphology and the amount of dislocations. The lower processing temperature at the final stages of the hybrid processing is expected to reduce dynamic recovery and recrystallization and, hence, increase the dislocation density inside the grains and at the grain boundaries. As discussed in Chapter IV, dynamic recovery and DRX have detrimental effects on yield strength of the material by reducing the dislocation density and introducing new unstrained grains. However, no effects of dynamic recovery and DRX were observed on the compressive yield strength along ED (See Figure 4.7.a, 4.8.a and 5.4.a and Figure 4.8.b, 5.4.b and 5.8.a). During this compression, plastic deformation is accommodated mainly by slip.

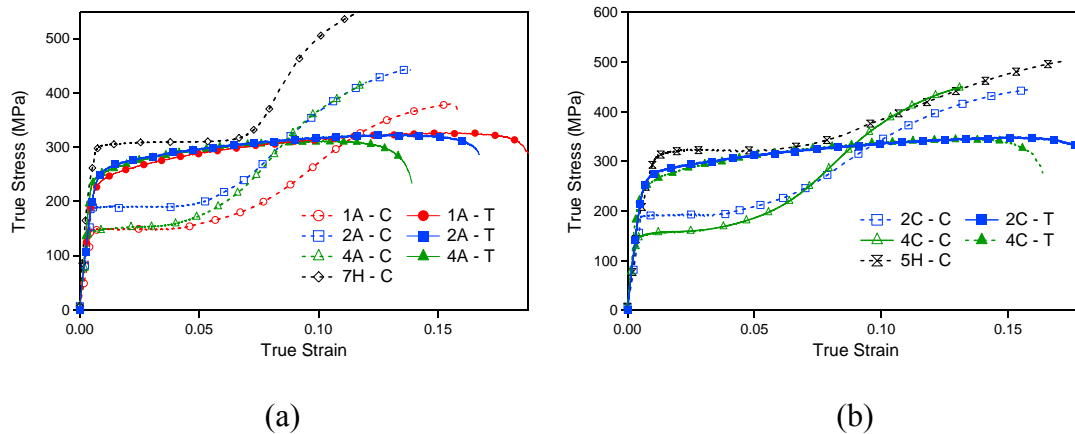


Figure 5.10 The mechanical response along flow direction (FD) of (a) Texture A samples and (b) Texture C samples.

5.6 Summary of Observations

AZ31B Mg alloy was successfully processed up to four passes following routes A, C, E and B_C. The texture evolution during ECAE was successfully predicted using a VPSC crystal plasticity model. The mechanical responses of the processed samples revealed the significance of the crystallographic texture on flow stress anisotropy and tension-compression asymmetry. The main findings of this study can be summarized as follow:

1. Higher number of ECAE passes leads to more uniform microstructures with finer grain sizes.
2. Routes E and B_C result in more uniform microstructures than those produced by routes A and C. Route B_C is leads to finest grain size.

3. Low temperature processing of AZ31B Mg alloy was successful after initial high temperature processing. Smaller grain sizes were achieved using the multi-temperature processing.
4. Despite the dynamic recrystallization observed during ECAE of Mg alloys, the texture evolution was successfully predicted using VPSC following different conventional and hybrid ECAE routes and up to seven passes.
5. Samples with different microstructures but very close crystallographic textures have similar mechanical response in tension and compression along different directions.
6. The activity of tensile twinning during monotonic testing leads to the T/C asymmetry.

CHAPTER VI

PREDICTION OF FLOW STRESS ANISOTROPY AND TENSION-

COMPRESSION ASYMMETRY OF AZ31B MG ALLOY

In this chapter, the mechanical response of as received hot rolled AZ31B Mg plate along its two directions is predicted using the same visco-plastic self-consistent (VPSC) model coupled with a dislocation-based hardening scheme. The same hardening parameters are then used to predict the response of the ECAE processed samples along the three orthogonal directions of the billet.

6.1 Dislocation-based Hardening Formulation

The aforementioned VPSC model coupled with the dislocation-based hardening formulation developed by Beyerlein and Tome' [91] was used to predict the stress-strain response of AZ31B Mg alloy. For each slip mode α , a dislocation population is evolved explicitly as a function of temperature and strain through thermally-activated recovery and debris formation.

Work hardening is linked to the evolution of dislocations, their interactions with each other, and with barriers in the microstructure. Therefore, the critical strength or slip resistance of each slip $s \in \alpha$, τ_c^s evolves as follows:

$$\tau_c^s = \tau_0^\alpha + \tau_{forest}^\alpha + \tau_{deb}^\alpha + \tau_{HP}^s, \quad s \in \alpha \quad (6.1)$$

where τ_0^α is the initial slip resistance which depends on slip mode α , solute density, and T and $\dot{\varepsilon}$. The second and third terms on the right hand side of equation 6.1 represent the work hardening due to dislocation interactions. The last term, τ_{HP}^s , is the barrier effect provided by grain or twin boundaries whichever constrains the mean free path of dislocations more.

An evolution model for dislocation density developed by Essman and Mughrabi [95] and further developed by Mecking and Kocks [96] was used to describe the dislocation density evolution and it is expressed as follow:

$$\frac{\partial \rho^\alpha}{\partial \gamma^\alpha} = k_1^\alpha \sqrt{\rho^\alpha} - k_2^\alpha(\dot{\varepsilon}, T) \rho^\alpha \quad (6.2)$$

where k_2^α is calculated as a function of strain rate, $\dot{\varepsilon}$ and temperature T and it controls the rate-sensitivity of dislocation removal. It increases with T and decreases with $\dot{\varepsilon}$ as shown in the following equation:

$$\frac{k_2^\alpha(\dot{\varepsilon}, T)}{k_1^\alpha} = \frac{\chi b^\alpha}{g^\alpha} \left(1 - \frac{kT}{D^\alpha b^3} \ln \left(\frac{\dot{\varepsilon}}{\dot{\varepsilon}_0} \right) \right) \quad (6.3)$$

where χ is an interaction parameter between 0.1 and 1.0, b is the Burger vector of the slip system α , D is a proportionality factor of unit of stress, g is normalized stress-independent activation energy and k is the gas constant. In equation (6.3), the constant k_1 affects the dislocation generation during plastic deformation. In thermally activated glide, usually the dislocation multiplication is rate insensitive compared to dislocation

removal processes [91]. Therefore, k_I is set as a function of material and not of strain rate or temperature. D and g are the thermal activation parameters.

The third term on the RHS of equation 6.1 which is the contribution of ρ_{deb} is expressed as follow

$$\tau_{deb}^{\alpha} = k_{deb} \mu b^{\alpha} \sqrt{\rho_{deb}} \log \left(\frac{1}{b^{\alpha} \sqrt{\rho_{deb}}} \right) \quad (6.4)$$

Where k_{deb} is a material-independent constant determined to be 0.86 [97] and ρ_{deb} evolves with plastic strain as follow

$$\partial \rho_{deb,tot} = q \sum_{\alpha} f^{\alpha} \frac{\partial \rho_{rem}^{\alpha}}{\partial \gamma^{\alpha}}, \text{ and } f = \frac{nb^{\alpha}}{l_{deb}} \approx A^{\alpha} b^{\alpha} \sqrt{\rho_{deb}} \quad (6.5)$$

where A is set as a logarithmic function of T , such that $A=Q_0+Q_1 \ln(1+T/Q_3)$. This third term τ_{deb}^{α} affects mainly stage IV. In this work, this stage has not been included due to time limitations. Therefore, values of $A = 1$ were set for all slip systems. Substituting for each term in equation 6.1, the resistance to slip of each system $s \in \alpha$ evolves from a zero-strain value calculated to be:

$$\tau_c^s(\gamma = 0) = \tau_0^{\alpha}(T) + \mu HP^{\alpha} \sqrt{\frac{b^{\alpha}}{d_g}} + b^{\alpha} \chi \mu \sqrt{\rho_0^{\alpha}} \quad \forall s \in \alpha \quad (6.6)$$

assuming no twins are present before deformation and the amount of debris is negligible, to a final value of

$$\tau_c^s = \tau_0^{\alpha}(T) + \mu HP^{\alpha\beta} \sqrt{\frac{b^{\alpha}}{d_{mfp}^{s,PTS}}} + b^{\alpha} \chi \mu \left[\sqrt{\rho^{\alpha}} + \frac{k_{deb}}{\chi} \sqrt{\rho_{deb}} \log \left(\frac{1}{b^{\alpha} \sqrt{\rho_{deb}}} \right) \right] \quad \forall s \in \alpha \quad (6.7)$$

6.2 Prediction of Hot-rolled Sample Mechanical Response

In this work, three slip systems and one twin system have been considered to predict the room temperature mechanical flow response of AZ31B Mg alloy. These deformation modes are listed in Table 6.1. The hardening parameters for the slip systems are listed in Table 6.2. The critical resolved shear stress for the tensile twinning system is set to 35MPa. As can be seen from Table 6.2, there are at least ten parameters for each slip system. The estimation of these parameters is achieved by running series of uniaxial tension and compression tests at several temperatures, since some of these parameters are functions of temperature. Some of these parameters should be material properties. However, the lack of experimental procedures to measure them for each individual slip system limits the solution to finding these parameters to fitting the measured stress-strain curves following trial-and-error approach. This fitting process can be highly improved by testing single crystals along different directions along which limited known slip or twinning systems are expected to take place.

Table 6.1 Deformation modes considered in the prediction of the stress-strain response.

Slip	Plane	Direction	Number of systems
Basal	$\{0002\}$	$\langle 11\bar{2}0 \rangle$	3
Prismatic $\langle a \rangle$	$\{1\bar{1}00\}$	$\langle 11\bar{2}0 \rangle$	3
2nd order pyramidal $\langle c+a \rangle$	$\{11\bar{2}2\}$	$\langle 11\bar{2}3 \rangle$	6
Tensile twinning	$\{10\bar{1}2\}$	$\langle 10\bar{1}1 \rangle$	6

Table 6.2 Hardening parameters for slip systems considered in the predictions.

	Basal	Prismatic	Pyramidal <c+a>
k_1^α	1.5E+9 m	2.5E+9 m	3.1E+9 m
ε_0^α	1.0E+7	1.0E+7	1.0E+7
g_1^α	0.5E-2	0.5E-2	9.75E-3
D_0^α	0.5MPa	5000MPa	6000MPa
τ_0^α	2.0 MPa	60.0 MPa	50.0 MPa
q	4	4	4
χ	0.9	0.9	0.9
HP^α	100	100	350
$HP^{\alpha\beta}$	1000	100	1000
A	1.0	1.0	1.0

Figure 6.1 shows the experimental and predicted compressive and tensile stress-strain curves of as-received hot rolled sample. The type of hardening observed along the two directions of the hot rolled plate was predicted. Through thickness compression (TTC) and in-plane tension (IPT) have slip dominated deformation. The strain hardening during through thickness tension (TTT) and in-plane compression (IPC) has twin characteristic.

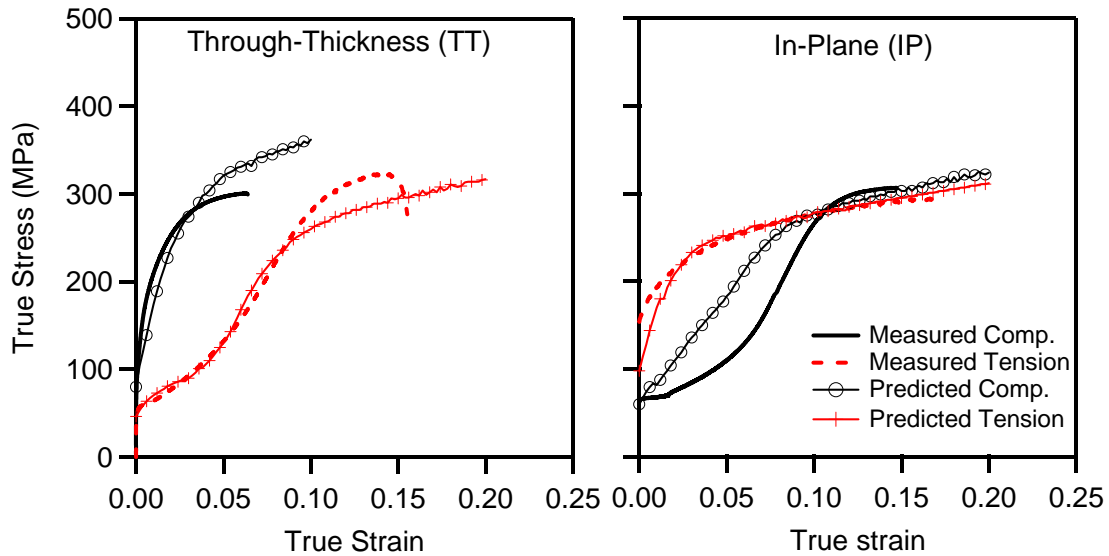


Figure 6.1 Experimental (lines) and predicted (symbols) of the as-received hot rolled sample.

Figure 6.2 shows the predicted relative activities during these tests inside the grains and twins. Despite the similar hardening response during TTC and IPT, the governing mechanisms are different as can be seen in Figure 6.2.a and 6.2.c. In TTC, all plastic deformation is accommodated by basal and pyramidal $\langle c+a \rangle$ slip systems, while, prismatic slip accommodates most of the deformation during IPT. Tensile twinning is activated at the beginning of both TTT and IPC. This results in the no-hardening plateau at stage II. The hardening rate observed afterward, is due to the activity of slip systems inside the twins and hence the effect of twins as barriers to the dislocation movements. These effects are accounted for in the model by the HP_{mfp} , representing the Hall-Pitch effect of the mean free path of the twins (see Figure 2.12).

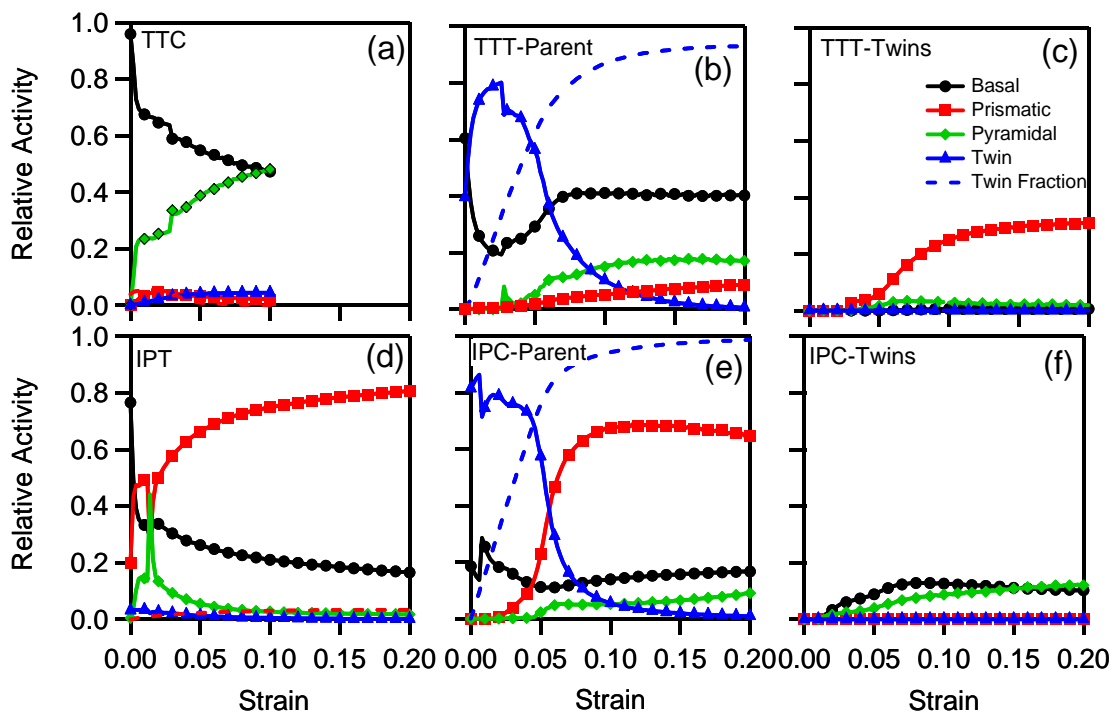


Figure 6.2 The predicted activities of deformation modes during (a) Through-Thickness Compression (TTC), (b) Through-Thickness Tension (TTT) in parent grains and (c) in twins, (d) In-Plane tension (IPT) and, (e) In-Plane compression in parent grains and (f) in twins, of the as-received hot rolled AZ31B Mg sample.

6.3 Prediction of Mechanical Response of ECAE Processed AZ31B Mg Alloy

Without considering the evolution of hardening parameter during ECAE, the predicted stress-strain curves of AZ31B ECAE processed samples up to four passes are shown in Figure 6.3. Those samples processed up to one and two passes have non-uniform bimodal microstructures consisting of large and fine DRX grains. Since, the dislocation hardening model used in the prediction does not account for such non-

uniform microstructures, the response of those samples are not predicted. Four-pass samples have more uniform microstructures as discussed in Chapter V.

It is important to note that the evolution of hardening parameter that is expected during ECAE, was not taken into account in the prediction of four-pass samples response. Exactly the same hardening parameter used for as received sample, including critical resolved shear stresses and dislocation densities, have been used for the modeling of stress-strain response of samples processed up to four ECAE passes. Despite this fact, the model was able to predict to some degree the hardening behavior of these samples along the three directions.

6.4 Discussion of Results

In order to find out the model parameters, tension and compression tests were carried out along the two directions of the hot rolled plate. These tests however, were performed only at room temperature. Some parameters in this model are temperature and strain dependent. Therefore, tests at several temperatures and strains are required to obtain the right parameters. These tests have not been done in this dissertation due to the time limitation. Despite this fact, the model was able to predict the hardening response.

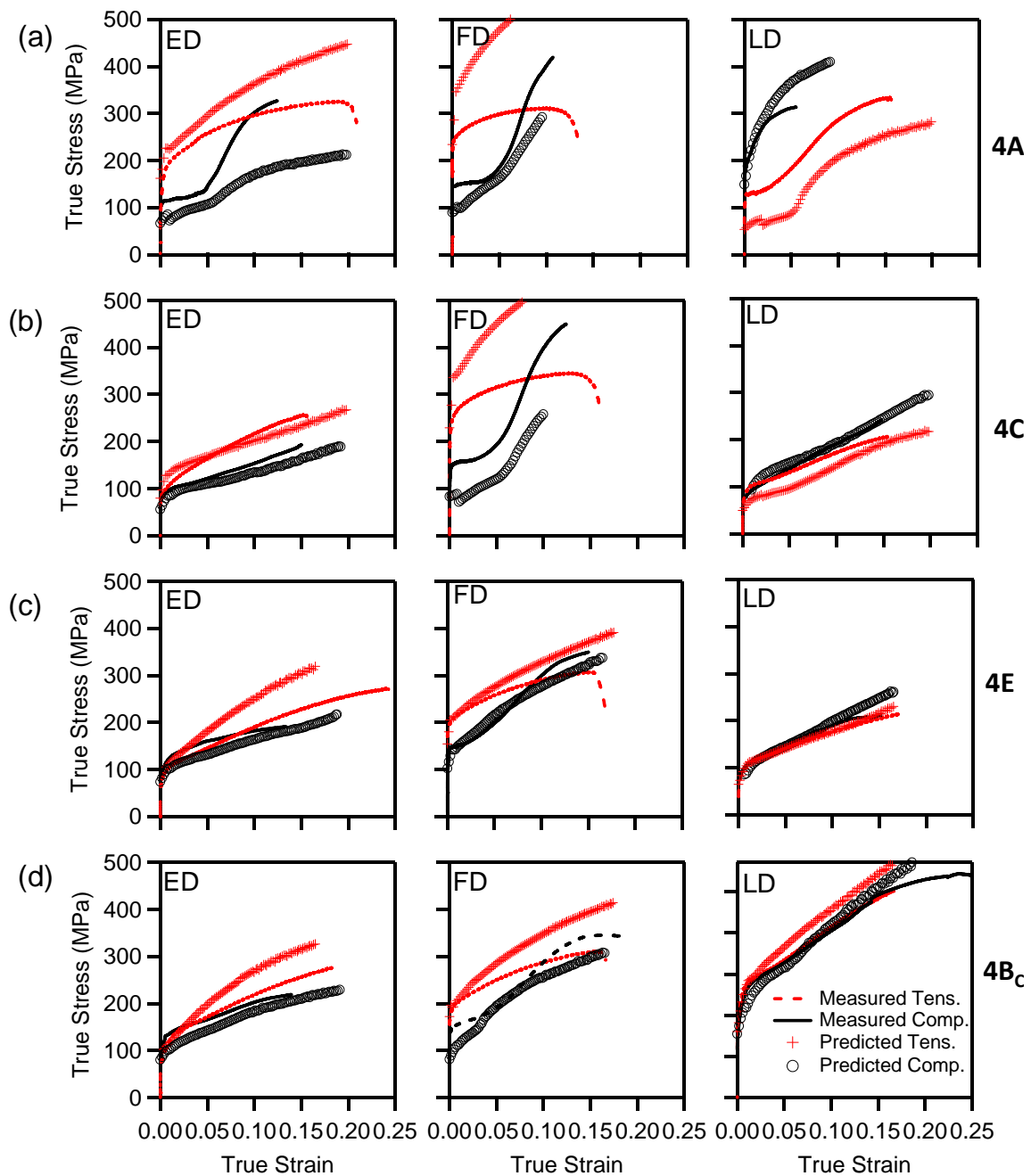


Figure 6.3 Experimental (lines) and predicted (symbols) of AZ31B samples ECAE processed up to four passes following route (a) A (4A-I), (b) C (4C-I), (c) E (4E-I) and (d) B_c (4B_c-I).

6.4.1 Governing mechanisms during through-thickness and in-plane monotonic testing of hot rolled plate

As discussed in Chapter IV, the tension compression asymmetry of the AZ31B Mg hot rolled plate is high along the two plate directions: through-thickness and in-plane, where the stress differential (SD%) values were -78% and 73% along IP and TT directions, respectively. Figure 6.2 shows the predicted relative activities during tension and compression of the rolled plate. Tensile twinning is activated during stage II and III of deformation in TTT and IPC. The twin fraction reaches 90% of the matrix in both cases. In TTC and IPT, however, negligible amount of tensile twinning is observed in Figure 6.2.a and 6.2.d. Deformation during TTC is accommodated by basal and pyramidal slip systems. In IPT, deformation is accommodated by mainly prismatic and basal slip systems.

Figure 6.2.c and 6.2.f shows the predicted relative activities inside the twins. It is very obvious, that there is a delay on the start of activities of slip systems inside the twins. This delay governs the size of the plateau region observed at stage II. Klimanek and Pöttsch [36] pointed out that at strains below 8%, while profuse $\{10\bar{1}2\}$ twinning takes place, there is little dislocation accumulation. In other word, twinning delays the onset of gross dislocation plasticity [114]. It is well known that the tensile twinning reorient the twinned region by 86.4° . This explains the difference in slip systems activated in the matrix and twins. During TTT, for example, plastic deformation inside twins is accommodated by prismatic slip similar to IPT. The same thing can be said

about deformation inside twins during IPC, where only basal and pyramidal are active similar to deformation during TTC.

6.4.2 Deformation mechanisms of ECAE processed samples

Figure 6.4 shows the predicted relative activities during tension along the FD of the ECAE processed AZ31B Mg samples up to four passes. The response of these four samples along this direction is similar as shown in Figure 5.4 and 6.3. The samples of 4E-I and 4C-I are, however, softer than 4A-I and 4C-I samples. The measured and predicted basal pole figures of the four samples are shown in Figure 5.3. Basal poles of most grains in all four samples are oriented with the FD. Therefore, these samples are expected to deform mainly by slip systems in tension along FD similar to IPT of hot rolled plate. This deformation behavior is seen very clearly in 4A-I and 4C-I samples where plastic deformation is accommodated mostly by prismatic slip. In 4E-I and 4B_C-I samples, the basal poles are more randomly distributed with respect to FD, although, most of them are oriented perpendicular to this direction. In fact, basal poles of significant amount of grains in these two samples have basal poles parallel to FD. This triggers some activity of tensile twinning during tension along FD as can be seen in Figure 6.4.c and 6.4.d.

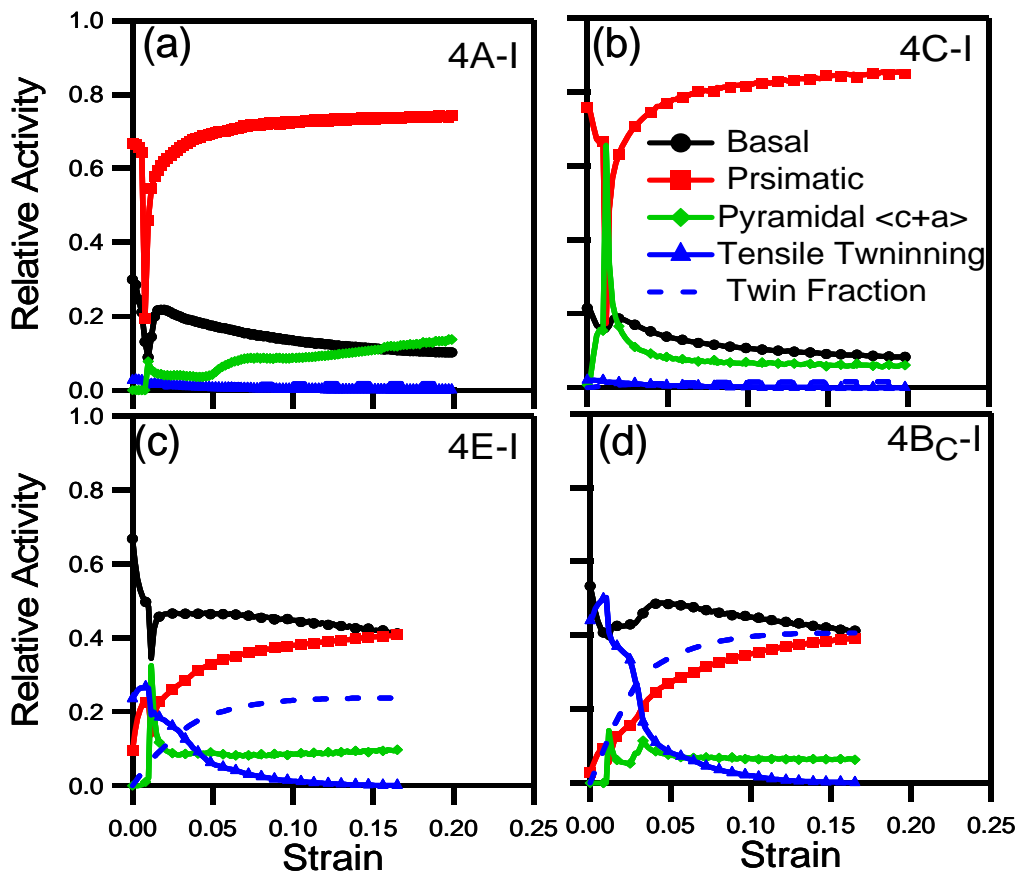


Figure 6.4 The predicted relative activities of deformation modes during tension along the FD of the AZ31B ECAE processed up to four passes following route (a) A (4A-I), (b) C (4C-I), (c) E (4E-I) and (d) B_C (4B_C-I).

The flow direction of the processed samples is of great interest because it is the strongest direction in tension (see Table 5.1 and Figure 5.4) and these samples demonstrate the highest T/C asymmetry along this direction as can be seen in Figure 5.9. As can be seen in Figure 6.4.a and 6.4.b, the activity of basal slip system is much lower than that of prismatic slip. Since basal is the easiest slip system, the material demonstrated higher tensile yield strength along FD due to the more restricted basal

orientation which is being perpendicular to the testing direction (FD). When the basal activity increases, as seen in Figure 6.4.c and 6.4.d, due to more favorable basal orientation, the tensile yield strength decreases.

6.5 Summary of Observations

The visco-plastic self-consistent polycrystalline plasticity model coupled with a dislocation-based hardening scheme was used to predict the stress-strain response of hot rolled AZ31B Mg plate in tension and compression. The same model parameters then used to predict the flow stress anisotropy and tension-compression asymmetry of ECAE processed samples. The main observations are summarized as follows:

1. The VPSC model coupled with the dislocation-based hardening scheme was able to predict the hardening response of as-received hot rolled AZ31B Mg plate.
2. The tension-compression (T/C) asymmetry observed during monotonic in-plane and through-thickness tension and compression is mainly because of the directionality of tensile twinning. Tensile twinning is activated only by a resolved tensile stress along the c-axis of the grains. This is why it is activated during through thickness tension (TTT) and in-plane compression (IPC) of hot rolled plate.
3. Tensile twinning reorients the twinned region by about 90° from the loading direction.

4. An acceptable prediction of flow stress anisotropy and tension-compression asymmetry of ECAE processed AZ31B Mg alloy up to four passes following four different ECAE routes.
5. Lower activity of basal slip systems due to the more restricted basal orientation during room temperature monotonic tests increases the tensile yield strength of the sample and T/C asymmetry.

CHAPTER VII

FLOW RESPONSE OF A SEVERE PLASTICALLY DEFORMED TWO-PHASE ZINC-ALUMINUM ALLOY

In this chapter, the effects of microstructural refinement and the evolution of microstructural morphology on the mechanical response of the ECAE processed Zn-Al alloy are discussed. A comparison between the current alloy (Zn-8wt% Al) and other similar Zn-Al alloys (Zn-12wt% Al, Zn-27wt% Al and Zn-40wt% Al) is presented in terms of the amount of improvement in strength and ductility, and the flow softening taking place after further ECAE processing. Microhardness measurements and microprobe analysis are also used to investigate possible reasons for the flow softening. Monotonic tensile tests were conducted at room temperature along the extrusion direction in addition to the directions parallel and perpendicular to the long axis of the elongated hard eutectoid phase particles in order to reveal the effect of microstructural morphology on the anisotropic flow response.

7.1 Microstructural Evolution during ECAE

Figure 7.1 shows the optical micrographs of the as-cast and ECAE processed ZA-8 taken from the flow plane of the billets. ZA-8 alloy lies left side of the eutectic composition in the Al-Zn phase diagram (Figure 2.9) where the primary phase is β which exists as numerous small and particulate dendrites in an eutectic matrix above the $C\text{-}\square$ eutectoid temperature of 275 °C [79]. Upon cooling below the eutectoid temperature, the β phase decomposes into α and η giving its lamellar structure. Therefore, the

microstructure of the as-cast alloy (Figure 7.1.a) consists of a dendritic structure with eutectoid dendrites (fine $\alpha + \eta$ lamellae) dispersed in a eutectic matrix ($\alpha + \eta$ phase). After the first ECAE pass, the dendrites were partially fragmented and macroscopic shear bands are present throughout the structure (Figure 7.1.b). After the second pass, the dendritic structure was completely eliminated and an elongated structure consisting of parallel bands of the eutectoid particles and the eutectic matrix was developed (Figure 7.1.c). More ECAE passes led to further refinement and uniform dispersion of the primary eutectoid particles in the eutectic matrix as can be seen in Figure 7.1.d which shows the microstructure of the sample processed up to eight ECAE passes following route B_C.

The effects of processing route on the microstructure and especially on the size, shape and distribution of the eutectoid particles can be seen in Figure 7.2. This figure shows the optical micrographs of the samples processed following route C, B_A, B_C and E up to eight passes. The hard eutectoid phase is finer in the samples processed following routes B_A, B_C and E. The microstructure of the alloy processed via route C is less homogeneous than those processed via other routes. Moreover, this structure contains large unbroken eutectoid particles in addition to the elongated bands as a sign of non-uniform deformation throughout the bulk of the material. In contrast, the eutectoid phase on the samples processed via routes B_C and E possesses an elongated and ribbon-shaped morphology throughout the structure. These eutectoid phase bands are, also, finer and distributed more uniformly in the matrix.

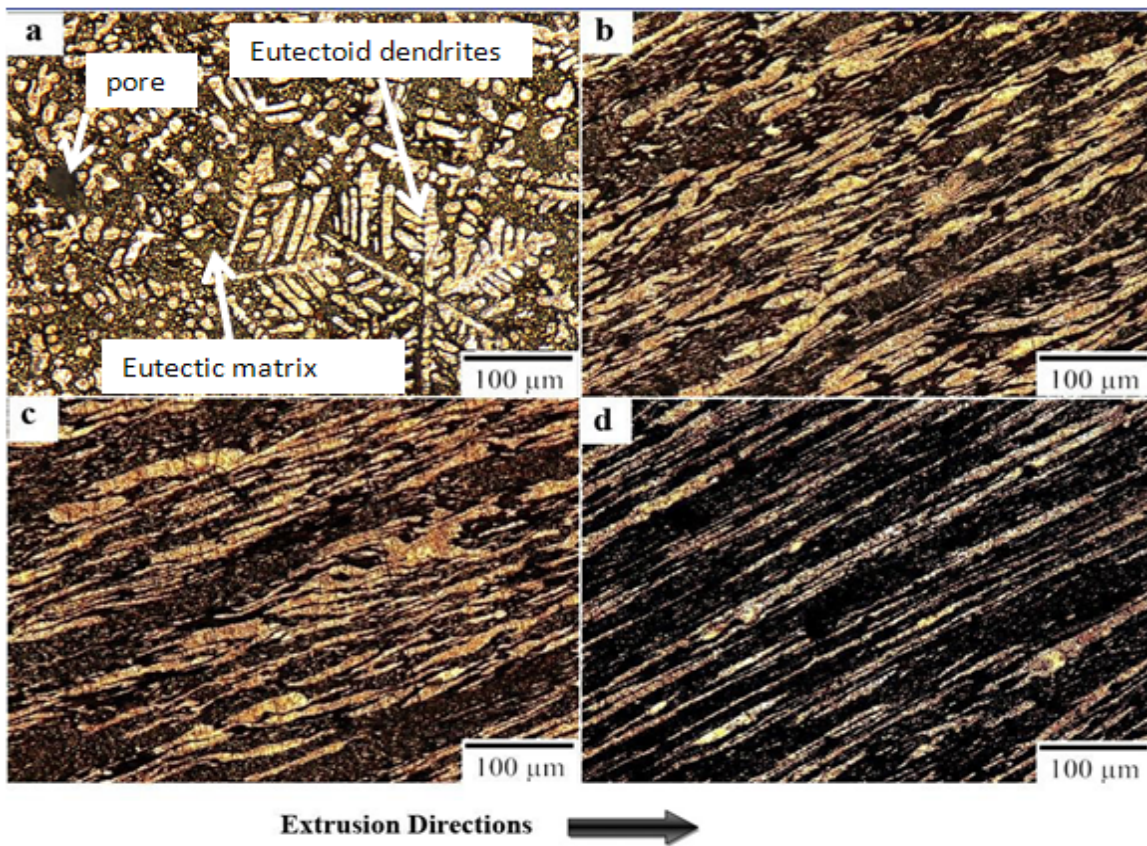


Figure 7.1 Optical micrographs of (a) the as-cast ZA-8 alloy and ECAE processed alloy for (b) one pass, (c) two passes, and (d) eight passes in route B_C. The aluminum-rich α -phase is the light phase and the zinc-rich eutectic matrix ($\alpha + \eta$) is the dark one.

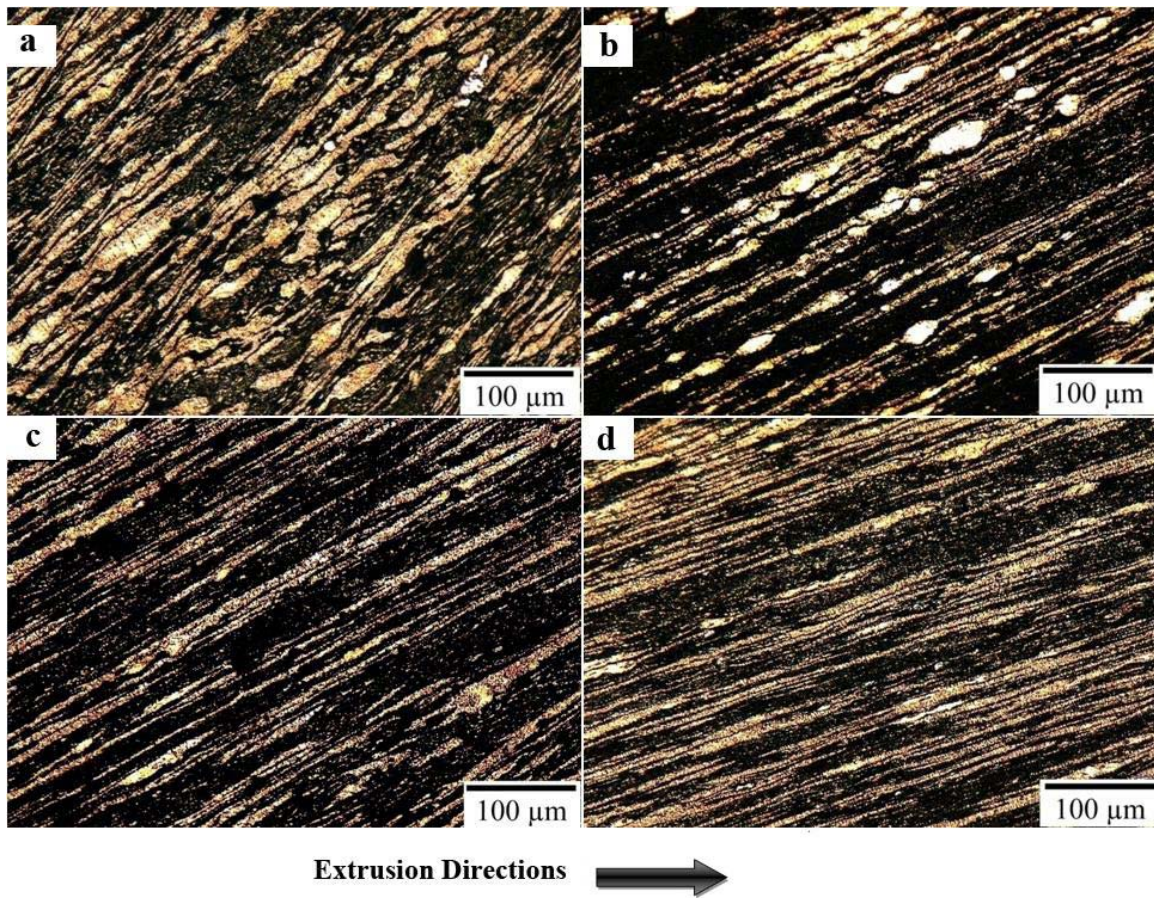


Figure 7.2 Optical micrographs of ECAE processed ZA-8 alloy up to eight passes via (a) route C, (b) route B_A, (c) route B_C and (d) route E.

7.2 Tensile Flow Response

The effect of the number of ECAE passes on the true tensile stress – strain responses of the as-cast ZA-8 alloy is shown in Figure 7.3. The basic mechanical properties extracted from these curves and the curves in Figure 7.4 are summarized in Table 7.1. From Figure 7.3, it can be seen that the ultimate tensile strength and elongation to failure were significantly enhanced after ECAE. A relatively high ultimate tensile strength was achieved after the first pass and then it slightly decreased after the second pass following route B_C, but it finally increased to a higher value after eight passes than that of the first pass sample. An average increase in ultimate tensile strength of about 50% was achieved after eight passes. The elongation to failure continued to increase with number of passes with a maximum value of about 61% achieved via route B_C compared to 0.6% of as-cast alloy.

It can be seen in Figure 7.4 that the true stress vs. true strain curves of the processed samples peaked directly soon after the yielding and demonstrated an extended no hardening regime before flow softening started. This figure also shows that the resulting strength and ductility levels are a strong function of the ECAE route. The effect of processing route on ductility seems to be much more pronounced than that on strength. The sample processed following route C shows the lowest strength and ductility after 8 passes compared to other routes. Its strength and ductility values are even less than those of the sample processed up to only two passes in route B_C. Owing to their similar microstructures (Figure 7.2), the stress-strain response of the materials

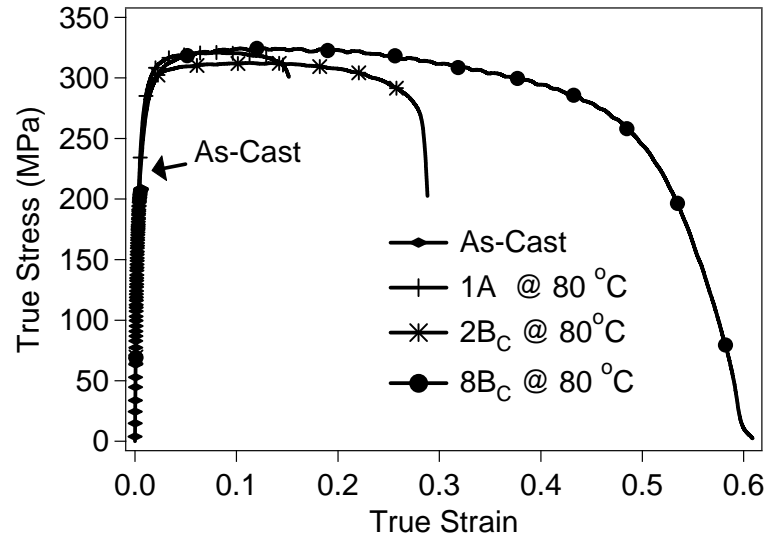


Figure 7.3 Room temperature true tensile stress vs. strain curves of the as-cast ZA-8 alloy and the samples ECAE processed using route B_C up to 8 passes.

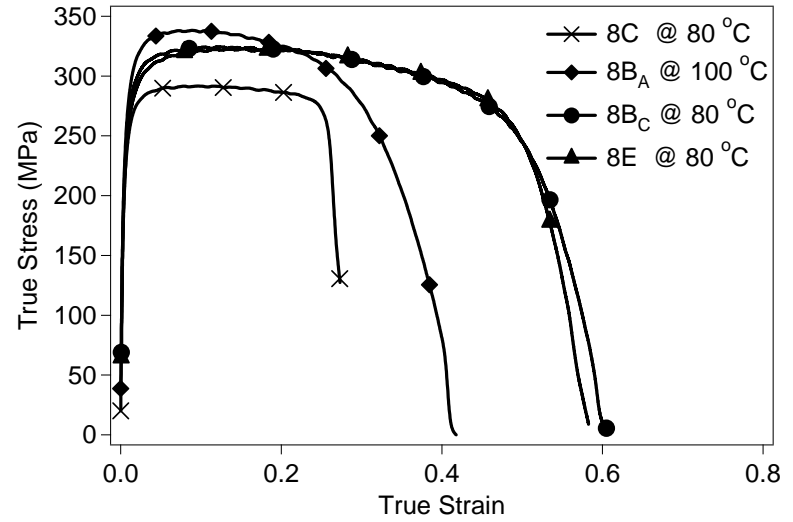


Figure 7.4 Room temperature true stress vs. true strain curves of the ECAE processed ZA-8 alloy up to eight passes using different processing routes.

Table 7.1 Tensile properties of the as-cast and ECAE processed ZA-8 alloy. HP: Major axis direction of the hard phase.

Route	Number of passes	Extrusion Temperature (°C)	Tensile Direction	Elongation at fracture (%)	Ultimate Tensile Strength (MPa)
As-Cast	NA	NA	NA	0.6 ± 0.05	217 ± 9
A	1	80	ED	15.6 ± 0.1	319 ± 2
			Parallel to HP	12.1 ± 2.1	330 ± 1
			Perp. to HP	4.4 ± 0.9	321 ± 1
B _C	2	80	ED	33.3 ± 6.3	315 ± 3
			Parallel to HP	34.5 ± 7.5	371 ± 1
			Perp. to HP	20.1 ± 6.4	323 ± 2
C	8	80	ED	28.4 ± 1.7	287 ± 6
B _A	8	100	ED	41.2 ± 0.6	336 ± 5
B _C	8	80	ED	60.8 ± 1.0	321 ± 4
			Parallel to HP	58.8 ± 3.7	340 ± 2
			Perp. to HP	49.4 ± 2.9	334 ± 6
E	8	80	ED	61.4 ± 3.1	319 ± 4

processed via routes E and B_C after eight passes are almost identical. The sample processed via these routes exhibit higher elongation to failure than those processed via route C and B_A. Route B_A, on the other hand, results in the highest ultimate tensile strength levels, probably because of the maximum refinement in the eutectoid hard phase after this route compared to other routes, yet the ductility in the Route B_A samples are relatively low as compared to those for Routes B_C and E due to the non-uniform nature of this refinement (Figure 7.2).

The macroscopic appearance of the failed tensile samples is shown in Fig 7.5. In the as-cast sample, there was no necking and the sample demonstrated brittle fracture without notable plastic deformation. The fracture surface of the as-cast sample is basically normal to the tensile axis. Whereas, the samples extruded up to eight passes,

excluding the one processed via route C which demonstrated brittle fracture with no neck formation, exhibited highly ductile fracture in which the samples necked down to almost a point at high plastic deformation levels.

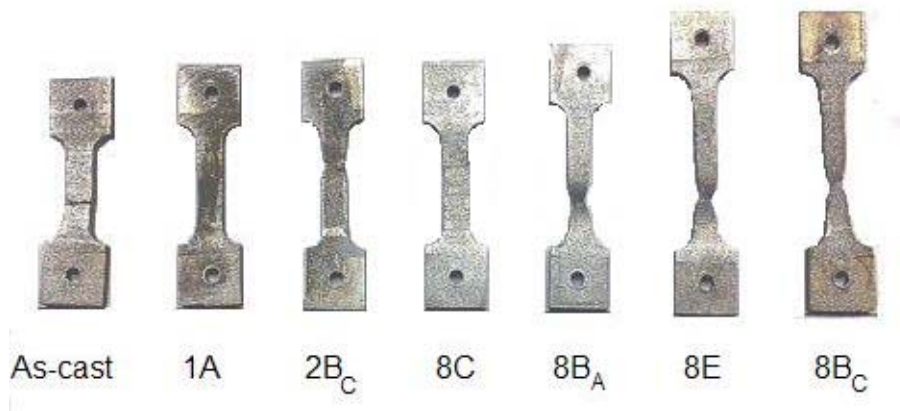


Figure 7.5 Macroscopic appearance of the failed tensile samples in the as-cast and ECAE processed conditions.

In addition to the tensile tests along the longitudinal axis of the ECAE samples, i.e. the extrusion direction (ED), the tests were also carried out parallel and perpendicular to the long axis of the hard phase particles, orientation of which determined using the OM images in Figure 7.1. Tensile responses of the 1A, 2B_C and 8B_C samples along the three directions are shown in Figure 7.6. The macroscopic appearance of the failed tensile specimens is also included in the figure. The anisotropy in the flow strength and elongation to failure is the most pronounced in the 2B_C sample. This anisotropy then tends to decrease with further processing and hence, with the further refinement, fragmentation, and more homogeneous distribution of the hard phase

particles, and chemical homogenization than in the hard phase particles, as will be shown in the next section. The 8B_C samples have the same strength levels when tested parallel and perpendicular to the long axis of the hard eutectoid phase bands. The necking however starts earlier when the sample is pulled in a direction perpendicular to these bands, thus leading to a lower elongation to failure value. These hard second phase bands basically act as fiber reinforcement in the softer Zn-rich matrix. However, their effectiveness diminishes with the number of passes due to chemical homogenization in the hard eutectoid phase which will be the focus of next section.

7.3 Wavelength Dispersive Spectroscopy (WDS)

WDS of the as-cast and ECAE processed ZA-8 alloy revealed changes in the composition of the constitutive phases after ECAE following routes B_C and C as listed in Table 7.2. Zn contents in the eutectoid phase increased from about 37 wt.% in the as-cast state to 50 wt% after the first ECAE pass and continued to increase up to an average of 58 wt.% after 8 ECAE passes for both routes. This increase in Zn content of the eutectoid phase was accompanied by an increase of the Al content in the eutectic matrix; however, the latter is less significant as can be seen in Table 7.2. This chemical homogenization in the eutectoid phase which took place during ECAE is believed to be a result of the long range diffusion taking place due to the high homologous temperature (0.52 to 0.55 T_m) of processing.

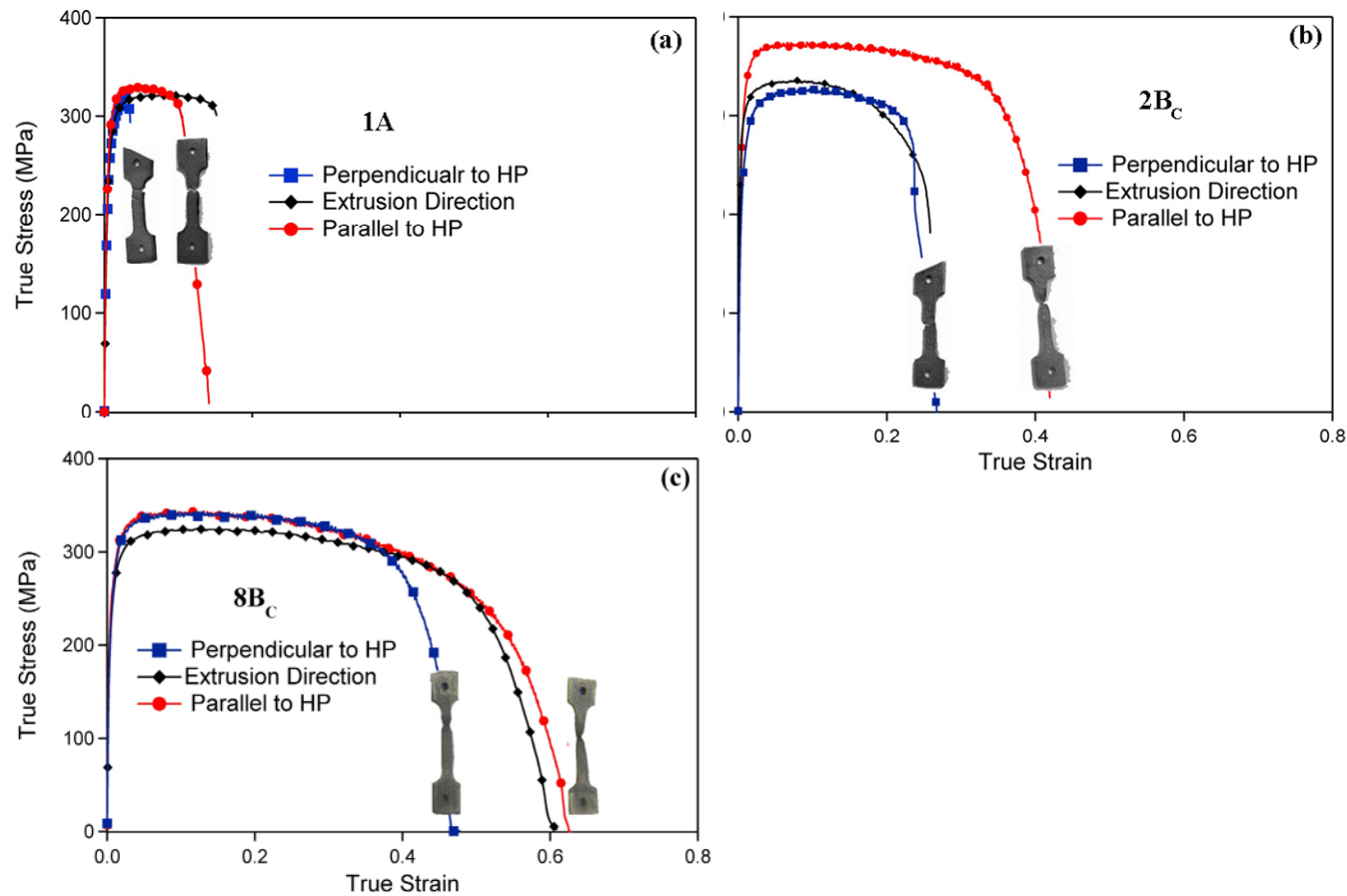


Figure 7.6 Room temperature true stress vs. true strain curves of the ECAE processed ZA-8 alloy tested along the extrusion direction and the directions parallel and perpendicular to the long axis of the elongated hard phase particles or bands (see Figure 1) for samples processed for (a) 1A, (b) 2B_C, and (c) 8B_C. (HP: The long axis direction of the hard-phase particles).

Table 7.2 Chemical compositions of the two phases in the as-cast and ECAE-processed ZA-8 alloy as a function of the processing parameters.

Condition	Eutectic-Matrix		Eutectoid ($\alpha + \eta$)-phase	
	Zn (wt.%)	Al (wt.%)	Zn (wt.%)	Al (wt%)
As-Cast	97.9 ± 0.1	2.11 ± 0.1	37.4 ± 2.0	62.7 ± 2.0
1A	96.5 ± 0.2	3.5 ± 0.2	49.5 ± 1.1	50.5 ± 1.1
2B _C	95.7 ± 0.1	4.3 ± 0.1	51.7 ± 1.1	48.3 ± 1.1
8B _C	95.6 ± 0.2	4.4 ± 0.2	57.8 ± 0.7	42.2 ± 0.7
8C	96.2 ± 0.7	3.8 ± 0.7	58.2 ± 0.8	41.8 ± 0.8

7.4 Microhardness Evolution

The Vickers microhardness levels of the two phases (eutectic and eutectoid) was measured before and after ECAE and the values are listed in Table 7.3. In addition to the overall change in tensile properties reported in Section 7.2, the mechanical properties of the individual constituents also changed as a result of the microstructural refinement depicted in Figures 7.1 and 7.2 and due to chemical homogenization. Relatively high values of the microhardness for both constituents were reached after the first pass and then, they continued to increase until an average increase of about 18% and 26% was achieved for the eutectoid phase and the eutectic matrix, respectively, after eight passes in the presence of chemical homogenization, pointing out significant microstructural refinement.

Table 7.3 Vickers microhardness values of the two phases of the as-cast and ECAE processed ZA-8 alloy as a function of the processing parameters.

Condition	Eutectic-Matrix (HV)	Eutectoid ($\alpha + \eta$)-phase (HV)
As-Cast	77.6 ± 2.0	85.6 ± 3.7
1A	88.9 ± 3.9	97.5 ± 3.1
2B _C	91.9 ± 2.7	100.8 ± 0.7
8B _C	98.4 ± 10.6	102.3 ± 6.4
8C	96.5 ± 5.7	100.4 ± 2.1

7.5 Discussion of the Results

7.5.1 Effects of Al content on mechanical behavior of Zn-Al alloys after ECAE

In the present study, we report a dramatic increase in strength and elongation to failure of the as-cast ZA-8 alloy after ECAE processing. A 50% relative increase in ultimate tensile strength obtained in the present study has not been reported for any ECAE processed Zn-Al alloys to date as can be seen in Figure 7.7. Figure 7.7 shows the evolution of ultimate tensile strength with the number of ECAE passes for ZA-8 processed at 80 °C, ZA-12 processed at 75 °C, ZA-27 processed at 90 °C and ZA-40 processed at 130 °C, all processed following route B_C. In all cases a strength drop was observed after the second pass, and in the case of ZA27 [16] and ZA40 [15], the final strength achieved after four passes was lower than the strength of the as-cast state. In the present study such softening was also observed after the second pass, however, the

decrease in strength as compared to the strength increase after the first pass was quite small. Moreover, higher strength levels are then achieved after eight passes for all routes except route C, in the present case which was not reported in any of the previous works.

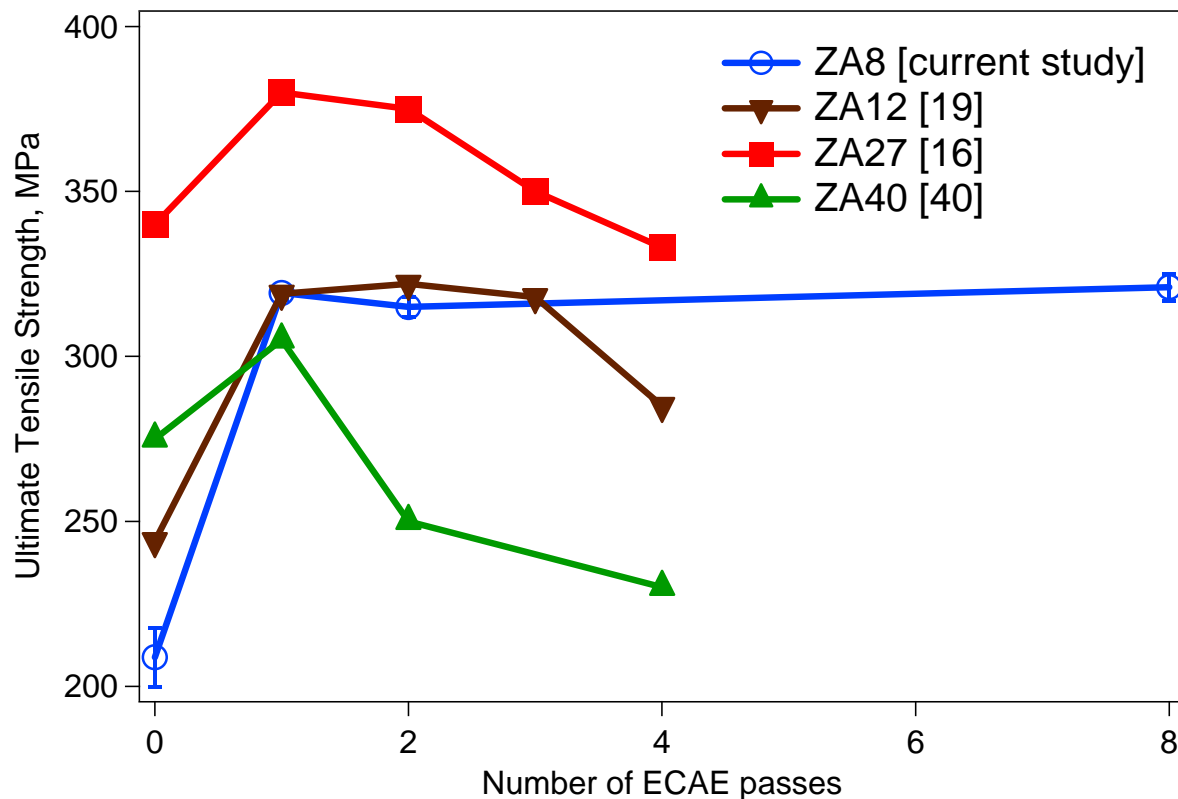


Figure 7.7 Evolution of ultimate tensile strength with the number of extrusion passes in different ECAE studies on Zn-Al alloys including the present work.

Close examination of Figure 7.7 reveals that the amount of increase in strength after the first ECAE pass and then the amount of softening after subsequent ECAE passes of Zn-Al alloys are consistent with the Al content of these alloys. The lower the Al content is, the higher the increase in strength after the first pass and the lower the

amount of softening after the subsequent ECAE passes are. Comparing ZA-8 and ZA-12, just above the eutectoid isotherm, ZA-8 has 17% primary β (ZnAl) phase compared to 50% in case of ZA-12. Upon cooling, the primary β decomposes into eutectoid fine $\alpha + \eta$ lamellae. Therefore, the volume fraction of the eutectoid phase (decomposed β) in ZA-12 is higher than that in ZA-8. Consequently, the spacing between the eutectoid dendrites is smaller in ZA-12. Larger spacing between dendrites will allow them to be sheared into smaller particles and scattered in the eutectic matrix more freely leading to more uniform microstructure. On the other hand, smaller spacing between dendrites will constrain them and allow limited shearing and distribution of the particles in the matrix. It is well known in composite materials that smaller hard phase particles in the matrix will contribute to the strength of the composite more than larger particles. This might explain the higher relative strength increase in ZA-8 than in ZA-12. In addition to the effects of size and distribution of the hard phase in the matrix, deformation-induced chemical homogenization of eutectic and eutectoid phases tends to soften Zn-Al alloys [15]. For the alloys with higher volume fraction of hard particles, like ZA-27 and ZA-40, a saturation level for the distribution of these particles can be reached earlier in terms of the amount of plastic strain applied. Softening then can start taking place because of the deformation-induced chemical homogenization mechanism [15]. In ZA-8, where there is enough space for the particles to be shared and scattered in the matrix, the effects of size and distribution of the hard particles overcome the softening caused by homogenization.

7.5.2 Effects of ECAE processing routes on the microstructural evolution

It is obvious from the optical micrographs of the samples processed up to eight passes following different routes (Figure 7.2) that the shape and distribution of the elongated bands of the eutectoid particles is different for the four presented cases. These bands are finer and distributed more uniformly in samples processed via route B_A, B_C and E than those processed via route C. The eutectoid particles are, also, smaller after processing through these former routes. The differences in microstructures, in terms of the shape and distribution of the eutectoid particles in the matrix, are due to the different shearing patterns and slip systems activated during processing. For the sample processed via route C, although the microhardness of the two phases increased and has values close to those of materials processed via route B_C, its structure consists of larger eutectoid particles which are not distributed uniformly as those in the other three routes. This observation can be attributed to the effects of the 90° rotation about the billet axis in route B_C, B_A, and E but not in route C on the shearing patterns and hence the effectiveness of grain refinement. Route C was also found to be the least effective route in introducing high-angle grain boundaries (HAGB) population because of the lack of 90° rotation [115-117]. This is another indication pointing out the influence of the size and distribution of the hard phase on the strength properties of ZA-8 alloy.

7.5.3 Ductility Improvements after ECAE

The remarkable improvement in ductility is mostly due to the refinement of the brittle dendritic structure and reduction of casting porosity after ECAE. Moreover, the distribution and size of the hard eutectoid phase also has a great influence on ductility. The eutectoid phase particle size was reduced by the severe plastic deformation and dispersed uniformly in the matrix. Carcia-Infanta et al. [118] have reported that the elongation to failure increased in Al-Si alloy after ECAE processing because the hard and brittle phase particles became smaller after ECAE processing. Hence, they have less probability of crack nucleation than the large particles found in the as-cast alloy. They also found that the difference in the tensile ductility of the alloys processed using different routes is because of the difference in crack propagation path. The more the hard phase particles become elongated and oriented along the testing direction the harder the propagation path of the crack is. Basically these particles act as barriers to mode-I crack propagation. Figure 7.2 shows how the hard eutectoid particles are elongated and oriented toward the extrusion direction along which the most tensile testing was performed. In the samples processed via routes B_C and E, these particles are more elongated and oriented along the extrusion direction than those in the samples processed via route C and B_A. Therefore, the former routes result in higher tensile elongation to failure values than the routes C and B_A along the extrusion direction. The higher elongation to failure levels observed in the 2B_C and 8B_C samples tested parallel to the long axis of the hard phase particles in Figure 7.6, as compared to the samples tested

along the extrusion direction, support the aforementioned assessment on the positive effects of elongated hard phase particles or bands on ductility.

7.5.4 Flow anisotropy in ECAE processed materials

It is well-known that fiber-reinforced composite systems are stronger in direction parallel to the fiber axis. The 2B_C samples behave similar to the fiber-reinforced composites. They demonstrate higher strength and elongation to failure values when tested parallel to the long axis of the hard eutectoid phase particles, as can be seen in Figure 7.6. The anisotropy in flow strength and elongation to failure tends to decrease with the number of ECAE passes as can be concluded from the tensile responses of the 8B_C samples in Figure 7.6. High magnification back-scattered electron (BSE) images shown in Figure 7.8 reveal the continuous refinement and fragmentation of the hard Al-rich phase during ECAE. This phase in 8B_C samples no longer exists as elongated particles as in the 2B_C samples. Instead, it exists as very fine discontinuous particles forming elongated bands. This might explain the reduction of anisotropy of the mechanical properties in these samples. The effect of the hard phase morphology is even more prevalent in the failure mechanisms of the tensile specimens perpendicular to the long axis of the hard phase particles or bands. The crack propagation path along the hard phase particle boundaries is obvious in the failed tension specimens of the 1A and 2B_C samples. However, the 8B_C specimens exhibited highly ductile fracture in which it necked down to almost a point at high plastic deformation levels similar to the specimens tested along the extrusion direction and parallel to long axis of the elongated hard phase bands.

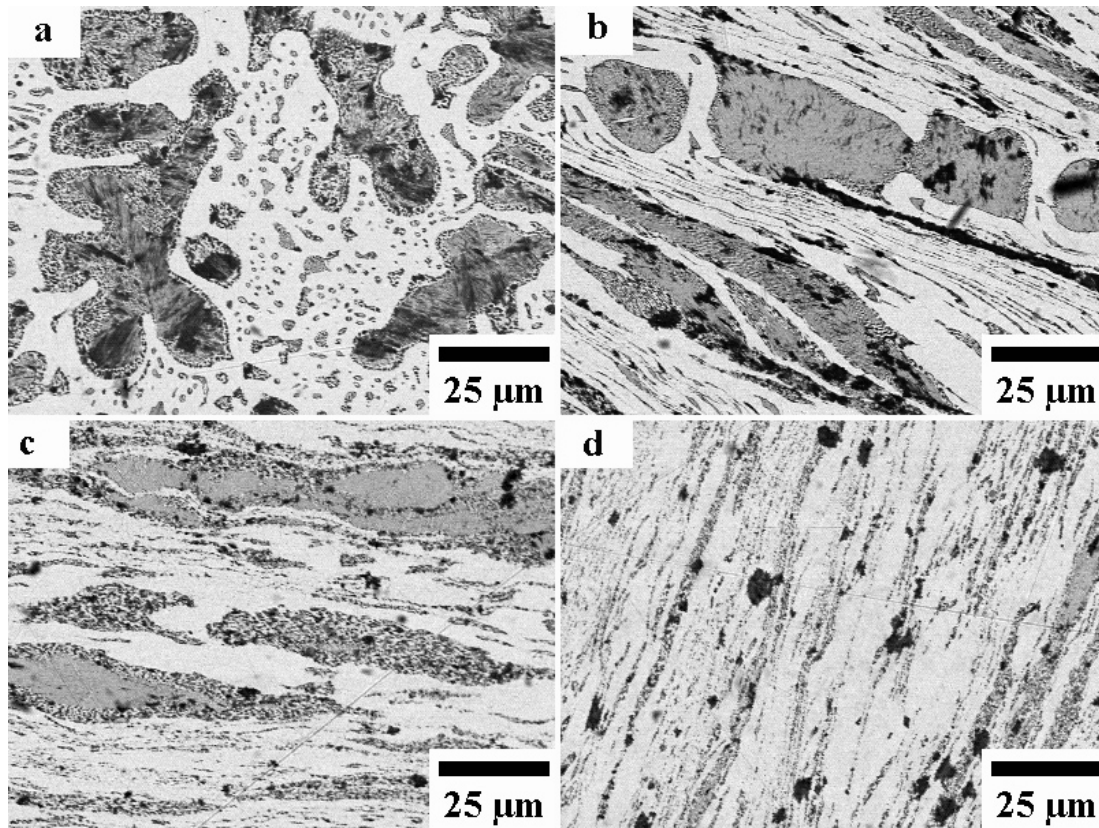


Figure 7.8 Back-scattered electron images of (a) as cast, (b) 1A, (c) 2B_C and (d) 8B_C samples. The hard phase particles are sheared and elongated starting from the first pass. However, the elongated structure is fully developed after the second pass. Large elongated particles can still be seen in 2B_C sample. In 8B_C sample, these particles are broken into much smaller particles that form elongated bands.

7.6 Summary of Observations

The two-phase Zinc - 8 wt.% Aluminum alloy was successfully processed using equal channel angular extrusion (ECAE) following different ECAE routes up to eight passes at temperatures 80 to 100 °C in order to investigate the flow anisotropy of hexagonal closed packed (hcp) materials with the presence of a face-centered cubic (fcc) secondary phase. The main findings of this study can be summarized as follows:

1. ECAE was found to be an effective technique to eliminate the dendritic structure and casting porosity as well as to refine the microstructures in two-phase alloys.
2. ECAE improved the mechanical properties of as-cast ZA-8 alloy. The ultimate tensile strength was significantly increased after the first ECAE pass and saturated almost at the same level with further processing. The substantial improvements in the tensile strength and ductility of the as-cast ZA-8 alloy after multi-pass ECAE were attributed to the elimination of the dendritic microstructure along with casting defects, decrease in the size of hard eutectoid-phase, and relatively homogeneous distribution of these phase particles in the eutectic matrix.
3. The relatively large increase in strength of ZA-8 as compared to what have been reported for other ECAE processed Zn-Al alloys was attributed to the initial lower volume fraction of the eutectoid-phase in ZA-8 and, thus, to the larger dendrite spacing for eutectoid particles to be sheared more effectively and to scatter in the eutectic matrix more uniformly.

4. No notable softening in strength with increasing number of ECAE passes as opposed to other Zn-Al alloys with higher Al content was observed in ZA-8. This is considered to be due to the effects of refined size and more uniform distribution of the hard eutectoid particles in the eutectic matrix overcoming the effects of deformation-induced chemical homogenization which is believed to be the main reason behind softening observed in other ECAE processed Zn-Al alloys.
5. The anisotropy in flow strength and elongation to failure of the ECAE processed samples increases with increasing elongation of the hard second phase particles. Then it drops with further ECAE passes following route B_C, for example, due to the continuous refinement and fragmentation of these particles.

CHAPTER VIII

MAIN CONCLUSIONS

The influence of the crystallographic texture, grain size and the presence of second phase on the flow stress anisotropy and compression asymmetry of hexagonal closed packed alloys was investigated in this dissertation. Equal channel angular extrusion (ECAE) process was very beneficial in introducing a wide variety of texture and grain sizes on AZ31B Mg alloys by varying the processing routes and number of passes. In addition to the conventional ECAE routes, thermo-mechanical processing utilizing ECAE of this alloy was successfully conducted in order to further refine grain sizes. ECAE was also used, successfully, to process Zn-8wt.% Al alloy following different processing routes. The size and distribution of the eutectoid particles varied depending on the number of ECAE passes and routes followed. This helped examining the effects of these particles in the mechanical properties as well as the flow anisotropy of this alloy. Notably the texture and grain shape evolution during ECAE following four conventional and hybrid ECAE routes were successfully predicted using an ECAE simulation model based on a visco-plastic self-consistent (VPSC) polycrystal plasticity scheme. The same material parameters were utilized in all simulations which are conducted continuously without interruption, accounting for the rigid rotations between passes associated with each route. Therefore, reliable predictions of the slip activities during each test could be achieved. The same model coupled with a dislocation-based hardening scheme was also used to predict the tensile and compressive stress-strain

response of as-received hot rolled AZ31B plate and ECAE processed samples along different directions. The main findings of this dissertation can be summarized as follows:

1. The initial grain orientation (initial texture) with respect to the ECAE die orientation significantly affects the evolution of texture, dynamic recrystallization, and grain morphology of the processed AZ31B Mg samples due to different amounts of non-basal slip activity.
2. The activity of prismatic slip system tends to reduce the amount of dynamic recrystallization during ECAE of AZ31B Mg alloy. Prismatic slip acts as a relaxation mechanism that lowers the amount of internal stresses and hence the available energy for DRX.
3. The flow stress anisotropy and tension-compression asymmetry of AZ31B Mg alloy depend on the orientation of the basal poles with respect to the testing directions. The more random distribution of the basal poles is the lower the flow anisotropy and tension-compression asymmetry are.
4. The activity of twins is the main reason behind the flow stress anisotropy and tension-compression asymmetry in AZ31B Mg alloy. More strong texture leads to the activity of twinning system along certain directions and under certain type of loading (compression or tension).
5. Despite the wide variety of ECAE deformation textures produced in AZ31B Mg samples, these textures can be classified in three categories that are called Texture A, Texture C and Texture B_C in this dissertation. When looking on

the flow plane texture, Texture A has two basal peaks close from each other and oriented along the longitudinal direction (LD) of the billet. Texture C has two separate basal peaks separated by 60 - 65° and make an angle of about 45° from the extrusion direction (ED) and longitudinal direction (LD). Texture B_C, however, have one basal peak where basal poles of most grains are oriented along a pole making an angle of about 27-38° from LD.

6. The visco-plastic self-consistent (VPSC) crystal plasticity model, notably, works very well in predicting texture evolution of AZ31B Mg alloy during ECAE following conventional and hybrid routes.
7. ECAE is an effective technique to eliminate the dendritic structure and casting porosity as well as refining the microstructure in as cast two-phase alloys.
8. The substantial improvements in the tensile strength and ductility of the as-cast Zn-8wt.% Al alloy after multi-pass ECAE are attributed to the elimination of the dendritic microstructure, the casting defects, decrease in the size of the hard eutectoid-phase, and relatively homogeneous distribution of these phase particles in the eutectic matrix.
9. The relatively large increase in strength of Zn-8wt.% Al alloy as compared to what have been reported for other ECAE processed Zn-Al alloys is attributed to the initial lower volume fraction of the eutectoid-phase in Zn-8wt.% Al and, thus, to the larger dendrite spacing for eutectoid particles to be sheared more effectively and to scatter in the eutectic matrix more uniformly. The

effects of refined size and more uniform distribution of the hard eutectoid particles in the eutectic matrix overcome the effects of deformation-induced chemical homogenization which is believed to be the main reason behind softening observed in other ECAE Zn-Al alloys.

10. The flow stress anisotropy of Zn-8wt.% Al alloy is dependent on the size and morphology of the hard eutectoid particles. The more refined these particles the lower is the anisotropy despite the elongated bands they form which are usually oriented along the same direction.

CHAPTER IX

SUGGESTIONS FOR FUTURE WORKS

1. The current study of flow stress anisotropy and tension-compression asymmetry of AZ31B Mg alloys was carried out by measuring and predicting the mechanical response of the ECAE processed samples along the three orthogonal directions of the billets: ED, LD and FD. From the crystallographic textures of the ECAE processed samples, this study can be extended to account for other important directions. For example, the direction of basal poles in the samples having Texture B_C samples.
2. Because of the size of AZ31B samples processed using the hybrid routes, the tension tests of these samples were limited along the extrusion direction (ED). It was observed that these hybrid routes produced samples of higher strength along the flow direction (FD). Only compression tests were performed along this direction because of the small size of the processed sample. Since, plastic deformation is mainly accommodated by twinning during compression along this direction, tension tests along this direction are necessary to confirm the finding that grain size has limited influence on slip systems activity. To overcome the size limitations, the AZ31B Mg alloy can be processed as bulk billets following hybrid route. It can also be processed inside larger cans.

3. Texture prediction during ECAE of AZ31B Mg alloy was carried out using the visco-plastic self-consistent (VPSC) polycrystalline model without considering hardening of deformation modes. This was sufficient to successfully predict the texture even after seven ECAE passes at relatively high temperatures. However, modeling post-ECAE processing at room temperature requires the knowledge of critical stress evolution during ECAE. Therefore, hardening evolution during ECAE should be accounted for by using a hardening scheme like the dislocation-based one.
4. The dislocation-based hardening scheme has many parameters associated for each slip systems. Fitting the experimental stress-strain curves to find out all these parameters is a time consuming process. Reducing these parameters by combining some of them will facilitate the application of this hardening model.
5. Tension and compression tests at several temperatures in addition to the room temperature tests should be done in order to improve the hardening parameters.
6. Post-ECAE processing can be used to further increase the strength of Mg alloys. Low temperature rolling is a good candidate to further refine the grains and increase the internal stresses of the alloy. Compressing the ECAE processed billets that have Texture A type along their extrusion axis can introduce twinning in the billet which increases the volume fraction of

boundaries that hinder the dislocation movement. This is expected to have significant increase on yield strength of the alloy.

7. Post-ECAE processing like rolling can increase the texture strength and hence increase the flow stress anisotropy. High flow stress anisotropy is beneficial in some applications such as blast protection applications.
8. Plate ECAE helps producing plates with ultrafine grained microstructures while preserving the strong basal texture of hot-rolled plate. Type A texture observed after ECAE is an evidence of the possibility of fabricating such plates. The current VPSC model used in this dissertation will help in designing the processing routes to obtain plates with desired textures and grain sizes.
9. ECAE found to be an efficient processing technique to eliminate the dendritic structure and casting porosities of as-cast two-phase Zn-Al alloys and hence improve the mechanical properties of these alloys. Other two-phase alloys should be processed using ECAE in order to improve their mechanical properties.

REFERENCES

- [1] Yoo MH. Metallurgical Transactions A 1981;12A:409.
- [2] Agnew SR, Yoo MH, Tomé CN. Acta Materialia 2001;49:4277.
- [3] Phillipe MJ, Wagner F, Mellab FE, Esling C, Wegria J. Acta Metallurgica et Materialia 1994;42:239.
- [4] Yapici GG, Karaman I. Materials Science and Engineering A 2004;503:78.
- [5] Yapici GC, Karaman I, Maier HJ. Materials Science and Engineering A 2006;434:294.
- [6] Yapici GC, Tomé CN, Beyerlein IJ, Karaman I, Vogel SC, Liu C. Acta Materialia 2009;57:4855.
- [7] Yapici GC, Karaman I, Luo ZP, Rack H. Scripta Materialia 2003;49:1021.
- [8] Karaman I, Yapici GC, Chumlyakov YI, Kireeva IV. Materials Science and Engineering A 2005;410-411:243.
- [9] Haouaoui M, Karaman I, Maier HJ. Acta Materialia 2006;54:5477.
- [10] Yapici GC, Beyerlein IJ, Karaman I, Tomé CN. Acta Materialia 2007;55:4603.
- [11] Al-Samman T, Gottstein G. Materials Science and Engineering A 2008;488:406.
- [12] Barnett MR. Materials Science and Engineering A 2007;464:1.
- [13] Jain A, Agnew SR. Materials Science and Engineering A 2007;462:29.
- [14] Agnew SR, Horton JA, Lillo TM, Brown DW. Scripta Materialia 2004;50:377.
- [15] Purcek G, Saray O, Karaman I. Materials Science and Engineering A 2008;490:403.

- [16] Purcek G, Altan BS, Miskioglu I, Patil A. *Materials Science and Technology* 2005;21:1044.
- [17] Furukawa M, Ma Y, Horita Z, Nemoto M, Valiev RZ, Langdon T. *Materials Science and Engineering A* 1998;241:122.
- [18] Kumar P, Xu C, Langdon T. *Materials Science and Engineering A* 2006;429:324.
- [19] Purcek G. *Journal of Materials Processing Technology* 2005;169:242.
- [20] Purcek G, Karaman I, Yapici GG, Al-Maharbi M, Kucukomeroglu T, Saray O. *International Journal of Materials Research* 2007;98:332.
- [21] Purcek G, Altan BS, Miskioglu I, Ooi PH. *Journal of Materials Processing Technology* 2004;148:279.
- [22] Segal VM, Reznikov V, Drobyshevskiy A, Kopylov V. *Russian Metallurgy* 1981;1:99.
- [23] Furukawa M, Horita Z, Langdon TG. *Materials Science and Engineering A* 2002;332:97.
- [24] Beyerlein I, Tóth L. *Progress in Materials Science* 2009;54:427.
- [25] Beyerlein IJ, Lebensohn RA, Tome' CN. *Materials Science and Engineering A* 2002;345:122.
- [26] Beyerlein IJ, Capolungo L, Yapici GG, Tomé CN, Karaman I. In: Zhao Y, Liao X, editors. *Ductility of Bulk Nanostructured Materials*, 2009a.
- [27] Lebensohn RA, Tome' CN. *Acta Metallurgica et Materialia* 1993;41:2611.
- [28] Segal VM. *Materials Science and Engineering A* 1999;271:322.

- [29] Iwahashi Y, Wang J, Horita Z, Nemoto M, Langdon TG. *Scripta Materialia* 1996;35:143.
- [30] Utyashev F, Enikeev F, Latysh V. *Annales De Chimie-Science Des Materiaux* 1996;21:379.
- [31] Berbon P, Furukawa M, Horita Z, Nemoto M, Langdon TG. *Metallurgical and Materials Transactions A-Physical Metallurgy and Materials Science* 1999;30:1989.
- [32] Nakashima K, Horita Z, Nemoto M, Langdon TG. *Materials Science and Engineering A* 2000;281:82.
- [33] Horita Z, Furukawa M, Nemoto M, Langdon TG. *Materials Science and Technology* 2000;16:1239.
- [34] Agnew SR, Duygulu O. *International Journal of Plasticity* 2005;21:1161.
- [35] Agnew SR, Tomé CN, Brown DW, Holden TM, Vogel SC. *Scripta Materialia* 2003;48:1003.
- [36] Klimanek P, Pöttsch A. *Materials Science and Engineering A* 2002;324:145.
- [37] von Mises R. *Zeitschrift für Angewandte Mathematik und Mechanik* 1928;8:161.
- [38] Taylor G. *Journal of the Institute of Metals* 1938;62:307.
- [39] Graff S, Brocks W, Steglich D. *International Journal of Plasticity* 2007;23:1957.
- [40] Stohr J, Poirier J. *Philosophical Magazine* 1972;25:1313.
- [41] Obara T, Yoshinga H, Morozumi S. *Acta Metallurgica* 1973;21:845.
- [42] Ando S, Tonda H. *Materials Transactions JIM* 2000;41:1188.
- [43] Hutchinson JW. *Metallurgical Transactions A* 1977;8:1465.

- [44] Hirth JP, Lothe J. Theory of dislocations. Malabar, Florida: Krieger Publishing Company; 1992.
- [45] Kronberg ML. Acta Metallurgica 1961;9:970.
- [46] Yoo MH. Transactions of the Metallurgical Society of AIME 1969;245:2051.
- [47] Koks U, Westlake D. Transactions of the Metallurgical Society of AIME 1967;239:1107.
- [48] Hauser F, PR L, Dorn J. Transactions of the American Institute of Mining and Metallurgical Engineers 1956;206:589.
- [49] Koike J, Kobayashi T, Mukai T, Watanabe H, Suzuki M, Maruyama K, Higashi K. Acta Materialia 2003;51:2055.
- [50] Capolungo L, Beyerlein IJ, Tomé CN. Scripta Materialia 2009;60:32.
- [51] Christian J, Mahajan S. Progress in Materials Science 1995;39:1.
- [52] Chino Y, Kimura K, Mabuchi M. Materials Science and Engineering A 2008;486:481.
- [53] Brown DW, Agnew SR, Bourke MAM, Holden TM, Vogel SC, Tomé CN. Materials Science and Engineering A 2005;399:1.
- [54] Wang YN, Huang JC. Acta Materialia 2007;55:897.
- [55] Mukai T, Yamanoi M, Watanabe H, Higashi K. Scripta Materialia 2001;45:89.
- [56] Yamashita A, Horita Z, Langdon T. Materials Science and Engineering A 2001;300:142.
- [57] Gan WM, Zheng MY, Chang H, Wang XJ, Qiao XG, Wu K, Schwebke B, Brokmeier H-G. Journal of Alloys and Compounds 2009;470:256.

- [58] Suwas S, Gottstein G, Kumar R. *Materials Science and Engineering A* 2007;471:1.
- [59] Agnew SR, Mehrotra P, Lillo TM, Stoica GM, Liaw PK. *Acta Materialia* 2005;53:3135.
- [60] Xia K, Wang JT, Wu X, Chen G, Gurvan M. *Materials Science and Engineering A* 2005;410-411:324.
- [61] Eddahbi M, del Valle JA, Perez-Prado MT, Ruano OA. *Materials Science and Engineering A* 2005;410-411:308.
- [62] Kim WJ, Hong SI, Kim YS, Min SH, Jeong HT, Lee JD. *Acta Materialia* 2003;51:3293.
- [63] Liu T, Wang YD, Lin Peng R, Huang CX, Jiang CB, Li SX. *Scripta Materialia* 2004;51:1057.
- [64] Smith AE. *Surface Science* 2007;601:5762.
- [65] Chetty N, Weinert M. *Physical Review B* 1997;56:10844.
- [66] Ion SE, Humphreys FJ, White SH. *Acta Metallurgica* 1982;30:1909.
- [67] Ding SX, Lee WT, Chang CP, Chang LW, Kao PW. *Scripta Materialia* 2008;59:1006.
- [68] Foley D, Al-Maharbi M, Hartwig TK, Karaman I, Kecskes L, Mathaudhu S. unpublished work.
- [69] Barnett MR, Ghaderi A, Sabirov I, Hutchinson B. *Scripta Materialia* 2009;61:277.

- [70] Koike J, Ohyama R, Kobayashi T, Suzuki M, Maruyama K. *Materials Transactions* 2003;44:445.
- [71] Jin L, Dongliang L, Mao D, Zeng X, Ding W. *Materials Letters* 2005;59:2267.
- [72] Chino Y, Kimura K, Hakamada M, Mabuchi M. *Materials Science and Engineering A* 2008;485:311.
- [73] Murphy S, Savaskan T. *Wear* 1984;98:151.
- [74] Calayag T, Ferres D. *Proceedings of the SAE Annual Conference*, vol. paper No. 820643, 1983. p.2241.
- [75] Savaskan T, Purcek G, Murphy S. *Wear* 2002;252:693.
- [76] Marczak RJ, Ciach R. *1st European Tribological Congress*. London: Institution of Mechanical Engineers, 1973. p.223
- [77] Delneville P. *Wear* 1985;105:283.
- [78] Tanaka T, Chung SW, Chaing L, Makii K, Kushibe A, Kohzu M, Higashi K. *Materials Science and Engineering A* 2005;410-411:104.
- [79] Cay F, Kurnaz C. *Materials and Design* 2005;26:479.
- [80] Abou El-khair MT, Daoud A, Ismail A. *Materials Letters* 2004;58:1754.
- [81] Prasad BK. *Materials Characterization* 2000;44:301.
- [82] El-Baradie ZM, Waly M, Abd El-Azim NN. *Journal of Materials Processing Technology* 2001;114:194.
- [83] Prasad BK. *Materials Science and Technology* 2003;19:327.
- [84] Lo SH, Dionne S, Sahoo M, Hawthorne HM. *Journal of Materials Science* 1992;21:5681.

- [85] Kocks UF, Tome' CN, Wenk H-R. *Texture and Anisotropy*. Cambridge, UK: Cambridge University Press; 1998.
- [86] Hill R. *Journal of the Mechanics and Physics of Solids* 1965;13:89.
- [87] Honneff H, Mecking H. In: Nagashima S, editor. *Proceeding of Sixth International Conference on Texture of Materials (ICOTOM-6)*. Tokyo: Iron and Steel Institute of Japan, 1981. p.347.
- [88] Tome' CN, Lebensohn RA, Necker CT. *Metallurgical and Materials Transactions A-Physical Metallurgy and Materials Sciece* 2002;33:2635.
- [89] Tome' CN, Maudlin PJ, Lebensohn RA, Kaschner GC. *Acta Materialia* 2001;49:3085.
- [90] Proust G, Tome' CN, Kaschner GC. *Acta Materialia* 2007;55:2137.
- [91] Beyerlein IJ, Tome' CN. *International Journal of Plasticity* 2008;24:867.
- [92] Tóth L, Massion RA, Germain L, Baik SC, Suwas S. *Acta Materialia* 2004;52:1885.
- [93] Beyerlein IJ, Tome' CN. *Materials Science and Engineering A* 2004;380:171.
- [94] Beyerlein IJ, Tomé CN. *International Journal of Plasticity* 2008;24:867.
- [95] Essmann U, Mughrabi H. *Philosophical Magazine A* 1979;40:731.
- [96] Mecking H, Kocks UF. *Acta Metallurgica* 1981 29:1865.
- [97] Madec R, Devincre B, Kubin LP. *Physical Review Letters* 2002;89:255508.
- [98] Maier HJ, Gabor P, Gubta N, Karaman I, Haouaoui M. *International Journal of Fatigue* 2006;28:243.
- [99] Barber RE, Dudo T, Yasskin P, Hartwig KJ. *Scripta Materialia* 2004;51:373.

- [100] Beyerlein IJ, Toth LS. *Progress in Materials Science* 2008;54:427.
- [101] Beyerlein IJ, Field RD, Hartwig KT, Necker CT. *Journal of Materials Science* 2008;43:7465.
- [102] Figueiredo RB, Beyerlein IJ, Zhilyaev AP, Langdon TG. *Materials Science and Engineering A* 2009;submitted.
- [103] Yapici GG, Tomé CN, Beyerlein IJ, Karaman I, Vogel, SC, Liu C. *Acta Materialia* 2009;57:4855.
- [104] Beausir B, Suwas S, Toth L, Neale K, Fundenberger J. *Acta Materialia* 2008;56:200.
- [105] Kelley E, Hosford W. *Transactions of the Metallurgical Society of AIME* 1968;242:5.
- [106] Reed-Hill: RE. *American Society of Metals* 1973;Metals Park:285.
- [107] HIRSCH P, LALLY J. *Philosophical Magazine* 1965;12:595.
- [108] Barnett MR, Keshavarz Z, Ma X. *Metallurgical and Materials Transactions A-Physical Metallurgy and Materials Science* 2006;37A:2283.
- [109] Barnett MR. *Journal of Light Metals* 2001;1:167.
- [110] Drucker DC. *Metallurgical Transactions* 1973;4:667.
- [111] Al-Samman T, Gottstein G. *Materials Science and Engineering A* 2008;490:411.
- [112] Proust G, Tomé CN, Jain A, Agnew SR. *International Journal of Plasticity* 2008;25:861.
- [113] Sun P, Kao P, Chang C. *Metallurgical and Materials Transactions A-Physical Metallurgy and Materials Science* 2004;35A:1359.

- [114] Cáceres CH, Lukáč P, Blake A. *Philosophical Magazine* 2008;88:991.
- [115] Iwahashi Y, Horita Z, Nemoto M, Langdon TG. *Acta Materialia* 1998;46:3317.
- [116] Gholinia A, Prangnell M, Markushev MV. *Acta Materialia* 2000;48:1115.
- [117] Sun P, Kao P, Chang C. *Metallurgical and Materials Transactions A-Physical Metallurgy and Materials Science* 2004;35A:1359.
- [118] Garacia-Infanta JM, Zhilyaev AP, Cepeda-Jimenez CM, Ruano OA, Ruano OA, Carreno F. *Scripta Materialia* 2008;58:138.

VITA

Name: Majid Al Maharbi

Address: Department of Mechanical and Industrial Engineering
Sultan Qaboos University
P.O. Box 33, Al-Khod 123
Sultanate of Oman

Email Address: majidm@squ.edu.om

Education: B.E., Mechanical Engineering, Sultan Qaboos University,
Sultanate of Oman, 2000
M.S., Materials Science, Arizona State University, Tempe, 2003